Remote sensing, tracking and imaging inside MRI systems

by

Mehmet Berk Bilgin

A Dissertation Submitted to the
Graduate School of Sciences and Engineering
in Partial Fulfillment of the Requirements for
the Degree of

Master of Science

in

Electrical and Electronics Engineering

December 16, 2021

Remote sensing, tracking and imaging inside MRI systems

Koç University

Graduate School of Sciences and Engineering

This is to certify that I have examined this copy of a master's thesis by

Mehmet Berk Bilgin

and have found that it is complete and satisfactory in all respects,
and that any and all revisions required by the final
examining committee have been made.

Committee Members:

_____

Prof. Metin Sitti (Advisor)

_____

Prof. Havva Yağcı Acar (Co-Advisor)

_____

Prof. Hakan Ürey

_____

Prof. Mehmet Burçin Ünlü

_____

Assoc. Prof. Sedat Nizamoğlu

Date: _____

Dedicated to all who believe in science and achievable better

ABSTRACT

Remote sensing, tracking and imaging inside MRI systems
Mehmet Berk Bilgin
Master of Science in Electrical and Electronics Engineering
December 16, 2021

In addition to diagnostic and therapeutic uses, clinical magnetic resonance imaging (MRI) systems have also been used for interventional procedures. However, safety risks associated with increased specific absorption rate and tissue overheating should be measured *in-situ* and controlled during such procedures. Here, we introduce a self-resonating radio frequency (RF) sensor capable of remote temperature sensing to serve as a visual indicator of *in-situ* temperature changes during real-time MRI interventional operations. We propose a new sensor design that uses dielectric properties as the tuning mechanism for the sensor resonant frequency and the temperature dependence of permittivity. Using a 7 Tesla (7T) preclinical MRI, we demonstrate *ex vivo* feasibility and remote temperature sensing capabilities in the clinically relevant temperature range of 36-42°C. The miniature design of the sensor allows its placement on the tip of a catheter, where it can be used for both catheter tracking and temperature sensing. The RF sensor is tuned to match the resonant frequency of 7T MRI (298 MHz), enabling a hyperintense signal on the sensor in the MR images. Hence, it can be used for three-dimensional position tracking during the steering of a given interventional medical device, such as a catheter. As temperature increases, the sensor detunes due to the change in the relative permittivity, and the hyperintense signal disappears in the MR image, serving as a direct visual indicator of the temperature change in real-time without a need for post-processing. Since this technique is based on common MR imaging sequences, the same image can be used for both device localization and temperature measurement. 0.6°C accuracy is achieved in the physiological range between 36°C and 42°C. Such RF sensors could provide safer operations in future MRI interventional procedures with potential local increased temperatures.

MRI is also a heavily utilized medical diagnostic tool that usually employs a contrast agent for enhanced image sensitivity and selectivity. Superparamagnetic iron oxide nanoparticles (SPIONs) have been shown as strong MRI contrast agents in the literature but usually with a dark (T2) contrast. However, bright contrast (T1 contrast agent) is preferred by the radiologists in the clinic, yet difficult to achieve. Here, we show T1 contrast generation of polyacrylic acid-coated superparamagnetic iron oxide nanoparticles (SPION-PAA) in our 7 Tesla MRI. We showed that such T1 contrast is achievable in *ex vivo* mouse experiments, as well.

Interaction of SPION with UV or visible light is also an exciting phenomenon that may be exploited in photopolymerization to produce polymer/SPION nanocomposites for both enhancing MRI imaging contrast and 3D printing small-scale MRI robots. Using biocompatible SPIONs of nanoscale size and high stability eliminates the need for an initiator that might be undesirable in biological applications. We show that SPION-PAA can also be used as an initiator in the photopolymerization of vinyl monomers. Differential scanning calorimeter experiments were conducted to find optimal parameters for the highest and fastest conversion conditions. Furthermore, synthesized SPION/polymer hybrids/gels were demonstrated as efficient sensitizers for hyperthermia in an alternating magnetic field.

ÖZETÇE

MRI sistemlerinde uzaktan algılama, izleme ve görüntüleme

Mehmet Berk Bilgin

Elektrik ve Elektronik Mühendisliği, Yüksek Lisans

16 Aralık 2021

Teşhis ve tedavi amaçlı kullanımlara ek olarak, klinik manyetik rezonans görüntüleme (MRI) sistemleri girişimsel prosedürler için de kullanılır. Fakat, artan spesifik absorpsiyon oranı (SAR) ve doku aşırı ısınması ile ilişkili güvenlik riskleri, sürekli gözlemlenmeli ve bu tür prosedürler sırasında kontrol edilmelidir. Bu tezde, gerçek zamanlı MRI girişimsel operasyonlar sırasında yerinde sıcaklık değişikliklerinin görsel bir göstergesi olarak hizmet etmek üzere uzaktan sıcaklık algılama yeteneğine sahip, bir radyo frekansı (RF) sensörünü sunuyoruz. Elektriksel geçirgenliğin sıcaklık bağımlılığını ayar mekanizması olarak kullanan yeni bir sensör tasarımı öneriyoruz. 7 Tesla (7T) klinik öncesi MRI kullanarak, tıbbı olarak önemli 36-42°C sıcaklık aralığında *ex vivo* fizibilite ve uzaktan sıcaklık algılama yeteneklerini gösteriyoruz. Sensörün minyatür tasarımı hem ucuna yerleştirildiği kateteri izleme hem de sıcaklık algılama için kullanılmasına izin verir. RF sensörü, MR görüntülerinde sensör üzerinde yoğun sinyal sağlayan 7T MRI (298 MHz) rezonans frekansına ayarlı şekilde ayarlanmıştır. Bu nedenle, kateter gibi belirli bir girişimsel tıbbi cihazın yönlendirilmesi sırasında üç boyutlu konum takibi için kullanılabilir. Sıcaklık arttıkça, elektriksel geçirgenlikteki değişiklik nedeniyle sensörün rezonansı kayar, MR görüntüsünde yoğun sinyal kaybolur ve sonradan işlemeye gerek kalmadan gerçek zamanlı olarak sıcaklık değişiminin doğrudan görsel göstergesi olarak işlev görür. Bu teknik yaygın olarak kullanılan MR görüntüleme dizilerine dayandığından, elde edilen görüntü hem cihaz lokalizasyonu hem de sıcaklık ölçümü için kullanılabilir. 0.6°C doğruluk, 36°C ile 42°C arasındaki fizyolojik aralıkta elde edilir. Bu tür RF sensörü, potansiyel yerel doku ısınma durumlarına karşın gelecekteki MRI girişimsel prosedürlerinde daha güvenli operasyonlar sağlayabilir.

MR aynı zamanda sıklıkla kullanılan bir tıbbi tanı aracıdır ve genellikle gelişmiş hassasiyet ve seçicilik için bir kontrast maddesi kullanır. Süperparamanyetik demir oksit nanoparçacıkları (SPION), literatürde güçlü MR kontrast maddesi olarak gösterilmiştir, ancak genellikle koyu (T2) kontrastlıdırlar. Ancak klinikte radyologlar tarafından parlak kontrast (T1 kontrast ajanı) tercih edilir, fakat elde edilmesi zordur. Burada, 7 Tesla MRI'da poliakrilik asit kaplı süperparamanyetik demir oksit nanoparçacıklarının (SPION-PAA) T1 kontrast üretimini gösteriyoruz. T1 kontrastının, *ex vivo* fare deneylerinde de elde edilebildiği gösterilmiştir.

SPION'un UV veya görünür ışık ile etkileşimi, fotopolimerizayon ile hem MR kontrastı hem de MR robotiği alanında kullanılabilecek SPION-polimer nanokompozitleri üretmek için çok ilgi çeken bir yönüdür. Küçük boyutlu ve yüksek kararlılığa sahip SPION kullanılması, biyolojik uygulamalarda istenmeyen bir başlatıcı ihtiyacını ortadan kaldırır. Bu çalışmada, SPION-PAA'nın vinil monomerlerin fotopolimerizayonda başlatıcı olarak da kullanılabileceğini gösterdik. En yüksek ve en hızlı polimerleşme koşullarını sağlayan parametreleri bulmak için DSC deneyleri yapıldı. Ayrıca, sentezlenen SPION/polimer hibritleri/jeller, değişken manyetik alan altında hipertermi için etkili araçlar olarak gösterildi.

ACKNOWLEDGEMENTS

I would like to start with my advisors, Metin Sitti and Havva Funda Yağcı Acar, who guided me through my thesis research. Their supervision and support made this thesis possible. I want to thank Mehmet Efe Tiryaki, Jelena Zinnanti and Mona Nejatpour who supported and helped me in my various projects. I want to express my gratitude to Adnan Kurt, whose advice and opinions I hold very dear. I want to thank Prof. Alphan Sennaroğlu for all the fruitful discussions. I specially thank to my thesis committee members, Sedat Nizamoğlu, Burçin Ünlü and Hakan Ürey.

I want to thank all of the Polymers and Nanomaterials research group members, especially Gözde Demirci and Pelda Akın, for their help in this thesis. I also would like to thank all the Physical Intelligence department members in Max-Planck Institute for Intelligent Systems. I want to express my gratitude to Mustafa Bilgin and Muharrem Güler for their assistance in time of need.

I would like to thank my all my colleagues who was there with me throughout my MS studies: Gökhan Gürbilek, Gözde Demirci, Işınsu Baylam, Abdullah Muti, Yağız Morova, Berna Morova, Gökhan Tanısalı, Cem Dayan, Sinan Demir, Saadet Baltacı, Martin Phelan, Uğur Bozüyük, Birgül Akolpoğlu, Nihal Doğan, Hakan Ceylan, Patricia Martinez and Hasan Abi.

I would like to thank my family for their endless support and patience. Also, I want to commemorate Mustafa Eyriboyun, whom I will always remember for his kindness and endless enthusiasm for teaching. Finally, I want to express my deep respect and sincere gratitude to Jülide Yener and Meral Eryürek, who inspired and motivated me to follow this scientific path early on.

TABLE OF CONTENTS

LIST OF TABLES

LIST OF FIGURES

ABBREVIATIONS

RC	Relative Contrast
RF	Radio-frequency
RMSE	Root Mean Squared Error
nm	nanometer
SPION	Superparamagnetic iron oxide nanoparticles
PAA	Polyacrylic acid
SPION-PAA	Polyacrylic acid coated superparamagnetic iron oxide nanoparticles
DSC	Differential Scanning Calorimeter
PhotoDSC	Photo-Differential Scanning Calorimeter
MRI	Magnetic resonance imaging
NMR	Nuclear magnetic resonance
TEM	Transmission Electron Microscopy
VSM	Vibrating Sample Magnetometer

Chapter 1:
INTRODUCTION

1.1 Magnetic resonance imaging

Magnetic resonance imaging (MRI) is a powerful non-invasive medical imaging technique. High-resolution imaging capabilities and non-ionizing nature make it one of the most commonly used imaging methods in clinics and hospitals. Since its introduction to clinical use in the early 1980s, it has become a staple tool for diagnostic medicine. Especially, in oncological and neurological disfunctions, MRI serves an essential part of diagnosing and tracking of the diseases/disorders progress.

MRI is based on the nuclear magnetic resonance phenomenon (NMR). In quantum theory, protons in the nuclei have a spin, sometimes referred to as the magnetic moment. This magnetic moment is a quantized vector value. At relaxed conditions, the magnetic moment of protons is randomly distributed; hence, the net magnetic moment is zero. However, when a magnetic field of B_0 is applied, these magnetic moments tend to align themselves in the direction of B_0. If an RF pulse is applied to these aligned protons, they react and change orientation proportional to the RF pulse. This excited state is unstable by nature, and while relaxing to the stable state, this extra energy is dispersed. NMR tracks and records this relaxation of the protons.

However, absorption of the RF pulse only happens if the RF wave's frequency matches the proton's precession at the given magnetic field B_0. The frequency of the precession is put forward with Larmor's equation given as, $f_0 = \gamma * B_0$, where γ is the gyromagnetic ratio for that proton and B_0 is the magnitude of the applied magnetic field. This value is specific to particles or atoms. For hydrogen protons in a water molecule, $\gamma = 42.58\ MHz/Tesla$.

MRI adds visualization to the NMR by collecting NMR data in frequency space called k-space. Data coming from the receiver coil is converted into the frequency domain using FFT processing techniques. Using frequency domain signals enables MRI to pinpoint the region where the signal originates and create an image of signal intensities across the field of view.

1.2 MRI as an interventional tool

MRI provides a versatile environment with ultra-strong static magnetic fields and adjustable gradients. Gradient amplitude can be adjusted, and the applied region can be set to the desired location. Furthermore, imaging with MRI can be done on command and take a relatively short time. Since imaging can be done simultaneously with the intervention and without additional gear, MRI offers the much-required visual feedback for closed operations. Hence, MRI-guided intervention alternatives are safer than their open operations counterparts due to their minimally invasive nature, which decreases the chance of healthy tissue damage, induced pain, and hospital stay durations [1].

Researchers realized early on that MRI can be used as an intervention environment [2], [3]. Since then, many different interventional designs utilizing MRI have been proposed. Active catheters [4], [5], MRI-compatible actuators [6], [7], untethered robots [8]–[10] are a few common focus designs of the field.

1.3 Tracking and sensing in MRI

For tracking and labeling inside MRI, various methods were proposed, such as; contrast agents [11]–[13], active tracking device [14], magnetic markers [15]–[17], and RF markers [18]–[20]. Contrast agents are substances that shorten the relaxation times of the surrounding around and, therefore, affect the signal on images. Usually, T1 agents result in positive(bright), and T2 agents create negative(dark) contrasts. Magnetic markers change the magnetic susceptibility around the marker, hence shifting the exerted B_0 field. By changing the Larmor frequency, Magnetic markers result in dark spots in the MR images. Active tracking methods include devices that are connected to the receiver of the MRI and give position information directly. RF markers are resonant devices that use applied RF pulse to increase signal. They create positive contrasts in images.

Sensing with MRI is extensively investigated. MRI has been used for sensing many different stimuli such as temperature [21]–[24], blood flow [25], blood oxygen levels [26], and countless tissue abnormalities and damages [27]–[29]. In all of the methods mentioned above, MRI is used without additional equipment. Hence, available measurements are limited with the imaging capability of the MRI. However, using additional implantable or insertable tools to overcome this bottleneck will help us

further enhance the use and abilities of the MRI. Only one study investigated such a tool in MRI for sensory purposes. Hai et al. used diode circuitry and RF markers to detect neuron activity near the sensor [30].

1.4 Thesis contribution

Tracking and sensing in the MRI environment require further advancement before the clinical phase. MRI-guided robotics promise new and less risky alternatives to complex operations. However, these tools are yet to be proven safe for widespread clinical use. For safe operations inside MRI, tools must be closely watched for potential harm such as heating, tissue damage, etc. New tracking methods will be helpful for MRI-guided tools, where monitoring is one of the critical issues. Completing such void in the field would help achieve faster feedback rates and better control of the interventional device. Safer and more effective methods required for clinical use can be delivered with better tracking and sensing mechanisms.

The development of new contrast agents for MRI continues to be the focus of researchers. Clinicians highly prefer biocompatible contrast agents with long blood circulation and high contrast ability; thus, SPION as a contrast agent attracted considerable attention. Furthermore, there is already extensive research on other functions of SPION such as, hyperthermia [31], [32], actuation [33], photopolymerization and 3D printing [34], gene therapy [35], [36], and drug delivery [37]. Biocompatibility, high magnetic saturation and small size of the particles make SPIONs a great candidate for future biomedical research, as their multifunctionality can simplify any system they are used in.

This thesis has following contributions:

1. Proposed and demonstrated (*ex vivo*) a new RF sensor at a few millimeters length scale for *in-situ* temperature measurements for interventional MRI systems. This work is the first study to demonstrate MRI remote temperature sensor.

2. Demonstrated (*ex vivo*) SPION-PAA as a new biocompatible dual-mode MRI contrast agent. The achieved contrast changes between T1 and T2 depending on the nanoparticle concentration.

3. Demonstrated photopolymerization initiation with SPION-PAA. Created gels have intrinsic high magnetic properties that can be used for actuation and magnetic heating.

Chapter 2:
RF MARKERS AS REMOTE TEMPERATURE SENSORS DURING MRI INTERVENTIONAL PROCEDURES

2.1 Background

Recently, MRI-guided minimally-invasive interventional procedures have attracted extensive attention in medical robotics as a potential alternative to traditional two-dimensional (2D) fluoroscopic imaging methods because of MRI's ionizing-radiation-free nature and tree-dimensional (3D) high-resolution soft tissue imaging capability [6], [20], [38]–[41]. By developing different medical robot or device designs in MRI, such as MRI-compatible guide wires [42], [43], soft pneumatic actuators [44], [45], piezo actuators [7], [46], focused ultrasound (FUS) systems [40], [47], [48], active catheters [49], [50], needle insertion systems [6], [51], [52], and magnetic microrobots [53]–[58], researchers have demonstrated promising interventional procedures, such as laser ablation [59]–[63], local hyperthermia [48], [64], [65], and FUS ablation [47], [63], [66]. The usage of MRI is mainly limited to the position tracking and steering control of such medical robots or devices with fiducial markers based on radiofrequency (RF) markers [18]–[20], [67]–[69], magnetic markers [15]–[17], and contrast agents [11]–[13].

One of the key challenges during many interventional MRI procedures is the risks associated with overheating, which poses a threat to the patients' safety. Numerous reports have been published concerning the heating of metallic components during MR imaging [70], [71], [80]–[86], [72]–[79]; therefore, continuous *in-situ* temperature monitoring is required for safe interventional MRI applications. As an *in-situ* temperature monitoring method, MRI thermometry has been developed [21]–[24]. Researchers used MRI thermometry-based temperature feedback to control FUS hyperthermia operations [64], [65], [87] or to evaluate MRI-guided laser ablation therapies [41], [60], [88] and MRI-guided active catheters [89], [90]. While MRI thermometry methods can provide accurate *in-situ* temperature mapping in 3D, they decrease overall MRI-based visual feedback by adding an extra sequence, hindering

real-time MRI feedback. In a different approach, some researchers proposed RF-based telemetric devices for measuring the *in-situ* temperature remotely [91]–[94]. However, previously proposed methods include sophisticated circuitry and metallic components that may distort MR images [95]–[97]. Therefore, a safe method for *in-situ* temperature monitoring without decreasing the MRI feedback rate is highly desirable inside the interventional MR scanners.

Previously, various RF marker designs have been reported, while their main focus has been on device 3D tracking inside MRI [18], [19], [102], [20], [67]–[69], [98]–[101]. Most of the proposed RF designs were for catheter tracking inside MRI [98]–[103]. Most of the literature was lacking performance metrics in their work and only few studies focusing on the tracking performance were published [19], [67], [68]. Recent studies explored new designs for ensuring functionality independent of the marker orientation [18], [100], [102]. Beyond tracking, a recent study used an RF marker design for remote bio-sensing in neuron transmission by using an additional field-effect transistor to detune RF coil with environmental stimulus [30]. An alternative approach for remote sensing is to leverage changes in the intrinsic parameters of the RF markers, such as inductance and capacitance. Hence, when a marker reacts to a stimulus, its resonant frequency shifts. With such response mechanism, markers can be used as remote sensors and respond to stimuli while retaining their 3D position tracking abilities.

In this work, we propose a 7T MRI-tuned RF sensor for remote temperature sensing. Our RF sensor design is composed of two coils tuned to the operating frequency of the MRI scanner using the self-resonance of the copper wire wound into the solenoid coil. We place our sensor inside a dielectric material, i.e., low-concentration agarose gel, where its resonant frequency can be changed with temperature due to temperature dependence of permittivity. Temperature increase alters the permittivity and decreases the capacitance; thus, detunes of the RF sensor. Therefore, the signal intensity within the RF sensor in the MR image changes with temperature. We place two perpendicular RF markers and fill them with low concentration agarose gel to assure orientation independence during excitation with the MRI RF coils. We provide further characterization of the RF sensor, such as the angle limit between the sensor and the MR imaging slice and the image resolution limit. For the ideal results, the marker should be oriented with the slice, and image resolution

should be lower than a limit determined by the marker size. The local *in-situ* temperature is estimated from the MRI images using the calculated contrast difference between the RF marker and the surrounding tissue (Figure 2.1). Our *ex vivo* temperature measurement experiments in a porcine heart tissue demonstrate that the proposed RF temperature marker has high precision in the operating temperature range of 36-42 ℃. Therefore, it is possible to map absolute temperature with pre-calibration of the signal with a known temperature.

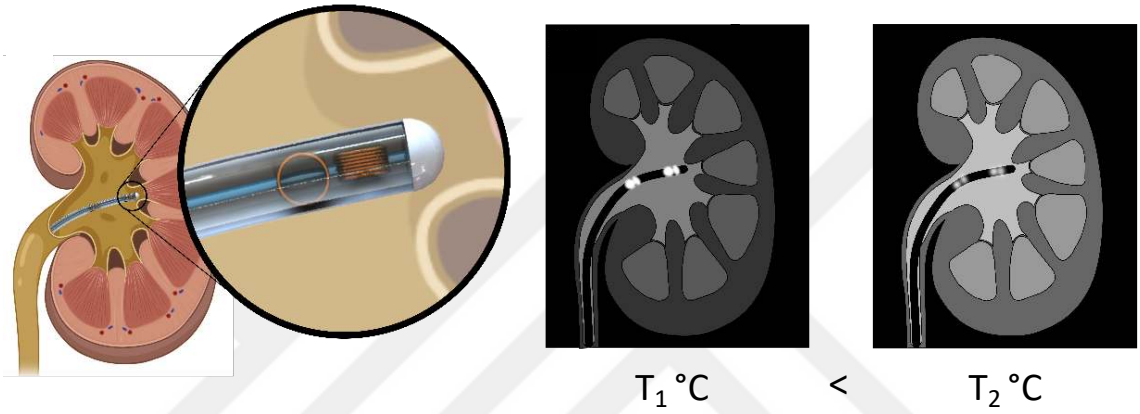

Figure 2.1: Conceptual schematic of the proposed RF sensor during a kidney operation. The RF sensor can be implemented in catheter operations, and the temperature can be monitored as the contrast created by the marker changes with the temperature.

2.2 Methods and Materials

2.2.1 Manufacturing of the RF sensor

MRI RF markers were manufactured by winding a 80-mm diameter insulated copper wire (Block, Germany) to a 14G hypodermic needle (Henke-Ject, Henke Sass Wolf GmbH, Germany). A layer of glue (Loctite 401, Henkel, Germany) was applied, and after drying, individual markers were cut. Manufacturing process and individual marker are shown in Figure 2.2 and Figure 2.3, respectively. Markers were trimmed and tuned one by one, using a Vector Network Analyzer (VNA, ENA20561B, Keysight Technologies, CA, USA). Using a coil loop attached to the VNA in the S11 mode, tuning measurements were done as markers submerged in water. Magnetic field pattern of the coils was also simulated in the COMSOL environment using a simplified axially symmetric electromagnetic module, to understand the distribution effective applied

magnetic field. A polyurethane catheter tube (Pellethane, Lubrizol, OH, USA) with a 2.8 mm diameter was used for temperature measurement experiments. Two markers were placed perpendicularly inside the catheter tube, filled and mechanically fixed with a low concentration agarose gel (Agarose, Sigma-Aldrich, MO, USA). The ends of the catheter tube were sealed to prevent ions in the Ringer's solution diffusing into the agarose and detuning the sensor.

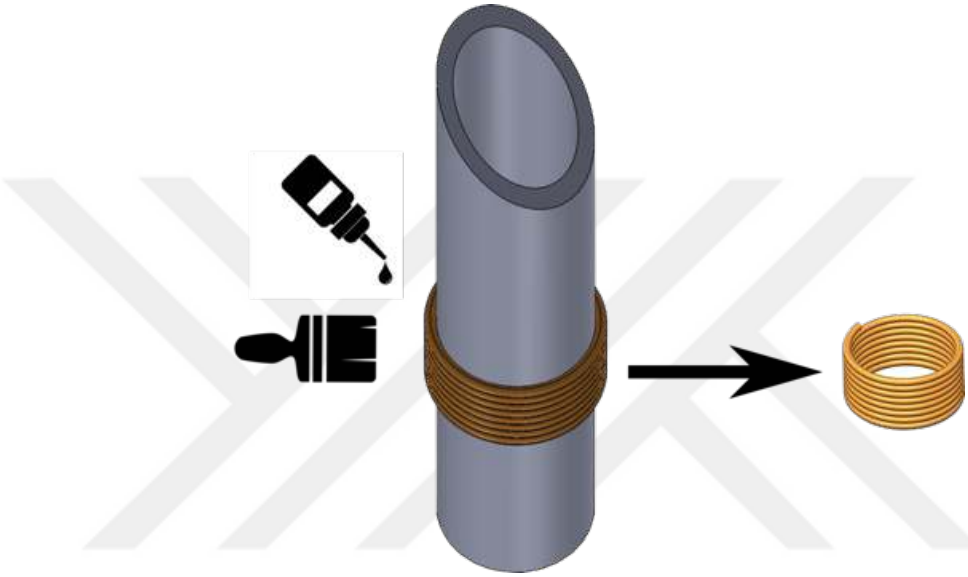

Figure 2.2: Manufacturing process steps of the RF markers. Copper wire wound around a needle and glue is applied to fix the shape. Removed markers are trimmed and tuned to the desired frequency.

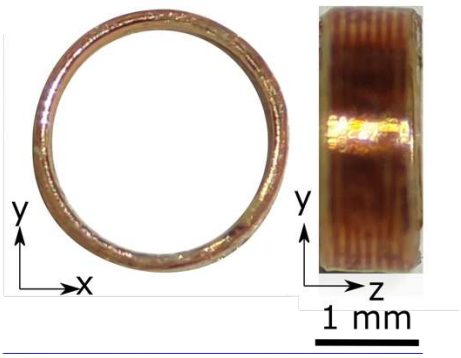

Figure 2.3: Individual marker, zoomed in.

Initial trials with the sensor included surface coils. In appendix A, design and manufacturing method of surface coils are provided.

2.2.2 MRI hardware and experimental setup

All MRI experiments were conducted in Max Planck Institute for Intelligent Systems. 7 Tesla preclinical small animal MRI (BioSpec 70/30, Bruker, Ettlingen, Germany) and 154 mm quadrature birdcage coil were used for MRI experiments. For sensor rotation experiments inside our MR scanner, a custom MRI-compatible horizontal rotating table was designed (Figure 2.4). The non-magnetic piezo motor and wires were kept outside the bore of the MRI to minimize any RF interference with MRI. A pulley attached to a piezo motor (LR23-50, PiezoMotor, Sweden), stationed at the MRI bore entrance, rotated the table with the help of a tight string. The piezo motor was used for horizontal rotation to rotate the table in 10° intervals inside the MRI. However, vertical rotations were done manually in 15° intervals. In *ex-vivo* experiments, a porcine heart tissue containing an artery was cut and placed in a sample box with polyvinyl tubing in a spiral pattern installed at the bottom for tissue heating experiments. The sample box was filled with Ringer's solution to increase heat transfer and placed in a styrofoam hold. A heated bath circulator (SC100-S5P, ThermoFisher Scientific, MA, USA) pumped hot water through the pipes and heat the heart tissue. A Catheter with two perpendicular markers was placed in one of the arteries, and an optical temperature probe (FOTEMP OEM-PLUS, Optocon, Germany) was placed next to it. MRI scans were conducted as temperatures were measured with the optical sensor as the ground truth.

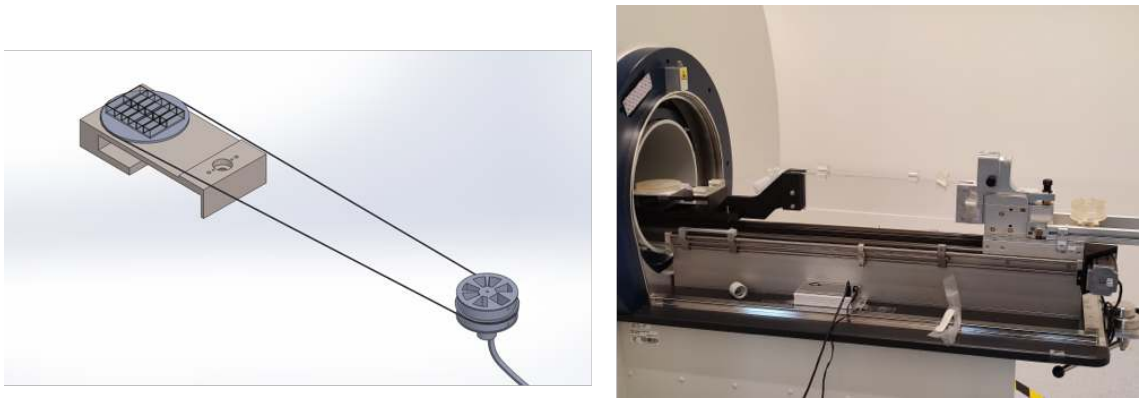

Figure 2.4: Rotation setup design and installation on the MRI stage. A piezo motor is used to rotate the table inside the MRI using pulleys connected by a string.

2.2.3 MRI imaging and data evaluation

In MRI experiments, a 2D non-slice selective GRE sequence was used. A minimum echo time of 3.438 ms and a minimum repetition time of 7.183 ms was used. 120×120 mm^2 field of view was imaged with 256×256-pixel matrix, if not stated otherwise. Single imaging sequence lasted around 1.8 s. 100 kHz excitation pulse bandwidth was used in all experiments, and the receiver coil bandwidth was set to 50 kHz. Pulse power was adjusted to have a flip angle of 0.2°. We have created an automated software routine to evaluate the RC values of RF markers in pixel size and rotation angle experiments. Our code detected corners of the sample box, therefore, the orientation angle of the sample box, and rotated it to 90°. After the correction rotation, it identified each sample well and checked for markers. For background signals, the signal of the water regions was used after removing markers from the image. Then the following formula was used for the calculation of the RC,

$$\mathrm{RC} = \frac{\max(marker) - mean(background)}{mean(background)}.$$

Equation 1: The calculation of the relative contrast (RC)

In *ex vivo* experiments, marker positions and selected background regions were manually given to code, and the software RC values were calculated. Then, calculated RC values were converted to temperature estimations by the software using the mapping relation. A sample code for automated RC evaluation is provided in appendix A.

2.2.4 Calculation of the resolution limit

Basically, with the resolution limit, our goal is to ensure a single pixel that falls entirely inside the maximum signal region of the marker so that one pixel will not fluctuate due to positioning to pixel projections. It is a requirement for reliable sensory measurement. In order to calculate this resolution limit, the length of the maximum signal region (l_{msr}) of a marker should be known, and l_{msr} must be larger than the two-pixel size. As positioning and pixel projections are assumed to be random, the pixel diagonal length should be used for calculations. For our marker, the diameter is l_{msr} since simulations show that the maximum signal is inside the marker. So, for our marker with a 2 mm diameter, the diagonal of the pixel should be 1 mm. That brings the

pixel size resolution to 0.707($\sqrt{1/2}$) mm. That is the resolution limit for our proposed marker design., RC mean values and their standard deviations with different resolutions are shown in Figure 2.5. Note that after 0.707 mm, mean values and deviations are converging.

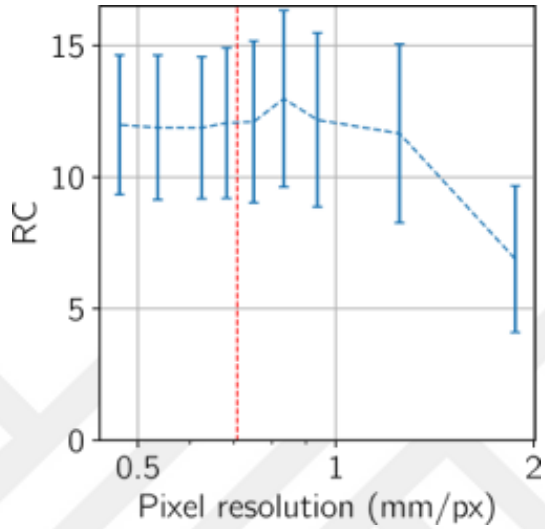

Figure 2.5: RC values of a marker in images with different resolutions. Markers are imaged in MRI in different resolutions and the RC values are calculated using the automated code. RC values stabilize after the resolution limit.

2.3 Experimental results

2.3.1 MRI-tuned RF marker design for remote in-situ temperature sensing

Previous research on MRI-tuned RF markers focused on the 3D localization and position tracking for MRI-guided robotic tools [18]–[20], [67]–[69]. Therefore, the main design objective of these studies was maximizing the coupling between the RF marker and MRI's own RF coils by precisely tuning the marker to the operation frequency of the MRI scanner, ensuring RF coupling robustness against any external physical stimuli. However, using RF markers for remote sensing requires a different design approach. The coupling between the RF markers and the MRI RF coils should be sensitive to the measured physical stimulus, as shown for our temperature markers in Figure 2.6.

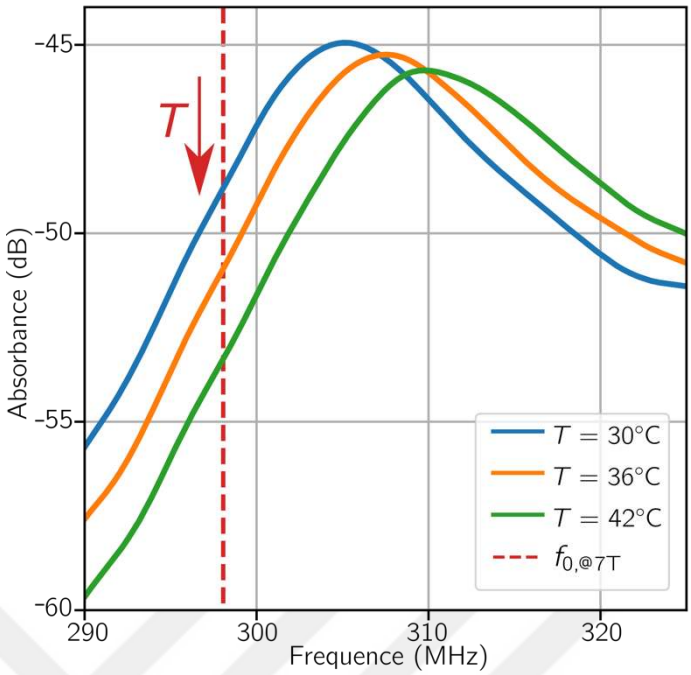

Figure 2.6: Desired response of the sensor resonance to the temperature change. The resonant frequency of the sensor shifts right with higher temperatures. The coupling with MRI, therefore the RC, decreases as the temperature increases.

We achieve a temperature-sensitive RF marker by excluding the lumped capacitor element from the design and using solely intrinsic capacitance (C_i) of our single-layer wound coil (Figure 2.6) to match the resonance frequency, $f_0 = \frac{1}{2\pi\sqrt{LC_i}}$. The circuit representation of the marker is given in Figure 2.7. Since temperature is the stimulus the marker is sensitive to, intrinsic capacitance is temperature dependent.

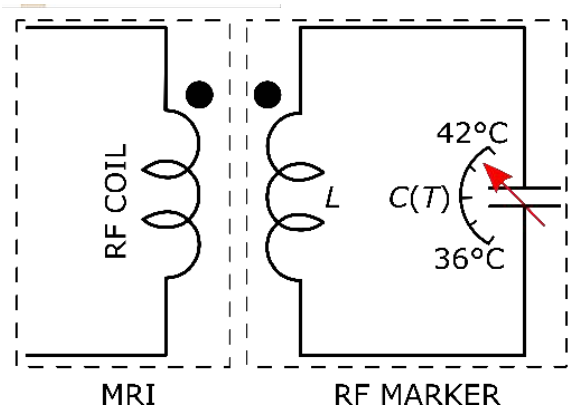

Figure 2.7: Circuit representation of the marker. The marker is inductively coupled to the RF coil of the MRI and has a temperature dependence capacitance.

Q factor of this circuit can be found using $Q = \frac{1}{R}\sqrt{\frac{L}{C_i}}$. After inserting calculated component values (R and L) and values that are derived from the resonant frequency equation (C_i), Q is found to be around 3200. As the flux through the marker is given as, $\Phi = \int^A B_1 da = \|B_1\|\|da\| \cos\theta$ where Φ is the flux through the marker, *da* is the surface normal vector of the marker and θ is the angle between B_1 field and the normal vector of the marker. Similarly, induced current within the marker (I) is obtained as $I = \frac{-1}{R}\frac{d\Phi}{dt}$. Since, in MRI, $B_1 = \begin{bmatrix} B_x & B_y & 0 \end{bmatrix}$ has no $\hat{z}$ component, marker should be placed perpendicular to the RF field and parallel to the z-axis in order to maximize the flux passing through. This implies any marker that is oriented or facing at z-axis has zero magnetic flux and no signal amplification.

For our single-layer winded coil design, most B_1 field amplification occurred inside the coil (Figure 2.8); therefore, it was placed inside a 1% agarose gel. Water-rich agarose gel provided a high density of ^{1}H protons for MR imaging. Moreover, high water content also provides a dynamic response range for temperature measurement due to large variation in relative permittivity of water, around 0.35℃$^{-1}$ between 20-40 ℃ [104], [105].

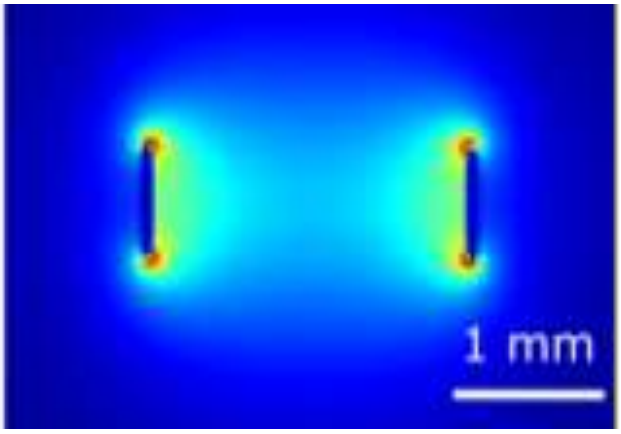

Figure 2.8: B_1 amplification distribution in the marker. 2D Axisymmetric simulation of the coil was done in COMSOL simulation environment. Most of the amplification is inside, near the coil.

Using only intrinsic capacitance is also advantageous to maximize the RF coupling between the marker and MRI RF coils. Since the resonant frequency is inversely related to both the inductance and capacitance, using only intrinsic capacitance enables larger

inductance in the circuit to match the frequency compared to a design with a lumped capacitor element. As a result, we could obtain a much larger coupling and higher quality factor with this sensor design. However, tuning RF markers with intrinsic capacitance is much more demanding than simple LC circuit tuning since both inductance and capacitance depend on geometric properties of the coil, i.e., its diameter and turn number. So, a tuning method with geometric manipulation has to be very precise.

We used a heuristic method to tune our coils for remote temperature sensing. The first step of tuning was to choose the resonant frequency region in which our coils operated. As shown in Figure 2.6, the main goal was to tune the resonant frequency such that coupling decreased linearly as temperature increased in the operational temperature range of 36-42℃. Thus, the marker gave a high-intensity MRI signal at lower temperatures and gradually lost signal strength with the temperature increase. This response was achieved by tuning the marker to the operating frequency of the MRI scanner (298 MHz for our 7T MRI) at room temperature 25℃. When it reached the body temperature of 36℃, resonant frequency shifted to higher frequencies. It is important to note that another linear response region could also be achieved by tuning the marker around 20 MHz less than the MRI's operating frequency at the body temperature. However, this would result in the temperature marker becoming visible only at high temperatures. Next, the effects of the coil diameter, turn number, and ambient temperature (Figures 2.9) on the resonant frequency were examined using a vector network analyzer (VNA). The final marker design in the desired temperature-dependent frequency regime was determined using VNA characterization results. In the rest of the study, we used coils of 2 mm diameter with 8.5 to 9 turns of winding. Each marker was individually tuned to the Larmor frequency of ^{1}H at 7 T at room temperature.

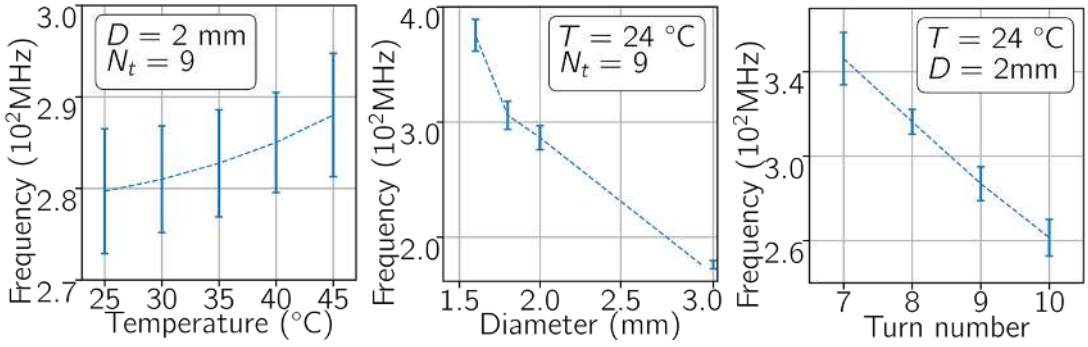

Figure 2.9: Effects of coil parameters on the resonant frequency of the marker. Markers with varying turn numbers and diameters were built, and the resonant frequency of the specified condition was measured with the VNA. Results were used for determining the final design.

2.3.2 MR imaging of the RF markers

In MR imaging, the spin excitation is proportional to transmit the RF magnetic field (B_{1+}). Flip angle (α) is a linear function of the gyromagnetic ratio (γ), the magnitude of the RF magnetic field (B_1), and the RF pulse duration (t_p) for small flip angles, where $\alpha = \gamma B_1 t_p$. Since RF markers amplify the local B_1 field, it increases the effective flip angle exciting the local spins. Therefore, we can take advantage of the amplified local B_1 to obtain a positive contrast between the RF sensor and tissue by imaging with very low flip angles[106]. This study utilizes created contrast difference to measure temperature using a metric for *relative contrast* (RC), the ratio of the maximum signal intensity from the RF sensor to the mean background signal.

The first step of the characterization is to determine the optimum applied flip angle for imaging RF markers. RF markers were submerged in deionized water and a gradient-recalled echo (GRE) sequence was performed with different flip angles and repetition times. The repetition time of the sequence directly affects the RC curve and the optimal flip angle value. The RC of different flip angles with different repetition times is shown in Figure 2.10. Longer repetition times provided higher RC but made sequences longer as well. To maximize the RC and minimize the sequence duration, a 0.2° flip angle and a minimum repetition time of 7.1 ms was used in the rest of the experiments. We also observed that as flip angles converged to 5°, RC was decreased as low as 4, at which the anatomical image could be seen. This observation suggests that the same MRI sequence can be used for imaging only markers at low flip angles and

tissue at higher flip angles. Lastly in flip angle characterization experiments, RF markers were tested at a 90° flip angle, highest RF excitation pulse used in imaging sequence to check any potential heating issues by placing a fiber optic temperature probe next to the marker. No RF marker-induced Joule heating was observed since B_1 amplification occurred on the agarose gel with virtually no ionic content.

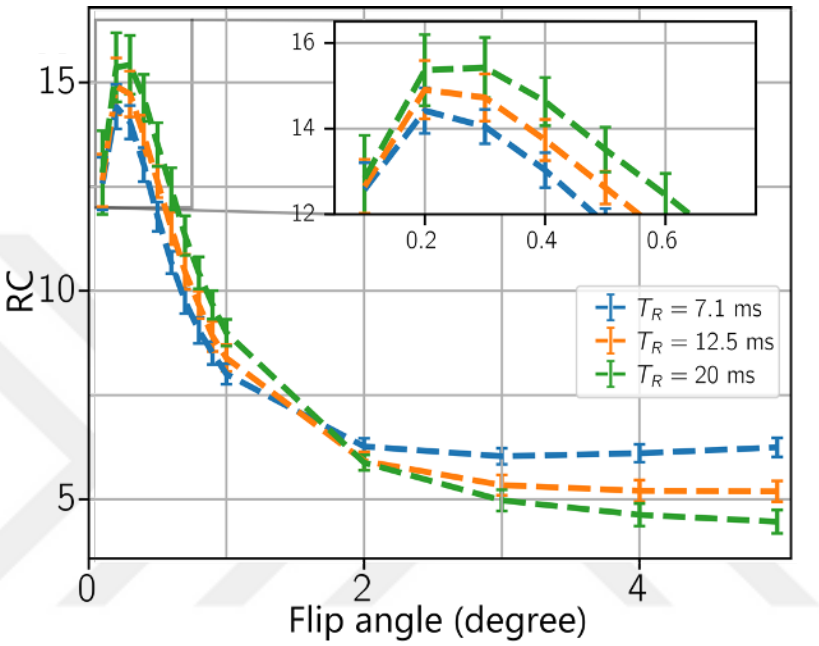

Figure 2.10: RC versus flip angle in different repetition times. RF markers were placed on a 12-well plate inside MRI and imaged with varying flip angles and repetition times. The optimal flip angle and repetition time pair were selected as 0.2° flip angle and 7.1 ms repetition time was selected.

The second factor affecting the marker signal is the marker and imaging slice orientation. MRI creates two circularly polarized RF waves in the *x*-*y* plane; therefore, markers should be oriented with the *x*-axis or *y*-axis for maximum signal amplification. On the other hand, any marker facing the *z*-axis, i.e., B_0 field, has no coupling with MRI RF coils; hence, it does not create signal amplification. In addition to RF coupling, the relative orientation of the RF marker to the MR imaging slice also affects the signal. 2D MR images are composed of projection of the volumetric signal in slice to the 2D slice plane. Since the B_1 amplification pattern of our coils was not uniform, as shown in Figure 2.8, higher signal was observed when the coil is facing the same direction with the MRI slice than when the coil was perpendicular to the MRI slice. Figure 2.11 gives a simple rule of thumb for combinations of the marker and slice orientations.

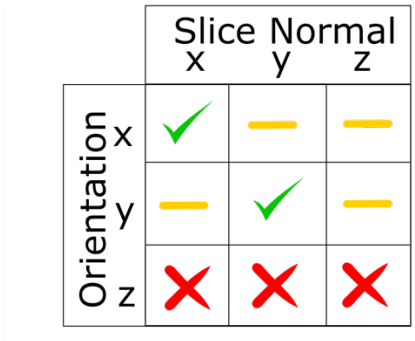

Figure 2.11: Desirable marker and MR imaging slice orientation combinations.

While Figure 2.11 summarizes the geometric effects in cardinal directions, the marker signal in other orientations is also necessary to use the markers in realistic procedures. Therefore, the orientations were examined with a custom motorized rotating stage. While keeping the image slice fixed, *y*-axis-oriented marker was first rotated around *y*-axis using the motorized stage and then around *x*-axis manually. In the end, the marker was oriented facing the *z*-axis, i.e., the B_0 field. RC of the marker during these rotations are reported in Figure 2.12, as the first and second rotations appear as orange and blue colors, respectively. While the marker could keep the RC when rotated around the *y*-axis, the signal disappeared completely during rotation around the *x*-axis. In light of these experiments, to ensure signal presence in every orientation, two perpendicularly placed markers were selected as the final design for temperature monitoring experiments.

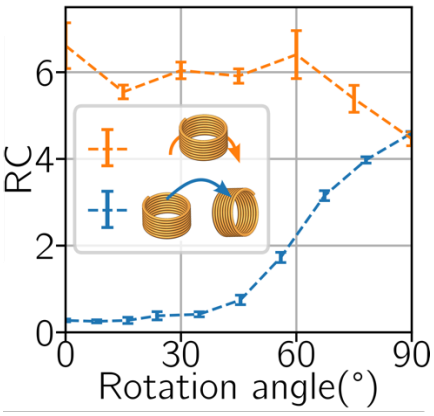

Figure 2.12:RF marker RC in different angles. Two perpendicular markers would ensure contrast in all orientations.

Another important factor for marker imaging is the spatial resolution. The obtained RC should be consistent and should not fluctuate between images to ensure reliable measurements. There is a natural resolution limit for robust measurements determined by the marker dimensions and orientation. The limit essentially suggests that at least one full pixel projection of the image should be positioned inside the marker, or rather the maximum signal region of the marker, so that the reading of that pixel gives solely the marker signal. If the resolution is larger than the limit, the projection of the pixel may not be positioned entirely inside the maximum signal region of the marker and, therefore, obtained RC might vary between images due to pixel positioning.

For the top facing marker of 2 mm diameter with the coronal imaging readout, the resolution limit was 0.707 mm. Stabilization of the signal standard deviation below the resolution limit is shown in Figure 2.13. For the resolution in the figure, multiple markers were moved in 1.5 mm steps inside MRI and are imaged in every step. The normalized mean and standard deviation of marker RC standard deviations of this experiment is provided in the figure. Given resolution on the *x*-axis was found as *Resolution = Field of View / Pixel Count*.

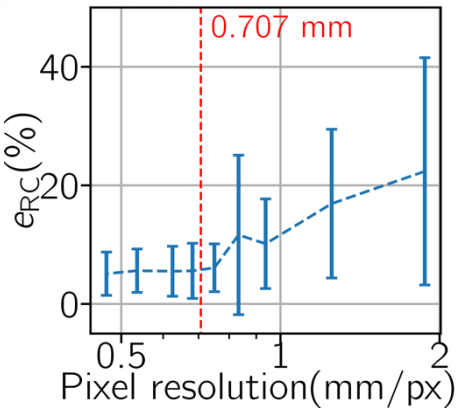

Figure 2.13: Deviation of RC values in images with different resolutions. After the resolution limit, the marker signal stabilizes and allows reliable sensor measurements.

MR images of the marker with different resolutions are provided in Figure 2.14. B_1 field distribution is visible through the signal in images, verifies the simulations in Figure 2.8. Pixel limits for markers in varying diameters with fixed turns for 298 MHz and their imaging sequence duration are provided in Table 2.1. The table shows a direct trade-off between resolution and imaging speed; hence, the MRI's spatiotemporal resolution is a limiting factor.

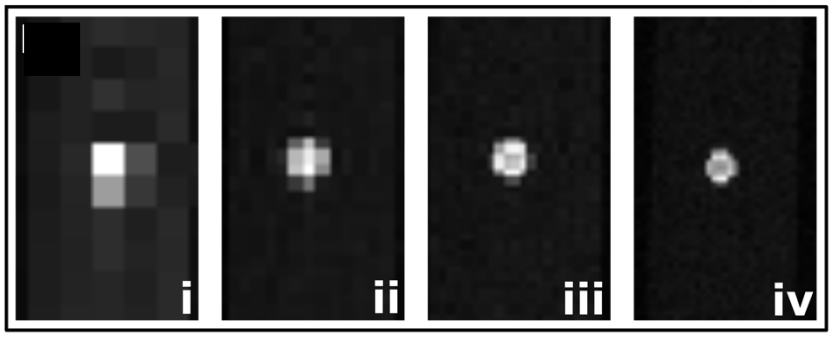

Figure 2.14: MR images of a marker in different resolutions. The distribution of the magnetic field amplification is visible in the image iv.

Diameter (mm)	Resolution (mm/pixel)	Sequence Duration (ms)
1.6	0.565	1336
1.8	0.636	1104
2	0.707	928
3	1.060	495

Table 2.1: Required resolution and the duration of the imaging sequence for markers with different diameters

To demonstrate the orientation-independent operation of our marker, *ex vivo* experiments in a porcine kidney was performed. RF sensor was attached to a commercial catheter tubing and the catheter was steered manually inside MRI while imaging. Images with different orientations are shown in Figure 2.15. RF sensor could be visualized in various orientations during the catheter navigation in the kidney.

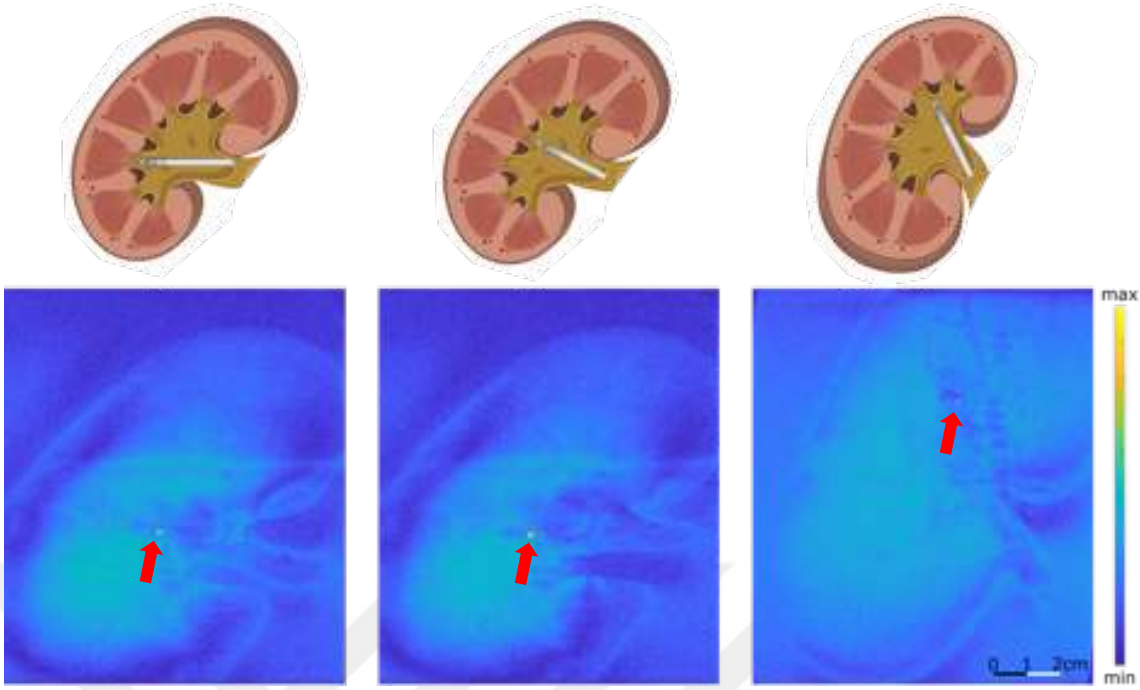

Figure 2.15: RF sensor operation in different orientations. Red arrows point the marker position in the MR image. The sensor is trackable in all orientations.

2.3.3 Ex vivo temperature measurements inside MRI

Before starting with the *ex vivo* temperature measurements, a mapping curve must be set. Raw MRI signals cannot be used for direct measurement since they are tissue sensitive and prone to background interference. Therefore, RF markers tuned to linear temperature response regime at 298 MHz were placed in water baths with different thicknesses, and an optical temperature probe was placed next to the RF marker to measure reference temperature. First, the RF coil of the MRI scanner was tuned to the signal from 40°C to have high RF coupling with water between 30-50°C. Then, the water was heated to 50°C. The samples are continuously imaged using GRE sequence t_E/t_R=3.438/7.183 ms with 0.2° flip angle during convective cooling of water. Since the relative permittivity of water is temperature dependent [104], [105], marker signals change with temperature. RC values of an RF marker as a function of temperature are shown in Figures 2.16. It can be observed that created RC is inversely proportional to the thickness of the background water, but the relation is non-linear. This is due to the signal integration characteristic of the MR slice imaging since 2D GRE sequences were used for this experiment. Moreover, while the temperature dependence of RC is

relatively linear around 40 °C, non-linearity in lower and higher temperatures due to the detuning of the MRI scanner's RF coils were observed. However, since the temperatures are expected to be 36-42°C during medical procedures to avoid tissue damage, this non-linearity is not important in clinical applications.

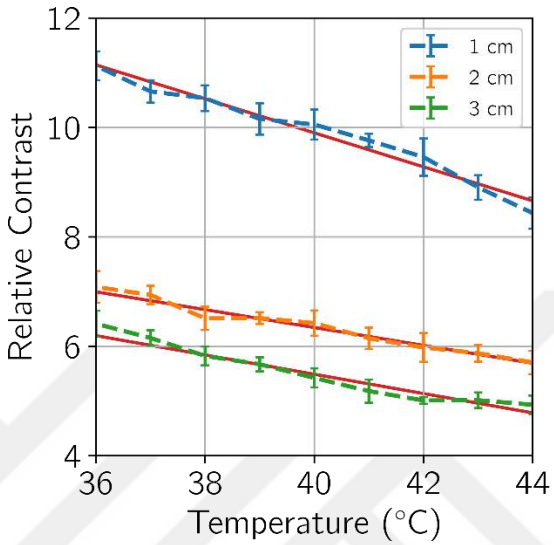

Figure 2.16: RC values of markers in different water thickness. RC values decrease with the temperature increase. The fitting line for the 1 cm water is used for temperature mapping in ex vivo experiment.

The MRI relaxation values of the actual tissue are different from water; therefore, we need an additional mapping measurement to estimate the temperature. A linear line was fitted to the mapping data from Figure 2.16 to estimate the temperature with *ex vivo* experiment RC values. Since relaxation values are not changing significantly for our marker and tissue with temperature, we introduced a scaled RC, $RC^*(T) = RC_{\text{water@36°C}}.RC_{\text{tissue}}(T)/RC_{\text{tissue@36°C}}$, using an initial calibration measurement obtained at 36°C from the tissue. Finally, we obtain the following linear estimation, $T_{est} = c_1 RC^* + c_2$, where c_1 and c_2 are the line parameters fitted to data from corresponding water thickness.

Porcine heart tissue was used to perform the *ex vivo* temperature measurement experiments. 10 mm-thick heart tissue was cut to be 50-80 mm^2 rectangular shape. The RF temperature marker made of two RF markers in a catheter tube was placed inside the artery, as shown in Figure 2.16. An optical temperature probe was also placed near the RF marker to measure the real temperature. The tissue was placed in a sample box which was thermally insulated with styrofoam. Then, the tissue was heated by hot water

circulation through the tubing at the bottom of the sample box. Calibration RC was recorded at $T = 36$ ℃. Then, the temperature was estimated by imaging the tissue approximately every 2 minutes. The temperature estimation and actual temperature values are shown in Figure 2.17. The temperature estimation experiment was repeated three times, and the mean square root (RMS) error in these experiments was calculated as ± 0.6 ℃ for three experiments.

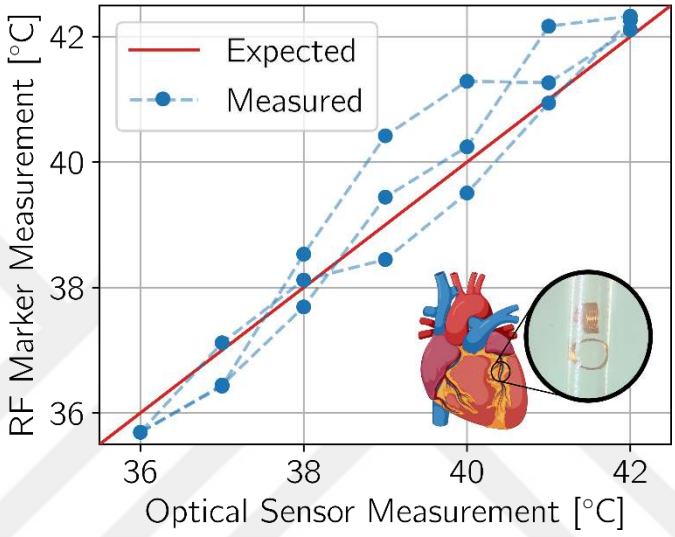

Figure 2.17: Ex vivo temperature measurement with marker. Measured RC values were mapped to temperatures using the 1 cm water data in Figure 2.16. Estimated temperature values have around ± 0.6 ℃ RMS error.

2.4 Discussions

In this study, we demonstrate a remote temperature measurement method based on an RF-resonator tuned to the 7T MRI RF resonance frequency (298 MHz). Proposed RF sensor can be used as remote *in-situ* temperature probes and position tracking markers for interventional tools, such as a catheter. We demonstrate temperature measurement precision comparable to the MRI thermometry sequences [21], [22], [24]. In contrast to MRI thermometry methods, we measure temperature using a basic GRE MR imaging sequence without the need for alternating between anatomical and thermometric MRI images. Therefore, the proposed method can achieve a higher feedback rate for both position and temperature measurements.

Moreover, we used a heuristic RF marker tuning approach to tune markers with different sizes to the working frequency of our 7T MRI scanner. Although the 7T MRI scanner enabled to downscale marker diameter as small as 2 mm, the size of the marker was mainly limited by the MR imaging resolution. Similar markers can be developed with 1.5 or 3 Tesla MRI scanners, but larger coils with higher turn numbers is needed. Another important step is the packaging and insulation of the marker to prevent shifting the resonant frequency by the ionic content in the medium. In this study, insulation was achieved by confining the two markers inside a catheter tube, but markers that have open contact with bodily fluid could be tuned accordingly. Moreover, our marker design is restricted to a simple solenoid geometry; however, many different RF marker manufacturing methods have been proposed [18], [20], [69], [102], [107]. Different antenna designs can provide RF markers with less footprint in future studies.

RF markers that are capable of measuring the temperature can be useful for interventional catheter and laser ablation procedures inside an MR scanner. A fast feedback rate for position and temperature information can enable higher control over the dose and targeting of the treatment. For example, in laser ablation operations, the exposure time and laser power could be controlled for safer treatment, and in active catheter operations, continuous and rapid feedback rate in both catheter temperature and position would make applications safer.

Although only remote temperature measurement was investigated in this study, other biological stimuli could also be targeted by leveraging environment-dependent intrinsic parameters of RF markers as a future work. Many other stimuli, such as ionic content, ion concentrations [108], and physical deformations [109], can be employed for this sensory response. Hai et al. demonstrated that a similar system could be used in biological investigations [30]. Body fluids and tissues have varying permittivity [110], [111] and, when markers are designed to be selectively responsive, this could be used as a flag mechanism for tissue selection. Markers sensitive to other stimuli would make catheter operations more functional.

One aspect that requires further examination is the measurement during the marker (i.e., device) in motion. All of the measurements were conducted in this study when the RF sensor was stationary. As motion can create undesirable artifacts in image reconstruction and hinder measurement, there are studies on motion correction methods for moving RF markers [112]. Sparse reconstruction and phased coil array techniques

could be used to address motion-artifact problems [113], [114]. *In vivo* conditions also have similar motion challenges, such as heart beating. Cine imaging [115] can be employed for temperature measurements near an active heart in future studies. Furthermore, integrating the sensory software to MR imaging would help achieve more accurate control of interventional medical devices. Marker localization, tool position and orientation tracking with multiple markers, and conversion of signal data to sensory readout algorithms can be developed for automation. Such algorithms would give the tool controller all the vital information it requires for safe operations.

Clinical applicability and safety concerns of interventional active medical tools require new functional RF markers with similar and new sensory approaches. In addition, we expect similar and new RF marker designs specialized for various environmental stimuli that would add more functions to MRI-guided interventional tools. Thus, the proposed RF marker-based remote sensing could be an integral part of future MRI-guided active catheters [5], [50], [71], [116], [117] and endoscopic tools [47], [118]–[120].

Chapter 3:
POLYACRYLIC ACID COATED MAGNETIC NANOPARTICLES AS DUAL-MODE MRI CONTRAST AGENTS

3.1 Background

3.1.1 MRI Contrast agents

Contrast agents are crucial for MRI, as more than 40% of the imaging procedures are done with contrast agents [121], [122]. Through the years, countless contrast agents have been proposed [123]–[130]. There have even been organ-specific agents that enable the detection of hard-to-see tumors [131].

The physics of the contrast agents rely heavily on quantum physics, specifically on the spins of protons. Every elementary particle has a spin, sometimes referred to as the magnetic moment. The magnetic moment is a physical property that particles have in quantized levels. Normally, spins of particles are randomly distributed in all orientations, meaning the net vectorial sum, the net magnetization, is zero. However, when a magnetic field B_0 is applied, spins interact with the magnetic field and tend to align themself with the magnetic field. This alignment results in a non-zero net magnetization, M_0. In this state, particles do not spin in a fixed axis but precess around it. The frequency of this precession is found using Larmor's equation, $f_0 = \gamma * B_0$, where γ is the gyromagnetic ratio and B_0 is the magnitude of the applied magnetic field. In MRI, the proton of the hydrogen in the water molecule is used as the particle imaged. For that proton, the gyromagnetic ratio is $\gamma = 42.58\ MHz/Tesla$. In this study, a 7 Tesla MRI is used; hence, the frequency of the precession is 298.06 MHz.

This value is important because when an RF pulse with the same frequency, 298.06 MHz, is applied, protons absorb this wave and changes its orientation. This only happens if the frequencies match. The angle of deviation, the flip angle, is related to the amplitude of the RF pulse.

Spins interact with the magnetic field and adjacent proton spins in this excited state while slowly decaying. This decay happens in two relaxation mechanisms, longitudinal and transverse. Both relaxations are exponential decay, fast at first and getting slower as

time passes. In the longitudinal relaxation, under the effect of main magnetic field B_0, net magnetization slowly returns to the initial state, as shown in Figure 3.1. This relaxation is characterized by the T1 relaxation time, the net magnetization in the *z-axis* is derived as $M_z = M_0\left(1 - e^{-\frac{t}{T1}}\right)$.

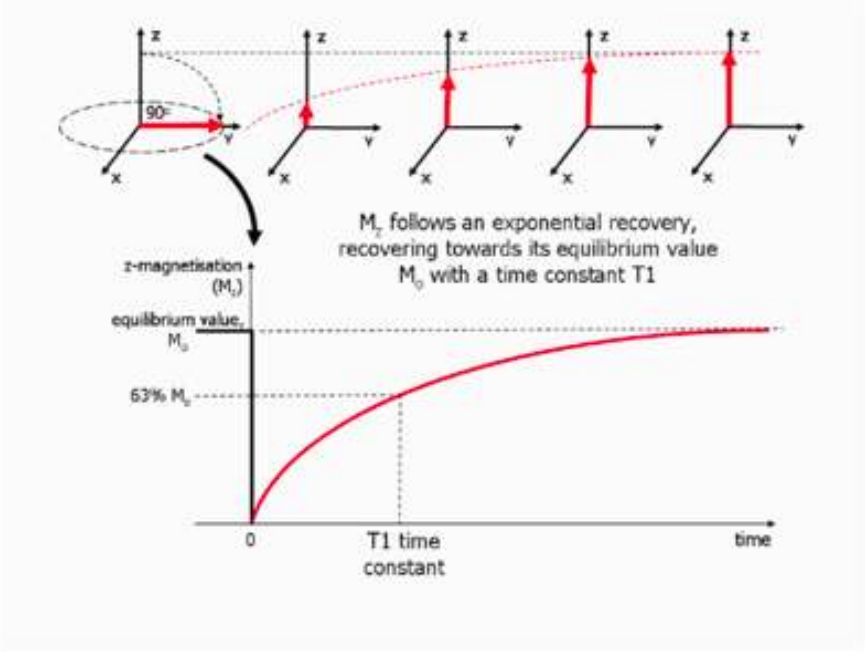

Figure 3.1: T1 (longitudinal) relaxation mechanism [132].

In transverse relaxation, the excited spins lose their coherence and start to dephase, as shown in Figure 3.2. Since their spins are still oriented in the *xy-plane*, this relaxation is named transverse relaxation and characterized by the T2 relaxation time. The net magnetization in the *z-axis* is derived as, $M_{xy} = M_0\left(e^{-\frac{t}{T2}}\right)$.

In general, T1 relaxation is based on the interaction with the B_0, while interactions with surrounding spins and other fields account for T2 relaxation. For pure water, T1 relaxation time is larger than T2 relaxation time, which means T2 relaxation is faster and more dominant.

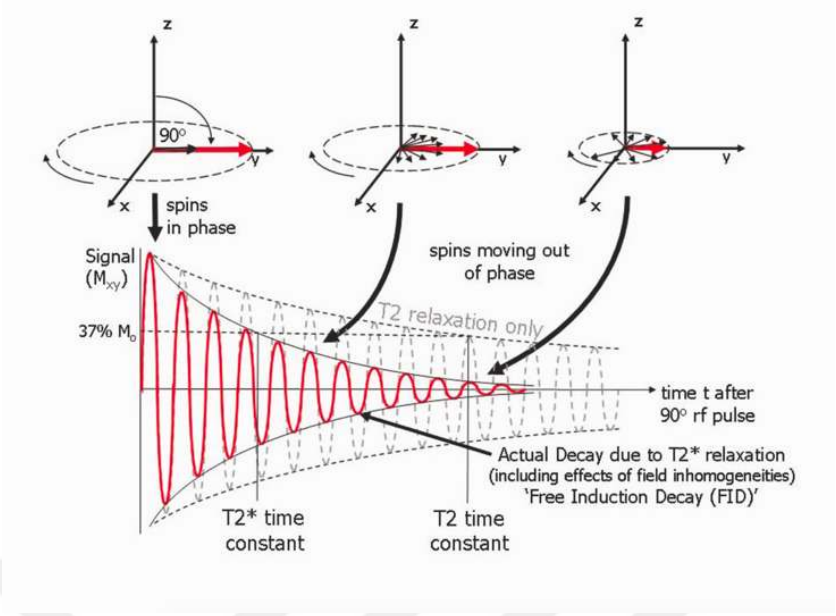

Figure 3.2: T2 (transverse) relaxation mechanism [132].

Contrast agents decrease the relaxation time of the surrounding protons to have faster relaxation and stronger signals. T1 contrast agents appear as positive(bright) in images, while T2 contrast agents appear negative(dark) in MR images. There have been numerous studies for both the T1 contrast agents [124], [128], [133], [134] and T2 contrast agents [125], [135], [136], as well as dual-mode contrast agents in which the contrast type changes with concentration or stimuli [123], [129], [137], [138].

The ideal contrast agent is expected to be biocompatible, small for tissue permeability, and has long blood circulation. Biocompatibility is one of the significant criteria for contrast agents as clinicians highly seek after it. Furthermore, prolonged blood circulation is essential due to the long duration of full-body MRI sequence. Biodistribution of the contrast agent is also a crucial factor which influenced by the size and the charge of the nanoparticle.

SPIONs have been on and off the market in US, EU and Japan. The commercialized SPIONs are shown in Tables 3.1, 3.2 and 3.3. Negative contrasts indicate T2 contrast, while the positive indicates T1 contrast. As can be seen from the tables, large aggregated SPIONs are usually used for liver imaging due to quick uptake of macrophages while small clusters circulate in the blood longer allowing angiography and imaging of lymph nodes [139]. Here, we will explore the MR contrast enhancement of small PAA-SPION nanoparticles.

Short name	Generic name	Trade name	Enhancement and physiochemical effects
Mn-DPDP[c]	Mangafodipir trisodium	Treslascan	Positive/liver
Gd-EOB-DTPA[a]	Gadoxetate	Primovist, Eovist	Positive-ionic-linear/liver
Gd-BOPTA[a]	Gadobenate dimeglumine	MultiHance	Positive-ionic-linear/liver
AMI-25[a]	Ferumoxides (SPIO)	Endorem, Feridex	Negative/liver
SH U 555 A[c]	Ferucarbotran (SPIO)	Resovist, Cliavist	Negative/liver
AMI-227[c]	Ferumoxtran-10 (USPIO)	Sinerem, Combidex	Positive or negative/lymph nodes
Gadofluorine-M[b]	-	-	Positive/(lymph nodes, CNS)
Mn-DPDP[b]	Mangafodipir trisodium	-	Positive/myocardium
Dy-DTPA-BMA[b]	Sprodiamide injection	-	Negative/myocardial and brain perfusion
Gd-DTPA-mesoporphyrin[b]	Gadophrin	-	Positive/myocardium, necrosis

[a], Agents available for clinical application; [b], agents being developed or development discontinued; [c], agents withdrawn from market. Gd-DTPA, gadolinium (III) diethylenetriamine pentaacetate; Mn-DPDP, manganese dipyridoxyl diphosphate; SPIO, superparamagnetic iron oxide; USPIO, ultrasmall super paramagnetic iron oxide; Gd-EOB-DTPA, gadolinium ethoxybenzyl diethylenetriamine pentaacetate. This table has been modified from http://www.magnetic-resonance.org/ch/13-01.html.

Table 3.1: Names and contrasts types of commercial contrast agents[Reprinted from 126]

Table 2 Properties and applications of some superparamagnetic iron oxide *(SPIO)* agents. The main references for this table are: for AMI-121 [20]; for OMP [1]; for AMI-25 [2, 22]; for SHU 555A [2, 18, 78]; for AMI-227 [25, 26, 27, 29]; for NC100150 [19, 24]

Agent	Particle size	Target organs	Dose[a]	Mode of administration
AMI-121	300 nm	GI lumen	1.5–3.9 mmol^{-1} l Fe 400–600 ml	p.o.
OMP	3.5 μm	GI lumen	0.5 g/l 400–600 ml	p.o.
AMI-25	80–150 nm	Liver/spleen	15 μmol Fe/kg	Slow infusion
SHU 555A	62 nm	Liver/spleen	8 μmol Fe/kg	Bolus injection
		Perfusion[b]	4–16 μmol Fe/kg	Bolus injection
		MRA[b]	10 μmol Fe/kg	Bolus injection
AMI-277	20–40 nm	Lymph nodes	30–45 μmol Fe/kg	Slow infusion
		MRA[c]	14–30 μmol Fe/kg	Slow infusion
NC100150	20 nm	Perfusion	7 μmol Fe/kg	Bolus injection
		MRA	50–100 μmol Fe/kg	Bolus injection

[a]The doses of SPIO agents may vary with imaging sequences and target organs: highly T2/T2*-weighted sequences require a smaller dose, T2* gradient echo sequences require a smaller dose than T2W SE sequences. Please refer to the information provided by the vendors and up-dated references for exact dosing

[b]Perfusion imaging and MR angiography are not the primary goals of SHU 555A. However, when properly administered and imaged, perfusion images and MR angiographic images can be obtained with SHU 555A

[c]MR angiography is not the primary goal of AMI-277. However, when properly administered and imaged, MR angiographic images can be obtained with AMI-277

Table 3.2: Sizes of the contrast agents and their applications[Reprinted from 139]

*r*1 and *r*2 relaxivities of MFs with different stabilizers measured at 0.47 T, 25 °C.

Sample name (hydrodynamic size of MNPs)	$r1$ ($mM^{-1} s^{-1}$)	$r2$ ($mM^{-1} s^{-1}$)	$r2/r1$
MF (140 nm)	27.8 ± 0.7	297.9 ± 7.6	10.7
NaOA-MF (159 nm)	4.5 ± 0.3	176.4 ± 6.8	39.2
PAA-MF (172 nm)	17.7 ± 0.6	186.5 ± 8	10.5
CA-MF (150 nm)	15.7 ± 0.9	143.9 ± 32.8	9.2
Resovist (63 nm)	40 ± 0.7	291.8 ± 8.8	7.3
Pluronic F127/OA-MNPs (71 nm) [19]	1.33 (37 °C)	63.4 (37 °C)	47.7 (37 °C)
Resovist (65 nm) [19]	24.9	177	7.1
Sinerem (17–20 nm) [20]	23 (37 °C)	53 (37 °C)	2.3 (37 °C)
Endorem (58 nm) [20]	24 (37 °C)	107 (37 °C)	4.46 (37 °C)

Table 3.3: Contrast agents r1 and r2 values at 0.47 Tesla[Reprinted from 140]

3.1.2 Polyacrylic acid-coated superparamagnetic iron oxide nanoparticle (SPION-PAA)

SPIONs are single domain superparamagnetic crystals with high saturation magnetization. They are known to be biocompatible and biodegradable, although very slow [141]. These properties attracted attention in many disciplines, from robotics to medicine. These versatile particles are multifunctional and have been used in various applications; hyperthermia therapy [31], [32], drug delivery [37], gene therapy [35], [36], photopolymerization and 3D printing [34], [142], actuation [33], magnetorheological fluid [143] etc. Furthermore, there have been many different SPION-based commercial contrast agents, some of which are organ specific, in the market.

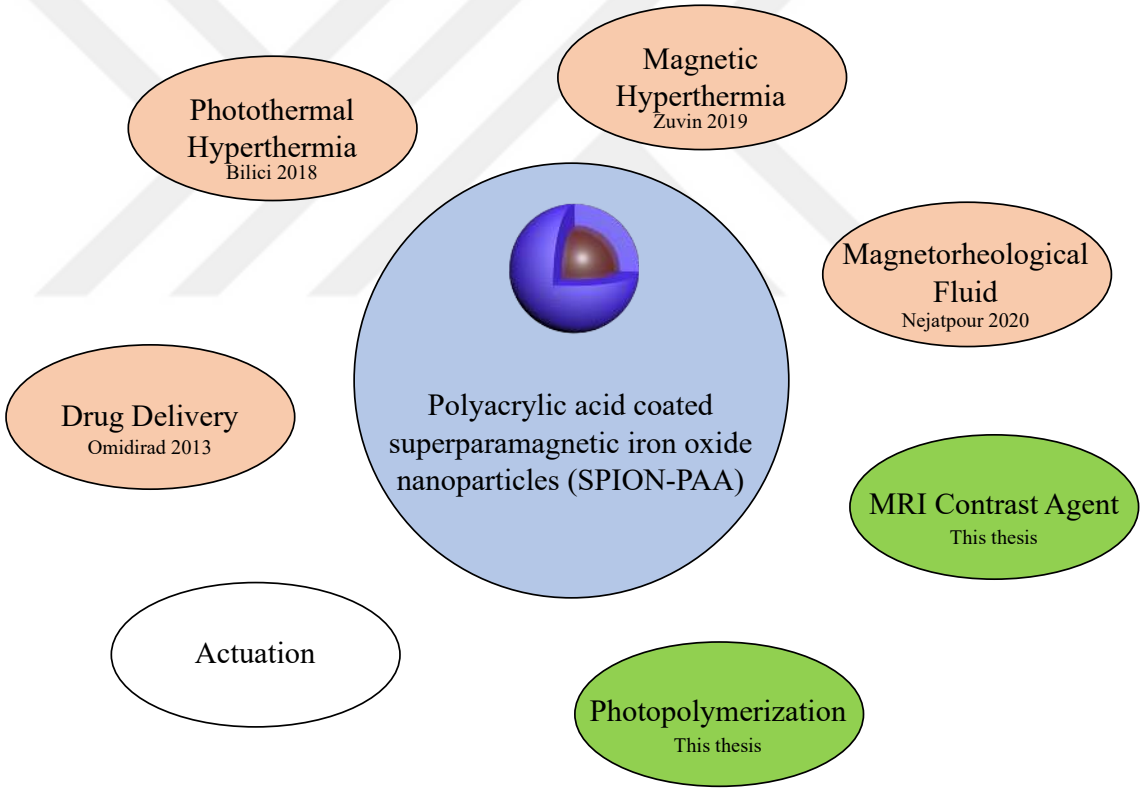

Figure 3.3: Applications of SPION-PAA

Since the surface properties govern the nanoscale world, the choice of coating of the SPION is also known to be essential. There have been numerous works with different SPION coatings and functionalized surfaces [32], [135], [138], [142]–[147]. Hydrophilic coatings are especially desired in this work for water penetration to boost the signal in MRI.

This chapter presents polyacrylic acid-coated SPION as a biocompatible dual-mode contrast agent due to its hydrophilic coating, small and non-agglomerated structure. Synthesis optimization, characterization, and biocompatibility of these SPION-PAA has been already proven in the in vitro studies by Yagci Acar et al., previously [31], [36]. These SPIONs have also been shown to have photothermal therapy and drug delivery potential in vitro or in vivo [32], [147], [148]. Hence, they have a tremendous theranostic potential in combining MRI with photothermal therapy and/or drug/gene delivery.

T1 and T2 contrast from PAA_SPIONs were achieved in aqueous colloidal solutions of the SPIONs at different concentrations. T1 contrast was also demonstrated using PAA-SPION in ex vivo mice experiments.

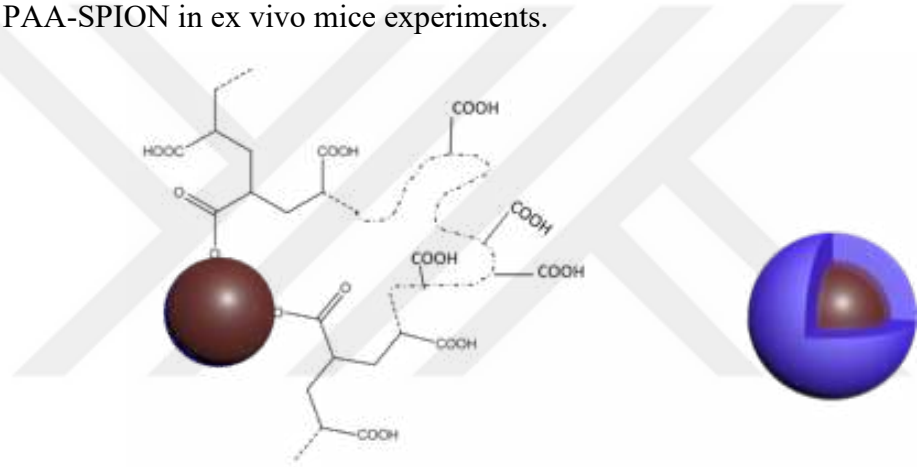

Figure 3.4:Polyacrylic acid coated SPION, with polyacrylic acid chemical structure and SPION-PAA core-shell visualization.

3.2 Methods and Materials

3.2.1 Synthesis of Polyacrylic acid coated SPION

Synthesis of the nanoparticles was done by Mona Nejatpour as described in work by Nejatpour et al. and by Bilici et al. [31], [143]. Briefly, iron salts ($FeCl_3 \cdot 6H_2O$ and $FeCl_2 \cdot 4H_2O$) were dissolved in degassed water with nitrogen gas at a 2:1 mole ratio of $Fe^{3+:}$ Fe^{2+}. Then, 2 g PAA was added to the reaction flask under nitrogen flow. The reaction flask was heated to 85 °C using the oil bath, and 4.63 mL of NH_4OH (4.5 M) was injected under vigorous stirring. The reaction was terminated after 30 minutes and cooled down to room temperature. The solution was placed on a magnet overnight to remove any precipitated particles. Finally, SPION-PAAs were washed with deionized water using 30 kDa MW cutoff centrifuge filters and stored at room temperature.

3.2.2 Characterization of the Particles

Hydrodynamic sizes of the SPION-PAA particles were measured with Dynamic Light Scattering (DLS) technique (Möbius, Wyatt Technologies, USA).

Transmission electron microscopy(TEM) imaging of the SPION-PAA is done in Stuttgart Center for Electron Microscopy. Solution samples were dried on copper grid in room conditions overnight and imaged with 200 kV transmission electron microscope (CM200, Philips, the Netherlands).

For VSM measurement of the SPION-PAA, solution drops were poured on a pre-weighed glass substrate and weighed after drying in room conditions to find the nanoparticle amount. The amount was measured to be around 2 mg. Super glue was applied to fix dried particles on the glass and the measurement is done (EZ7, MicroSense, USA). TEM and VSM measurements were done with the help of Anitha Shiva.

3.2.3 T1-T2 contrast in solution

All experiments were done in 7 Tesla small animal MRI. Small quadrature birdcage coil with 40 mm inner diameter was used in all MRI experiments. T1 and T2 experiments, SPION-PAA solutions were prepared in the following iron concentrations; 0.023 mg/mL, 0.046 mg/mL, 0.069 mg/mL, 0.092 mg/mL, 0.11 mg/mL, 0.13 mg/mL, 0.16 mg/mL, 0.18 mg/mL, 0.23 mg/mL, 0.27 mg/mL, 0.37 mg/mL, and 0.46 mg/mL. Solutions were put in 1 mL syringes, closed with rubber cap and stacked in MRI stage. Experiment was repeated several times in different concentration ranges. T1-weighted RARE and T2-weighted MSME imaging sequences are used for solution experiments. In the postprocessing, T1 and T2 values are evaluated using ImageJ software (NIH, USA).

3.2.4 T1 and T2 contrast in ex vivo mice

Ex vivo mice experiments are done with dead C57BL/6 WT mice. Two injection sites were determined around the muscle tissue on the back of the mouse and shaved for easy access. For an accurate comparison, a preliminary scan was done on the mouse before administering the SPION-PAA. SPION-PAA solutions were prepared in varying

concentrations, and 20 µL solution was administered to each site. FLASH and RARE imaging sequences were used in all mice experiments.

3.3 Experimental results

3.3.1 Characterization of SPION-PAA

SPIONs dispersed in water have a diameter of 50 nm suggesting the formation of small clusters, as shown in Figure 3.5.

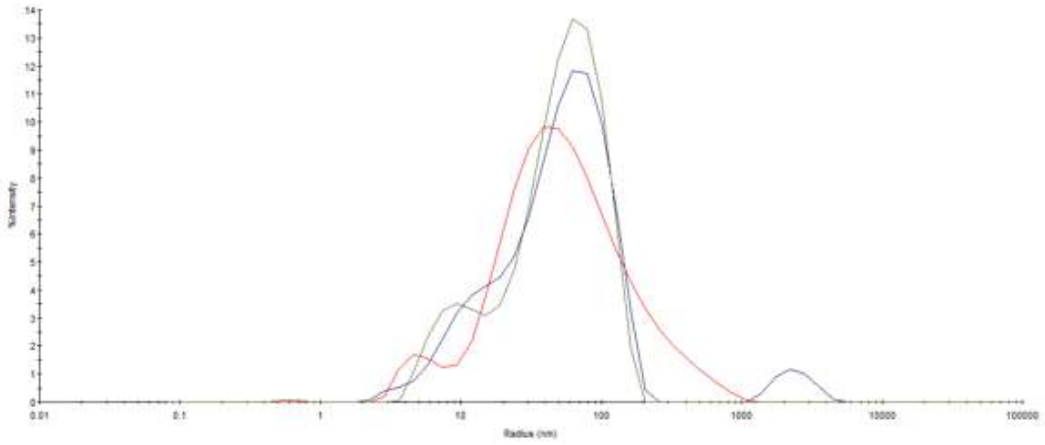

Figure 3.5: DLS results of the SPION-PAA.

TEM images showed individual particles as well as aggregated ones due to the drying method. Figure 3.6 shows particle distribution on the copper grid.

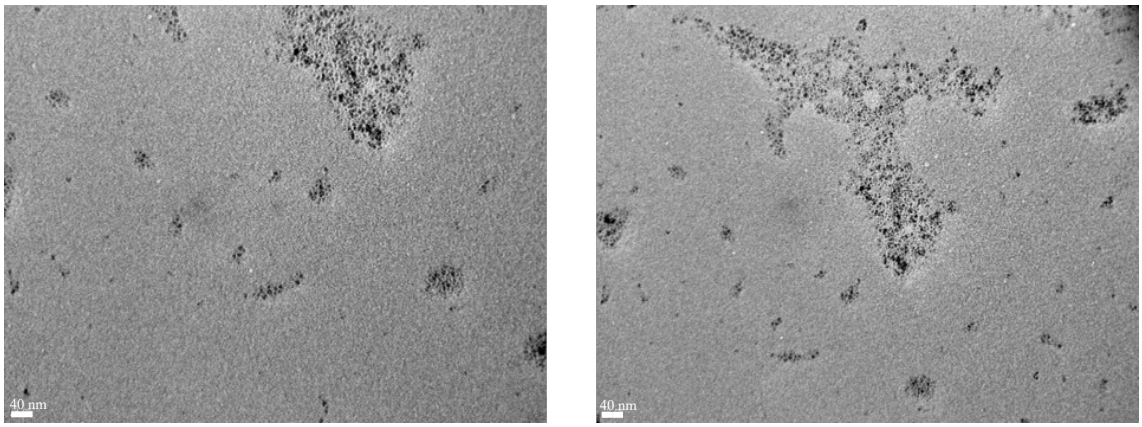

Figure 3.6: TEM images of the SPION-PAA particles, scale bar: 40 nm.

VSM measurements showed high magnetization of the particles. Due to the instrument limitations, the saturation could not be observed clearly.

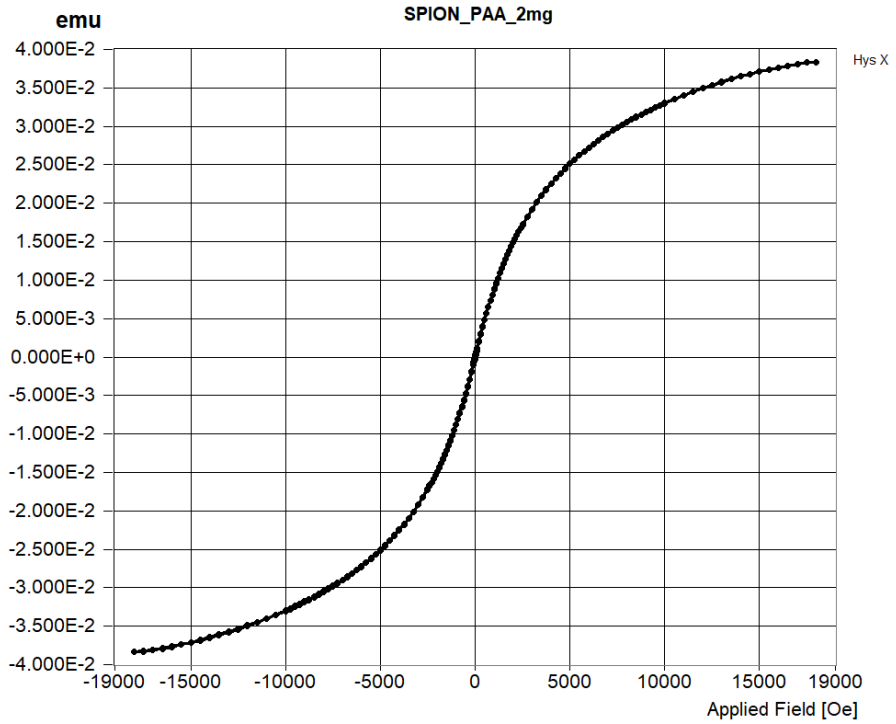

Figure 3.7: VSM measurement of the SPION-PAA.

Thus, the sample has around 20 emu/g.

3.3.2 T1-T2 contrast in solution

MR images were obtained from MRI, as shown in Figure 3.8.

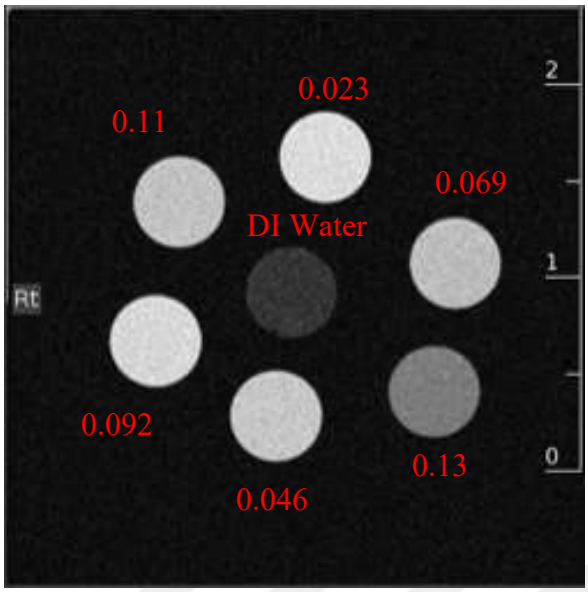

Figure 3.8: T1-weighted RARE sequence image of SPIONs. Concentrations are given on the imaged.

r1 and r2 values were obtained using the derived T1 and T2 values from ImageJ. Calculated r1 and r2 values as a function of the iron concentration were shown in Figures 3.9 and 3.10, respectively. r1 value is calculated to be around 700 mM^{-1} s^{-1} and r2 value is calculated to be around 9750 mM^{-1} s^{-1}.

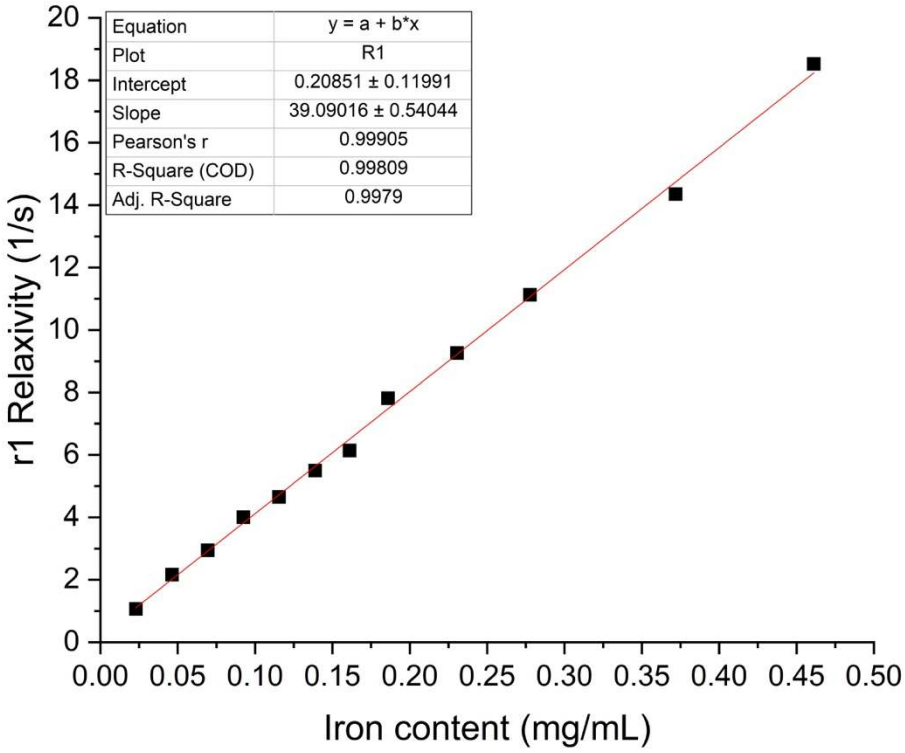

Figure 3.9: r1 values of SPION-PAA as a function of iron content

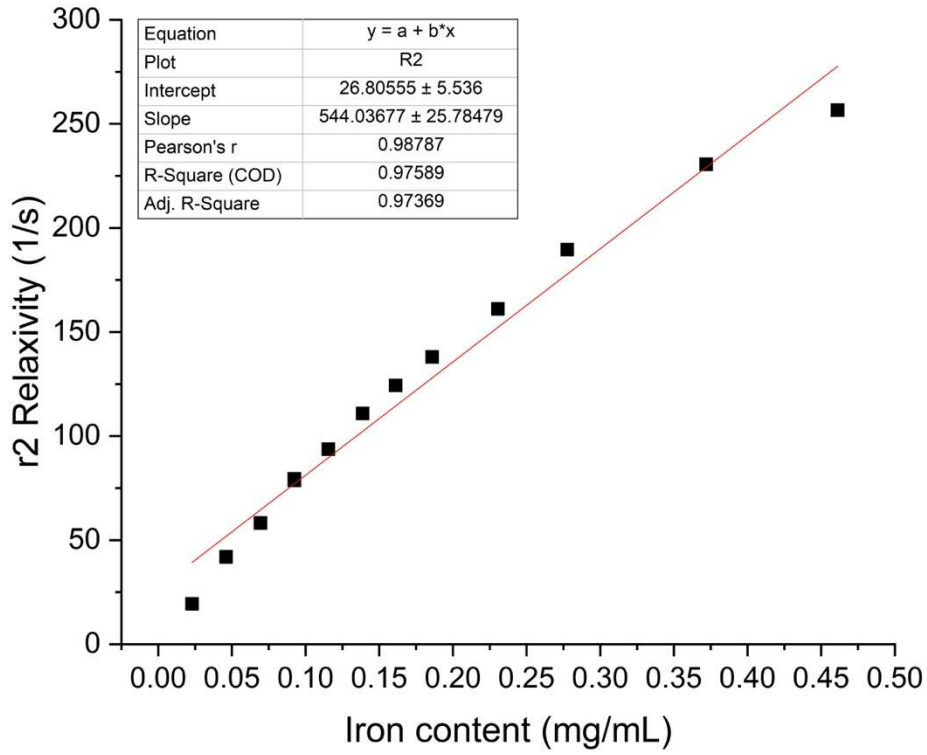

Figure 3.10: r2 values of SPION-PAA as a function of iron content

We obtain our r1 and r2 values as 700 $mM^{-1}s^{-1}$ and 9750 $mM^{-1}s^{-1}$. The calculated r2/r1 ratio is 13.92.

3.3.3 T1 and T2 contrast in ex vivo mouse tissue

In the animal experiment, SPION-PAA concentrations and injection dose were known, but the dispersion of the solution in the muscle tissue was a random process. The remaining concentration of nanoparticles in the tissue is not in our direct control. Hence, our control over the achieved contrast type was limited. Change in T1 and T2 contrast between different concentrations is not the direct result of concentration of the injected solution but the concentration created in the tissue.

MR images of *ex vivo* mice with SPION-PAA administration are provided in Figures 3.11, 3.12, and 3.13. Unmarked images are pre-scans for comparison, and iron concentrations of the injections are given in colored arrows. Since T1 contrast is harder to achieve, experiments were done to create T1 contrast. In Figure 3.11, T1 and T2

contrast is shown in MR images taken with RARE and FLASH sequences. As observed, T1 contrast is achieved in the left injection site, while T2 contrast is observed on the right injection site.

As shown in Figure 3.12, T1 contrast is achieved with both concentrations in the image taken with the FLASH sequence. T1 contrast is achieved in both injection sites.

In Figure 3.13, both T1 and T2 contrast is achieved in the right injection site, and only T1 contrast in the left injection site.

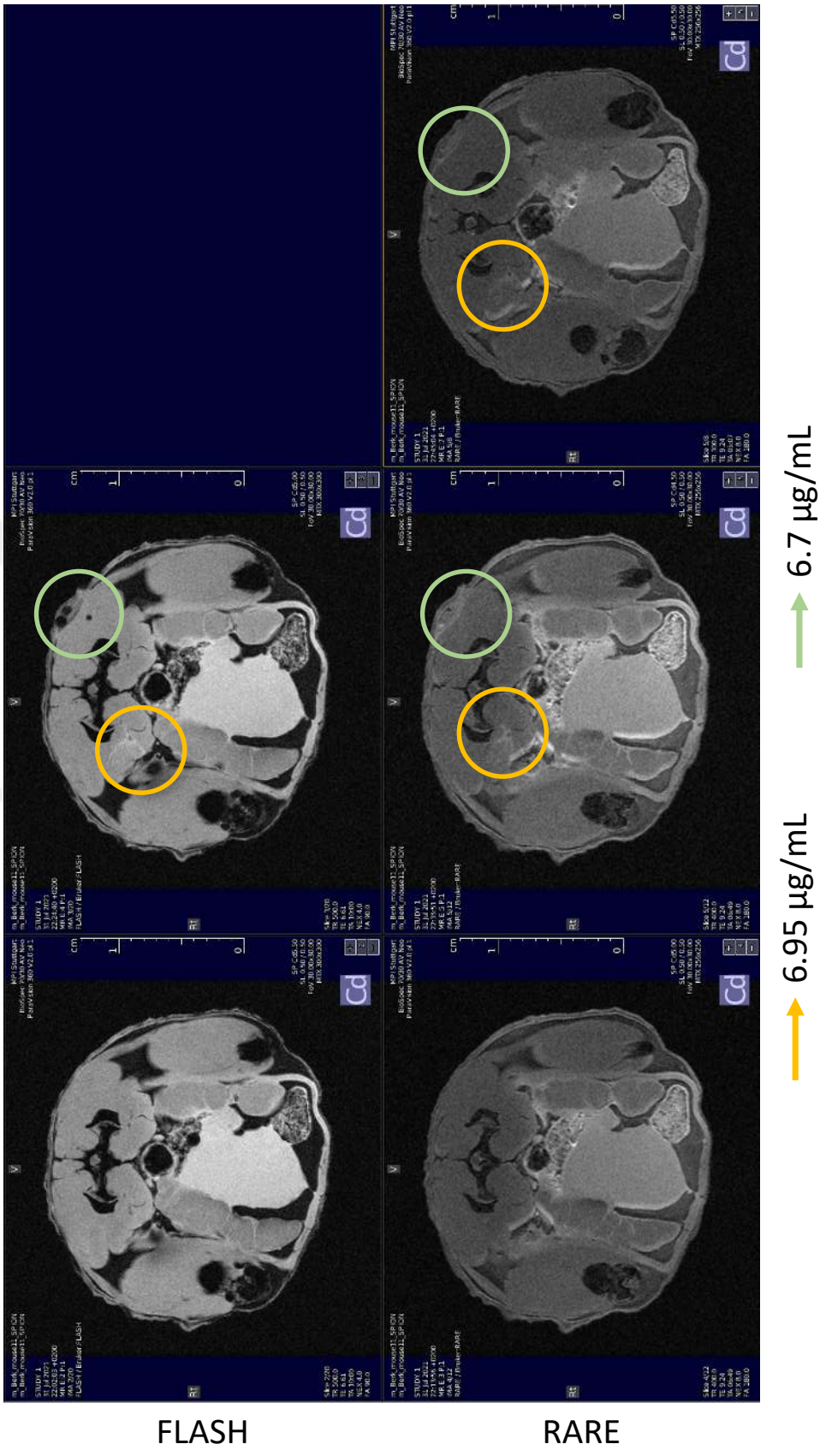

Figure 3.11: Ex vivo mice experiment figure I. T1(bright) and T2(dark) contrasts were achieved in different regions.

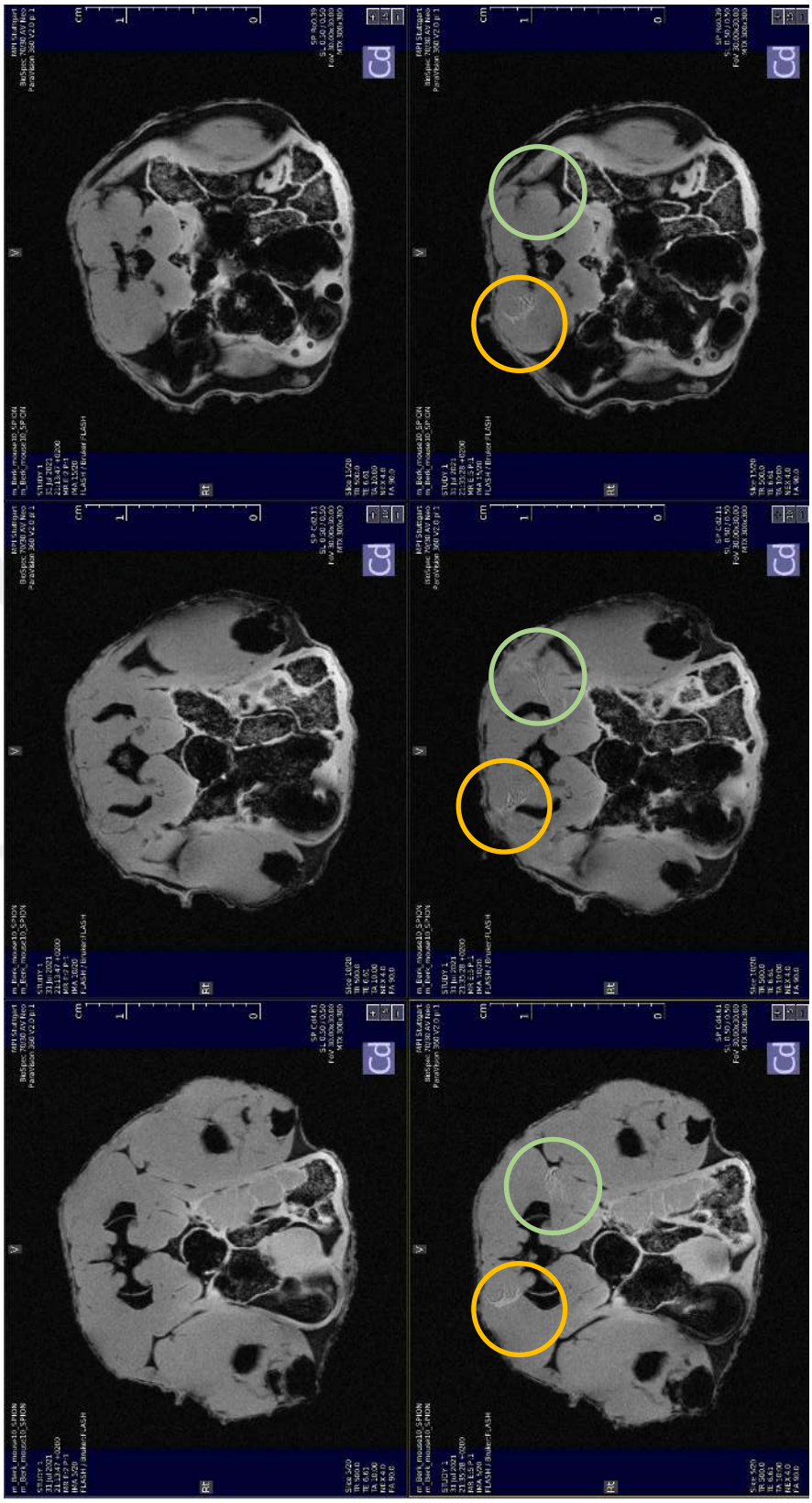

Figure 3.12: Ex vivo mice experiment figure II. T1 was achieved in both injection sites.

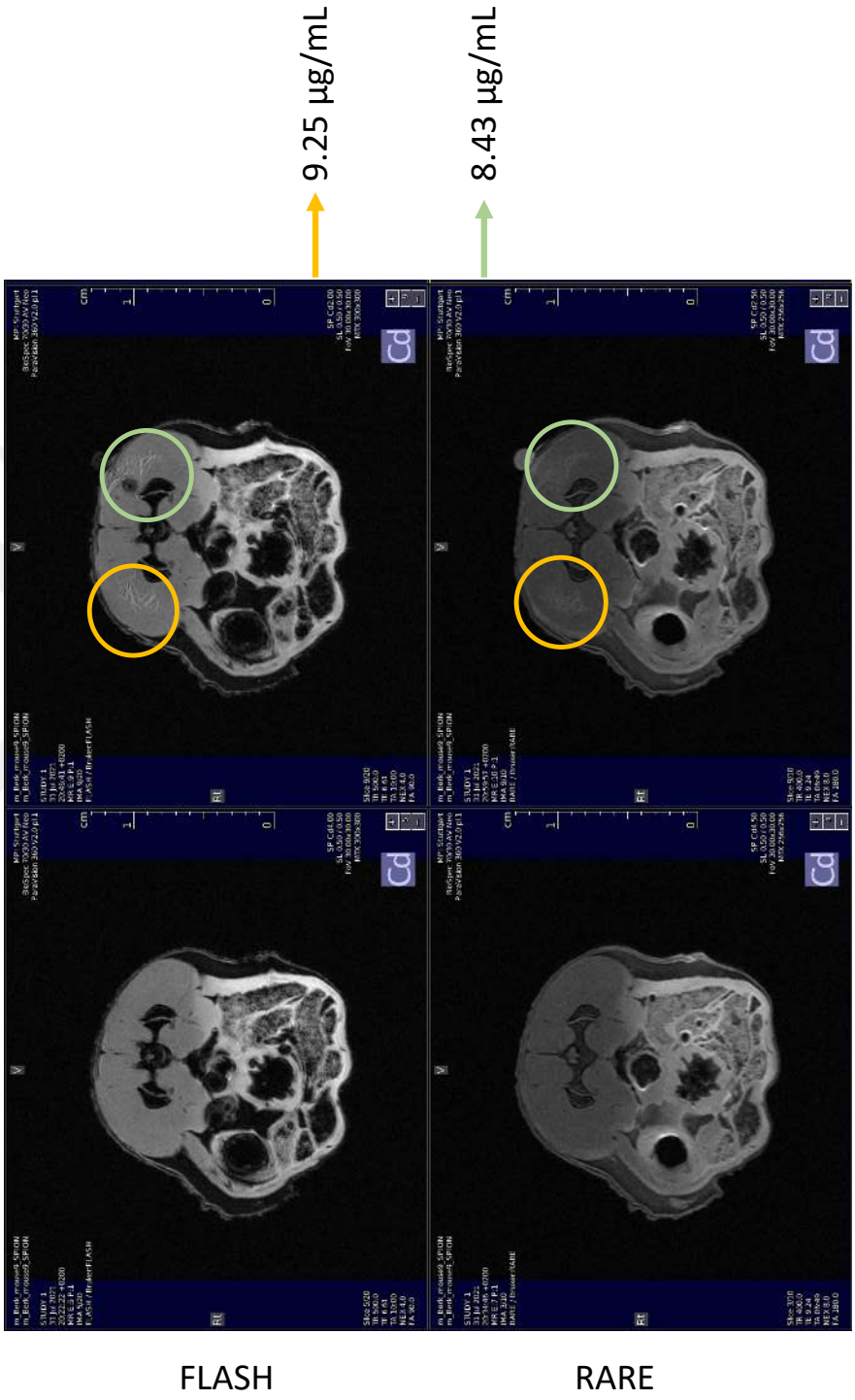

Figure 3.13: Ex vivo mice experiment figure III. T1 contrast was achieved in both injection sites and T2 was visible in the right injection site.

Note the contrast difference in two injections of the same concentration in Figures 3.12 and 3.13. There is a change of contrast between T1 and T2 in the same

concentration. This contrast transition verifies our assumption that the contrast can be affected by the tissue porosity.

3.4 Discussions

In this work, we showed that SPION-PAA could be employed as a dual-mode contrast agent that is able to generate both T1 and T2 contrast depending on the concentration. r1 and r2 values of different concentrations are calculated from the MR images. Only one recent study in the literature, Wang et al., has demonstrated dual-mode contrast with iron oxide nanoparticles with r1=1.37 mM^{-1} s^{-1} and r2=7.53 mM^{-1} s^{-1}, which means r2/r1 ratio of about 5.5 [129]. Although the r2/r1 ratio of SPION-PAA is a higher, the r1 value is significantly higher than the Wang's, as well. *Ex vivo* mice experiment showed that this contrast could be achieved in tissue as well.

The dual-mode feature enables sophisticated measurements like tumor detection due to accumulation using the enhanced permeability and retention (EPR) effect in highly vascularized tissues. Furthermore, using SPIONs as a contrast agent is advantageous for simplifying the system, as multifunctional SPIONs can be used in more than one task and help reduce the number of elements in the design. Numerous applications of SPIONs have been shown in the literature, from hyperthermia to robotic applications. Features of SPION, such as high magnetic saturation, high colloidal stability, and biocompatibility, make SPIONs an excellent choice for any design in the biomedical engineering field. New projects can benefit from multifunctional SPION particles and the existing literature on their biological applications.

Future work should be focused on *in vivo* imaging with the SPION-PAA. MRI imaging of SPION-PAA *in vivo* is required to verify T1 and T2 contrast generation.

Chapter 4:
EXPLOITATION OF POLYACRYLIC ACID COATED SPIONS AS PHOTOINITIATORS

4.1 Background

4.1.1 Photopolymerization

Polymers are defined as macromolecules that are composed of smaller molecules called monomers [149]. The name comes from Greek, meaning many ("poly") parts ("meros"). The reactions in which monomers come together and form a larger polymer molecule are called polymerization reactions. The type of a polymerization reaction is determined by the formation of the polymer chain in the reaction. Although there are several types of the polymerization reaction, the most important two are chain polymerization and step polymerization. In a chain polymerization reaction, monomers are added to the growing end of the polymer chain one by one, similar to an actual chain making process, by adding one ring after another [149]. However, in a step polymerization reaction, monomers bind to each other to form dimers for the second step of the reaction. Dimers merge to tetramers, tetramers to octamers, and so on. The reaction follows similar steps until the end product is reached [149].

The process condition of the polymerization is another important classifier. If the reaction mixture is homogeneous, polymerization is called homogeneous polymerization. Examples of homogeneous polymerization are bulk polymerization and solution polymerization. Heterogeneous polymerization methods include suspension and emulsion polymerizations [149].

Most vinyl monomers polymerize via chain growth mechanism. Such polymerization reactions are usually started with so called *initiators*. Initiators are usually more susceptible to external stimuli such as heat and light; hence they can be used to start polymerization with some external triggering. On the other hand, some substances can be used to enhance the efficiency of the reaction. These substances are named catalysts.

The duty of the initiator is indeed to create the first reactive species which will react with the first monomer molecule producing a reactive chain end (Figure 4.1). Free radical polymerization constitutes the majority of commodity polymers. In that case, initiators produce a free radical that will add to the double bond of the vinyl monomer producing a monomer radical, that will add on the double bond of the second monomer, producing again a free radical chain end which is called as the propagation step. This continues until radical die to several reactions (Figure 4.1). Most free radical polymerizations use initiators that decompose and form reactive free radical species at specific temperature. However, when temperature increase is not desired or practical, such as polymeric coatings on large pieces on living tissue etc., photoactive initiators come into the seen. *Photoinitiators* (PI) generate free radicals upon the excitation at specific wavelength, usually in UV. Such reactions are called photopolymerizations. They are widely used in the coating industry. However, one limitation is the excitation wavelength. Most PIs are active in ultraviolet range, which limits light penetration and pause operational risks. There is a tremendous effort in the industry to develop PIs active in the visible region.

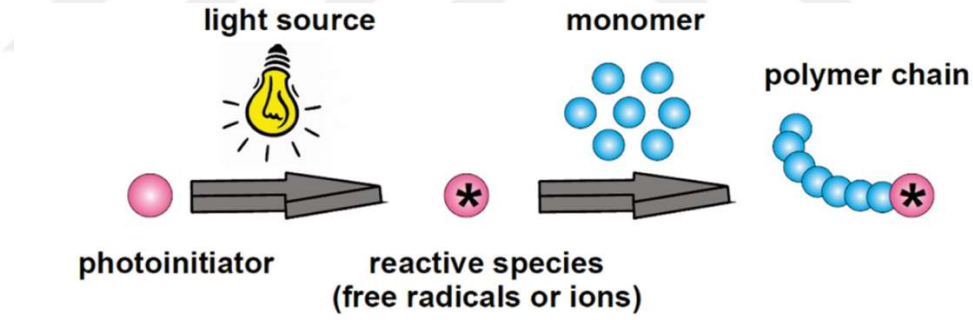

Figure 4.1: Steps of the Photopolymerization. Ultraviolet light creates the free radical by exciting the photoinitiator. Then, monomers bind this free radical to create the polymer chain. [150]

4.1.2 SPION Nanocomposites

Polymer/SPION mixed compositions as nanocomposites or core/shell structures are extremely popular and valuable in niche applications such as magnetically addressable microrobots [151]–[154], drug delivery patches, etc.

Lauric acid coated SPIONs (SPION-LA) have been demonstrated as visible range PIs in the photopolymerization of acrylic by Yagci Acar et al [142]. This is inspiring considering that such an approach eliminated the use of an additional initiator and hence

undesired degradation products, increasing the safety and simplicity and reducing the cost. In addition, since SPIONs have strong absorption in the visible region, they have a great potential to act as a long-wavelength photoinitiator. However, SPION-LA was hydrophobic and allowed photopolymerization of hydrophobic monomers in organic solvents, which is not suitable for aqueous systems desired for medical applications.

4.1.3 Synthesis of Polymer/SPION composites with SPION-PAA based photopolymers and their hyperthermia potential

SPIONs are widely investigated for local hyperthermia [32], [147], drug delivery [37], and thermal actuation [33]. In the literature, magnetic hyperthermia was conducted using alternating magnetic fields (AMF). In AMF, magnetic fields are used to alternate the magnetization of the particle to induce loss mechanisms, like Néel and Brownian relaxations. During these relaxations, particles heat up, and the temperature of the medium containing SPIONs increases [148]. Magnetic hyperthermia may be used for triggered drug release or thermal ablation of tumor cells [148], [155], [156].

Recently, SPIONs were reported as a photosensitizer that converts light to heat efficiently for laser-induced local hyperthermia, called photothermal therapy (PTT). In PTT the irradiation wavelength is critical, and red or NIR wavelengths are preferred for safety and appreciable penetration depths [157]. PAA-SPIONs were also reported by Yagci Acar et al as effective PTT agents at 808 nm, which is one of the most favored wavelengths in medical treatments [31].

In this chapter of the thesis, the use of SPION-PAA dispersed in water as a PI in photopolymerizations of water soluble, a medically relevant monomer, PEGDA was explored. This study involved photoDSC studies in determining the effective wavelength for photoinitiation, reaction kinetics and solution polymerizations to produce PEGDA gels. Lastly, the hyperthermia potential of these gels was evaluated under the alternating magnetic field for magnetic hyperthermia and under 808 nm laser irradiation for photothermal heating.

In this chapter of the thesis, photopolymerization initiated with SPION-PAA is investigated. The verification of the radical source and the polymerization performance in different conditions are provided. The heating of the polymerized samples is

investigated for their hyperthermia potential. High-resolution TEM images of the polymerized samples and Electron Energy Loss Spectroscopy images are presented. Demonstrating the photopolymerization function of SPION-PAA extends SPION-PAAs abilities and makes the particle an excellent candidate for biomedical research.

4.2 Methods and Materials

4.2.1 Bulk Photopolymerizations

Aqueous solutions of SPION-PAA were added to PEGDA (molecular weight of 525 Da, Sigma-Aldrich, MO, USA) in10 and 20 weight% and irradiated at 360 nm in a chamber consisting of 8 ultraviolet lamps (Philips, The Netherlands) for 5 hours.

4.2.2 Decarboxylation Experiment

A test tube containing aqueous SPION-PAA was connected using a silicone the to another test tube containing 4.7 mM NaOH solution with phenolphthalein pH indicator, then placed into the above-mentioned UV chamber. The sample was irradiated with UV for 24 hours. Color change in the tube with pH indicator was monitored.

4.2.3 PhotoDSC Experiments

Polymerization kinetics was studied using a Photo Differential Scanning Calorimeter (PhotoDSC). PhotoDSC experiments were carried out using Q200 DSC (TA Instruments, New Castle, DE, USA). 15 microliters of polymerization mixtures were placed on the sample stand in T-zero DSC pans. SPION-PAA was placed in the reference pans at the same amount used in the polymerization mixtures to compensate for the photoheating effects of SPION-PAA itself. All polymerizations were performed after 10 minutes of N_2 gas purge at 30 °C. UV Arc Lamp (Lumen Dynamics OmniCure S2000 UV source) was used as the light source. Two different excitation filters were used: A broadband filter with high transmission in 320-480 nm range and a visible region filter with high transmission in the 400-500 nm range. Heat flow as a function of time was determined.

Given the heat flow from the sample, the rate of polymerization is calculated as follows,

$$Rate\ of\ Polymerization = \frac{Heat\ Flow}{Bond\ Energy * Number\ of\ Bonds * Moles\ of\ Monomer}.$$

Equation 2: The calculation of the rate of polymerization from the heat flow

The total conversion of monomer to polymer was calculated by integrating the rate in time.

Influence of monomer/SPION-PAA ratio, presence of a co-initiator (triethylamine), excitation filter, and excitation power on conversion and polymerization rate was studied. Polyethylene glycol diacrylate (PEGDA) with a molecular weight of 525 Da was selected as the monomer for PhotoDSC experiments.

4.2.4 Magnetic Heating of Samples

PEGDA/SPION mixtures with 10 and 20 weight% SPION were prepared and were filled into 1 mL polypropylene syringes, then cured at 360 nm. Then, syringes were cut to obtain cylindrically shaped polymers. Polymers were placed in 2 mL Eppendorf tubes, placed at the center of a coil and exposed to an alternating magnetic field with 347 kHz frequency and power of 7.5 kW for 15 minutes(EasyHeat, Ambrell, NY, USA). The temperature of the gels was recorded with an optical temperature probe (FOTEMP OEM-PLUS, Optocon, Germany) that was inserted at the center of the gels, as shown in Figure 4.2.

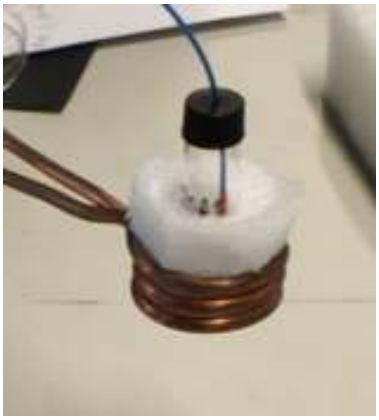

Figure 4.2: Magnetic heating setup of gels. The sample was placed in a vial with an optical temperature probe. The vial was put at the center of heater coil.

4.2.5 TEM imaging of polymerized gels

TEM imaging of the polymerized gels was done in Stuttgart Center for Electron Microscopy. Polymerized samples were frozen, cut with the microtome device, and placed on a copper grid. Imaging was done with two devices: for general overview 120 kV TEM (912 Omega, Zeiss, Germany), and for HRTEM and STEM images, 200 kV TEM (ARM 200CF, JEOL, Japan) were used.

4.3 Results

4.3.1 Initial Bulk Polymerization

Initial studies conducted under UV irradiation produced fully polymerized PEGDA into a kind of gel, confirming the effective photoinitiation with SPION-PAA (Figure 4.3). Next, the possible mechanism for SPION-PAA based photoinitiation was investigated.

Figure 4.3: Polymerized samples of bulk polymerization. Samples were fully polymerized.

Our previous studies with SPION-lauric acid concluded that photo-Kolbe reaction is responsible for the initial radical generation [142]. Irradiation of the SPION with carboxylic acid groups adsorbed on its surfaces with high-energy photons create an electron-hole pair in the nanoparticle. Interaction of the hole with the carboxylic acid produces a carboxylate radical which rearranges to kick off CO_2 and produce a carbon radical as the first initiating radical for the polymerization, as suggested in Figure 4.4 [142], [158].

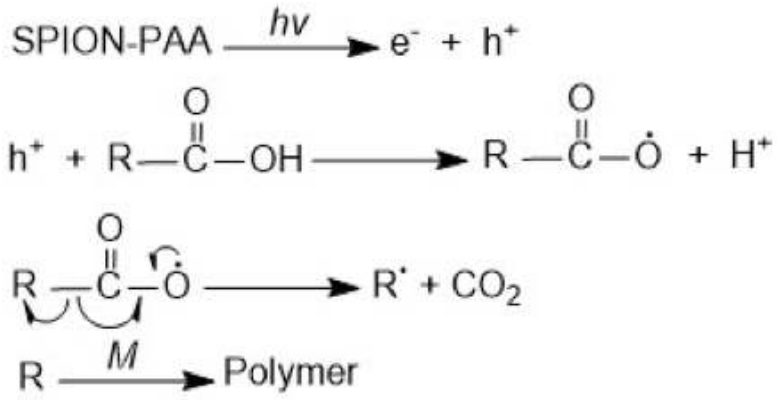

Figure 4.4: Suggested mechanism of initiation. The hole created by the UV irradiation initiates photo-Fries rearrangement, a radical is generated, and a CO2 molecule is released.

Hence, a decarboxylation experiment was performed with SPION-PAA as well to determine if Photo-Kolbe reaction is also responsible from initiation. In the set-up shown in Figure 4.4, if CO_2 would release upon photoexcitation of the SPION-PAA, it would travel to the tube with NaOH and reduce the pH which would be detected by the discoloration of the pink solution which had a pH indicator.

After 12 hours of UV irradiation, the pinkish color of the solution has gotten lighter in hue, as shown in Figure 4.5. Hence, this experiment suggests that ultraviolet light irradiation of SPION-PAA is the source of CO2, which is possible due to the Photo-Kolbe reaction.

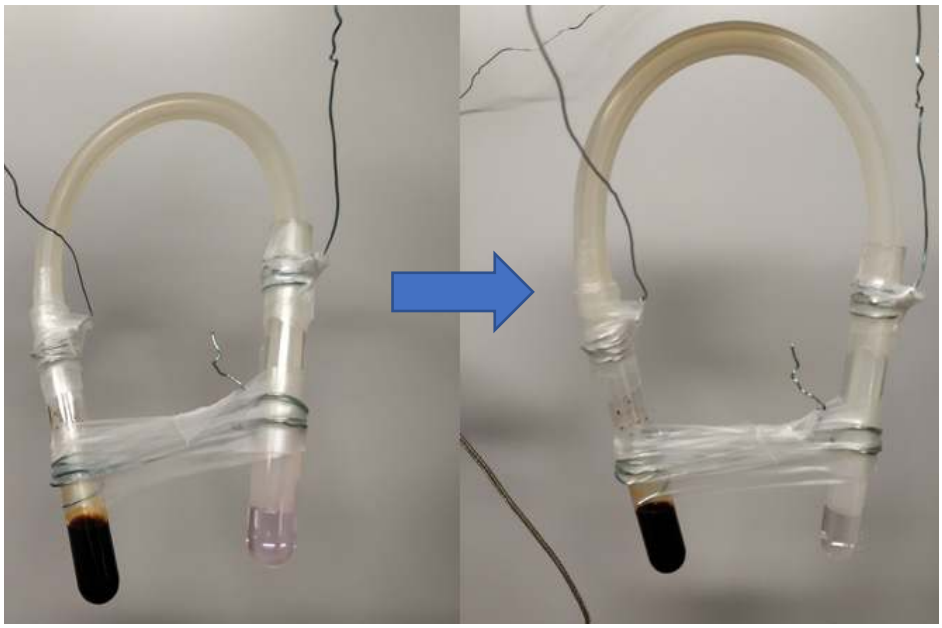

Figure 4.5: Decarboxylation experiment of SPION-PAA. The pinkish color of the basic solution has disappeared after 24 hours of ultraviolet light irradiation.

4.3.2 Photopolymerization kinetics

Rate of polymerization and monomer conversion was first determined using PEGDA and 10-20-40 weight% SPION-PAA with 40mW incident power in 320-480 nm wavelength range. We have found that the rate of polymerization and conversion increases until 20 weight% and decreases after that (Figure 4.6) which may be due to scattering events at high SPION loading.

In Figure 4.7, the influence of incident power on polymerization for 10 weight% SPION-PAA / PEGDA mixture in 320-480 nm wavelength range was summarized. As expected, increasing the incident power to 40mW increased the rate and the conversion significantly.

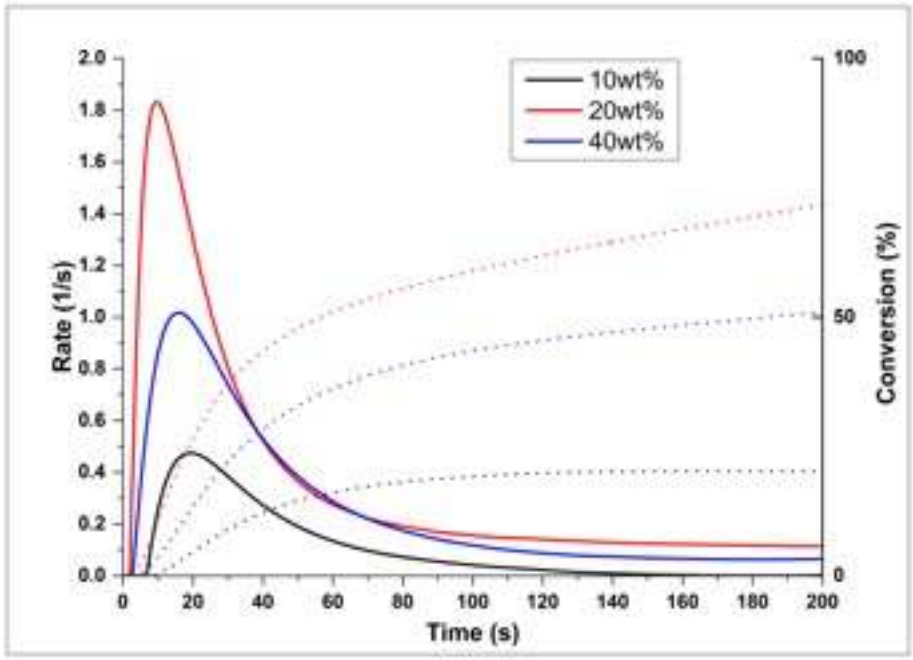

Figure 4.6: The rate of polymerization and conversion with different SPION-PAA feed ratios.

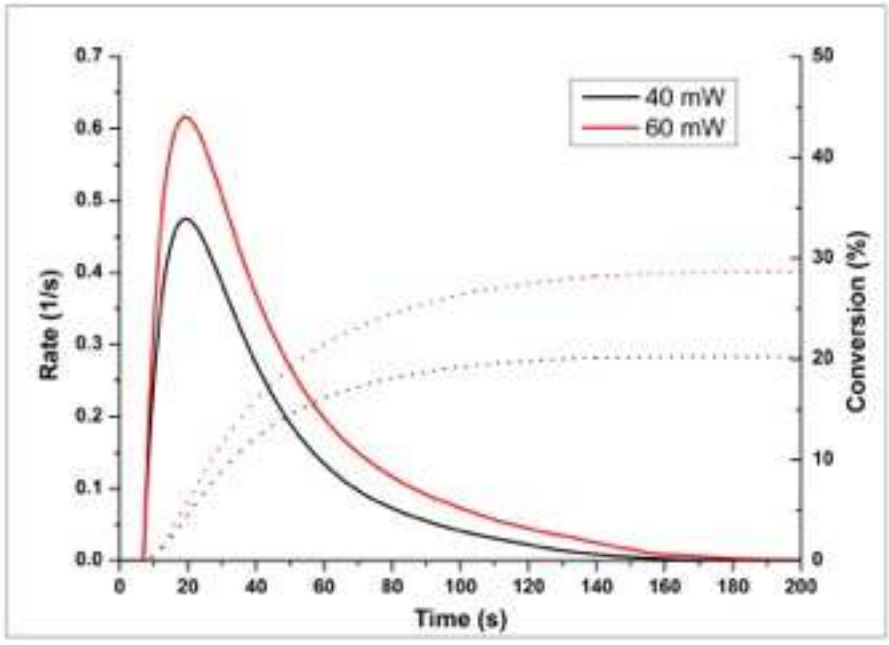

Figure 4.7: The rate of polymerization and conversion with different incident light powers. A higher power induced a higher polymerization rate.

One of the goals of using SPIONs as a photoinitiator is to explore its potential as long-wavelength photoinitiator. In order to evaluate the effect of the excitation wavelength, visible (400-500 nm) and broadband (320-480 nm) filters were used during excitation. A comparison of different excitation wavelength ranges using 20 weight% SPION-PAA and 40 mW power is given in Figure 4.8. Indeed, excitation between 400-500 nm caused photopolymerization of PEGDA with about 40% monomer conversion after a brief inhibition period. Broadband excitation, which included UV, caused a faster reaction with about 70% monomer conversion. Broad excitation filter provides more energetic photons as SPION absorption in the 320-480 nm is higher than 400-500 nm. On the other hand, one great advantage of using a visible excitation filter is the suppression of PEGDA autopolymerization in addition to safety of the light source and better penetration depth.

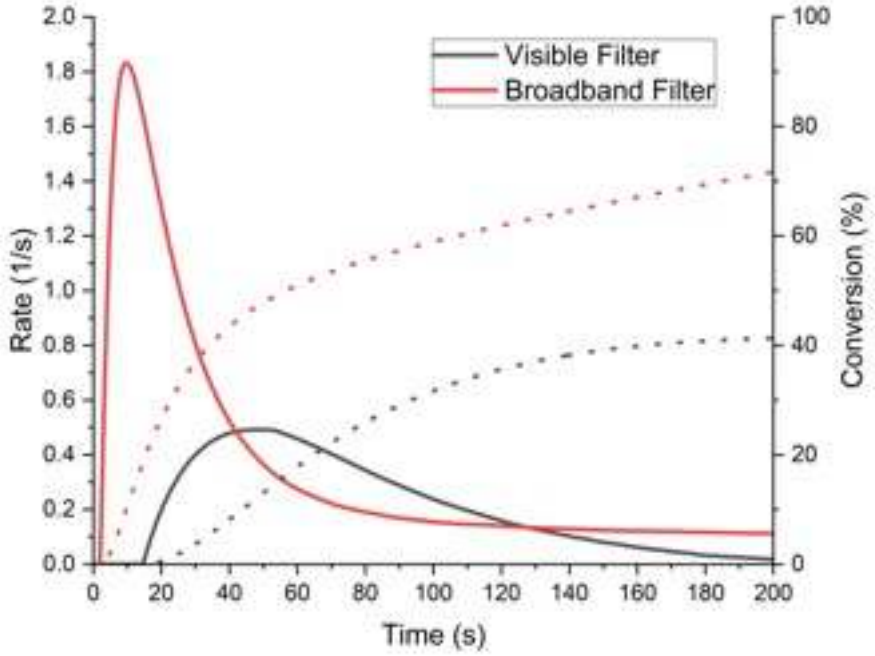

Figure 4.8: The rate of polymerization and conversion with different wavelength ranges.

Triethylamine (TEA), is added to the polymerization mixture to determine whether the co-initiator boosts the polymerization rate. However, it is observed that the addition of co-initiator quenched generated radicals and decreased the rate of polymerization, as seen in Figure 4.9.

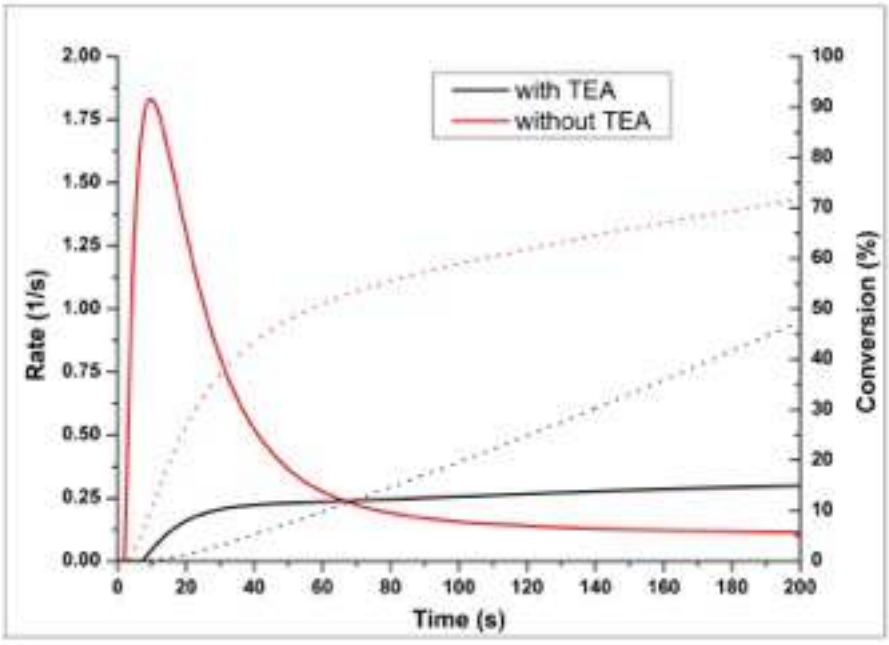

Figure 4.9: The rate of polymerization and conversion with and without Triethylamine (TEA). The addition of co-initiator decreased the rate of polymerization.

Therefore, the optimal recipe was determined as 20 weight% SPION-PAA as an initiator, use of broad-band filter and 60 mW incident light power. Besides, SPION-PAA was also confirmed as a long-wavelength photoinitiator.

4.3.3 TEM images of polymerized gels

In Figure 4.10 and Figure 4.11, the general overview of polymerized sample is provided. SPION seems to be homogeneously distributed within the polymer. Electron energy loss spectroscopy analysis was performed on the samples. The original signal and the derived background-subtracted signal are given in Figure 4.12. The SPION inside the polymer is verified with Figure 4.13, as the Fe_3O_4 signal from the EELS Atlas [159], [160] is matched as shown.

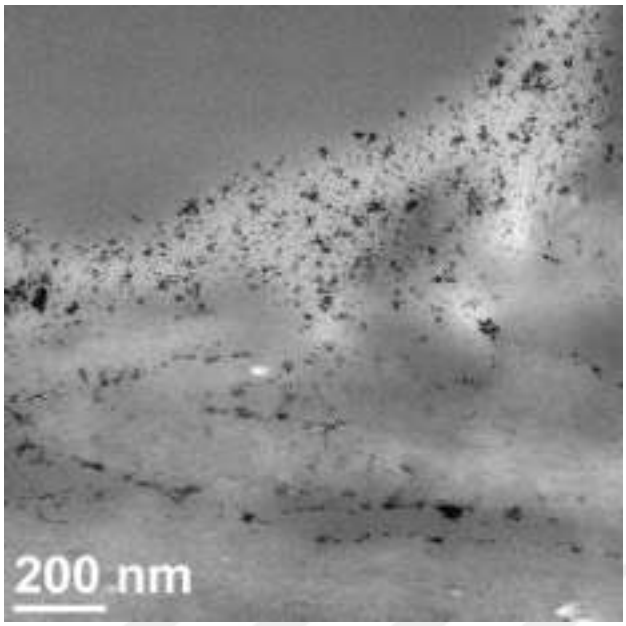

Figure 4.10: TEM of the polymer, general overview I. Particles appeared to be homogenously distributed.

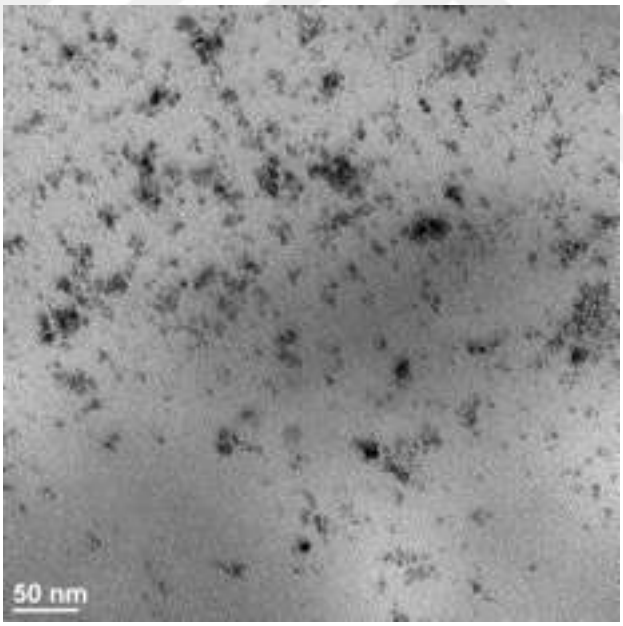

Figure 4.11: TEM of the polymer, general overview II. Particles appeared to be homogenously distributed.

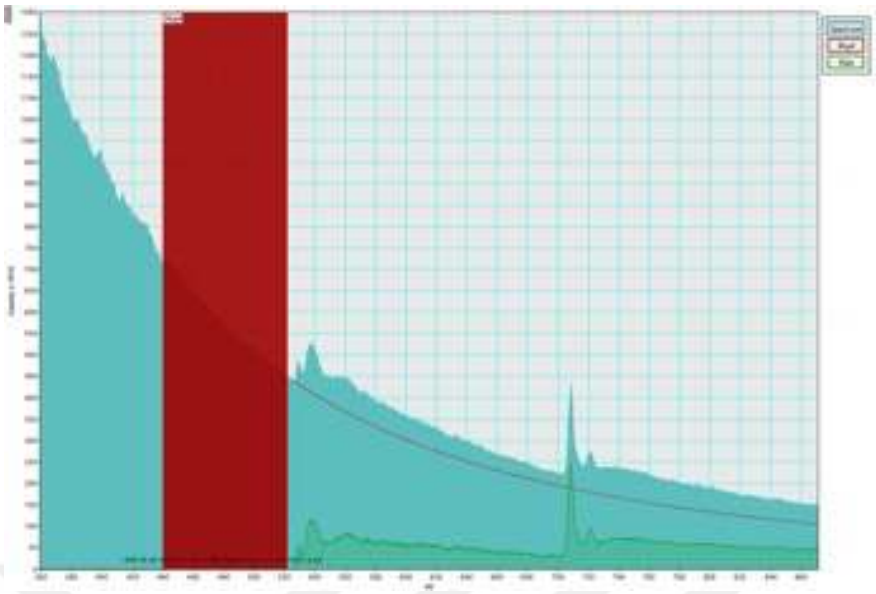

Figure 4.12: EELS of the sample. The background, obtained from the red shaded area, is subtracted from the original signal.

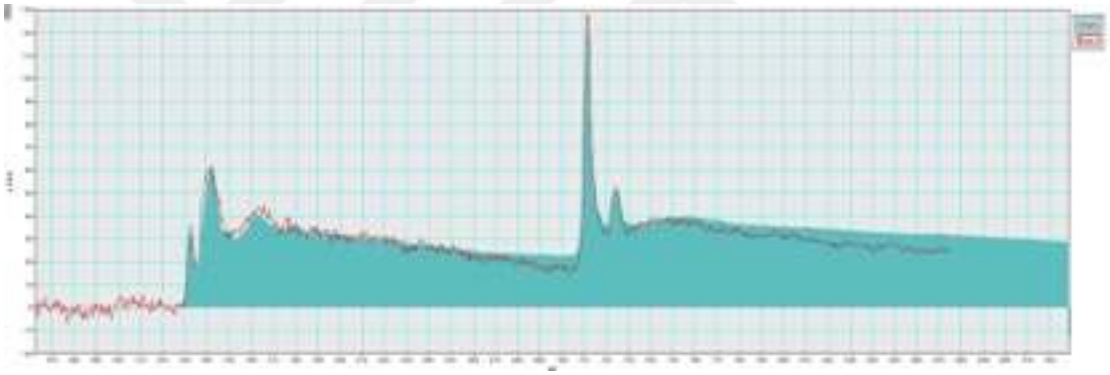

Figure 4.13: The background subtracted EELS signal(red) and the Fe_3O_4 signal(green) form the EELS Atlas. A good match verifies the SPION inside gel matrix.

In Figure 4.14, elemental signals are provided. As observed from the figure, while the iron signal is restricted to the SPION positions, the oxygen signal is present throughout the entire image since oxygen is present in both the SPION and the polymer itself.

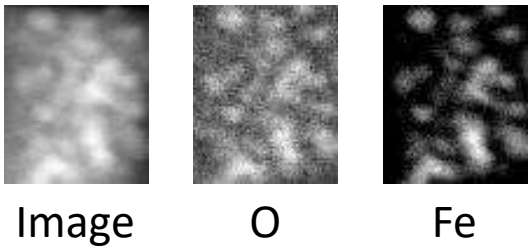

Figure 4.14: Elemental Imaging: Image position, the oxygen signal and the iron signal. Oxygen is present both in gel and SPION-PAA, while iron is only present in SPION-PAA.

High-resolution transmission electron microscopy is done to verify the SPION-PAA crystalline structure. The zoomed image given in Figure 4.15 is used to determine the distance between molecules inside the SPION crystal. Sometimes referred to as the d-spacing, the crystal's interplanar molecular distance helps identify the crystal type. 1D projection of the pixels in the red rectangle in the Figure 4.15 is shown in Figure 4.16. The figure shows that the mean distance is ~0.2 nm, consistent with the magnetite literature [161].

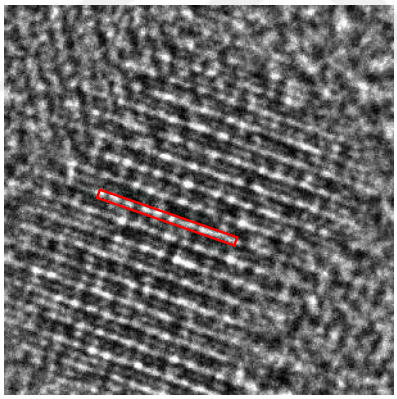

Figure 4.15: A high resolution TEM image of the SPION-PAA in polymer. 1D projection of the red rectangle is used to measure crystalline spacing in Figure 4.17.

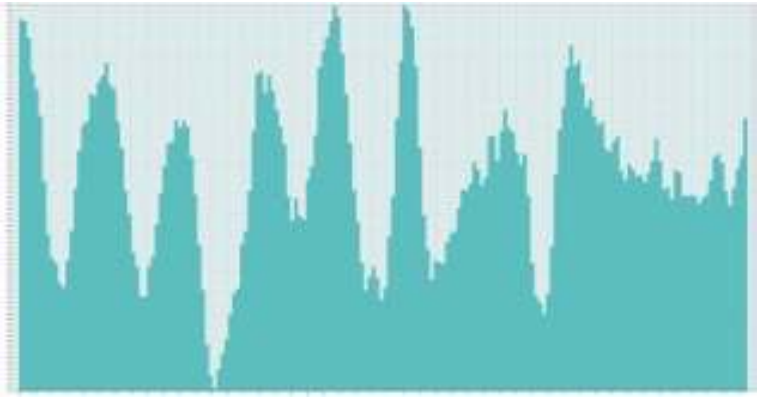

Figure 4.16: 1D projection of the red rectangle area in Figure 4.16. Distance between the first and eighth peak is 1.75 nm.

4.3.4 Heating under alternating magnetic field

One of the advantages of using small sized and highly dispersed SPIONs is the ability to load high concentrations of SPIONs into a polymeric matrix, especially for magnetic hyperthermia or magnetic dragging applications. Figure 4.10 presents the temperature change of the PEGDA/SPION gels under the alternating magnetic field. Since the gels contained high loading of SPION-PAA, they were quickly heated to high temperatures, proving their potential to be used in hyperthermia applications.

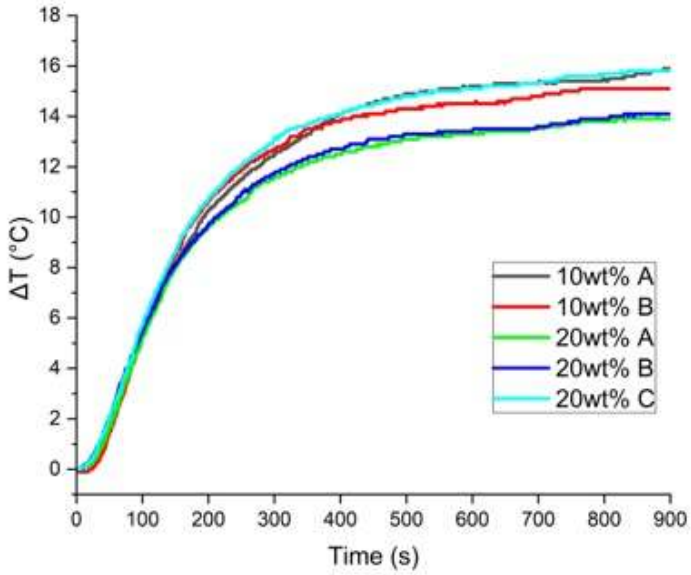

Figure 4.17: Magnetic heating of the polymers

4.4 Discussion

SPION-PAA nanoparticles which were confirmed as dual contrast agents in MRI in chapter 3, was confirmed as successful photoinitiators in this chapter, forming nanocomposites with well-dispersed SPIONs. The influence of several parameters on the photopolymerization was investigated, and the optimal parameters were determined. Although photopolymerization was fastest and the conversion is highest at broad band excitation including UV range, SION-PAA was also confirmed effective long-wavelength photoinitiator.

In this chapter, the magnetic hyperthermia potential of SPION loaded polymers were also confirmed under alternating magnetic field, which shows the diverse function of the SPION-PAA.

One of the main benefits of SPION-PAA is the high-loading of the particle in the polymers. Due to their high stability in solution, SPION-PAA remains colloidal and has a long shelf life. High nanoparticle loading to the polymer is possible with these nanoparticles. This is advantageous because the total magnetization increases with higher loading, causing higher temperature increases with alternating magnetic fields, and more force/torque for actuation with the same magnetic field is possible. Furthermore, the use of SPION-PAA enables the simplification of the system by reducing the number of elements. The use of SPION-PAA/polymer nanocomposite in biomedical robotics is advantageous for the same reason. Same SPION particles dispersed in the polymer can be used for polymerization, actuation, drug delivery, heating, and tracking, as established in Chapter 3. The biocompatible nature of SPION-PAA makes the end product ideal for biomedical applications.

Future work on the photopolymerization of SPION-PAA should focus on the printing abilities. Stereolithography printing of SPION-PAA should be investigated to achieve microrobots that consist of multifunctional SPION-PAA and polymer only.

Chapter 5:
CONCLUSION

This thesis shows that new sensing, tracking, and imaging methods are feasible and practical in MRI. In chapter 2, a new mechanism for sensing and tracking in MRI is proposed. The proposed sensor depends on the parasitic capacitance for its resonant frequency. Hence, a change in the relative permittivity directly affects capacitance, consequently, the resonant frequency. The temperature dependence of the relative permittivity makes the resonant frequency sensitive to the temperature, the coupling between the MRI and the sensor changes with the ambient temperature. This relation is visible in the MR image signal and also quantifiable. The in-situ temperature can be measured with the proposed mechanism via the MR images without an extra image sequence. We have demonstrated the ex vivo feasibility in a porcine heart with a root mean square error of 0.6°C.

In this thesis, ex vivo demonstration of the idea was done; but the future work for the sensor should be concentrated on in vivo applications since the conditions of the live environment might be challenging for the sensor. Harsh conditions like the stomach or intestines should be tested for the sensor operation. Another essential aspect that needs further investigation is the in-motion measurement. Sensor signals might be affected by the motion; thus, methods like sparse reconstruction can compensate for the artefact created by the motion in MRI.

In chapter 3, polyacrylic acid-coated SPION is demonstrated as a dual-mode MRI contrast agent. Solution and ex vivo mouse tests showed that these SPIONs provide not only a strong T2 but also a strong bright (T1) contrast. Future studies for the polyacrylic acid-coated SPION should focus on the in vivo MR imaging.

In the last chapter, performance of the polyacrylic acid-coated SPION as a free radical photoinitiator and formation of nanocomposites were demonstrated. Radical initiation with the SPION-PAA under UV and the visible range was shown to produce nanocomposites with high and well dispersed SPIONs. Further work on the subject should be towards the applications. Printing with 3D polymerization methods like stereolithography using SPION-PAA particles can be one direction for future work.

Demonstration of the printed designs, including microrobot design, should show the abilities of the SPION-PAA in the biomedical field. SPION filled PEGDA gels were also confirmed as effective heat generators under the alternating magnetic field to generate local temperature increases. This may be exploited in the future for hyperthermia and drug release.

Overall, SPION-PAA was shown as a multifunctional nanoparticle that may be exploited to design polymeric materials/devices with dual contrast in MRI for tracking and magnetic hyperthermia for therapy or triggered drug release.

BIBLIOGRAPHY

[1] M. Vierra, “Minimally invasive surgery,” *Annu. Rev. Med.*, vol. 46, pp. 147–158, 1995, doi: 10.1146/annurev.med.46.1.147.

[2] P. R. Mueller *et al.*, “MR-guided aspiration biopsy: Needle design and clinical trials,” *Radiology*, vol. 161, no. 3, pp. 605–609, 1986, doi: 10.1148/radiology.161.3.3786706.

[3] R. Lufkin, L. Teresi, and W. Hanafee, “New Needle for MR-Guided Aspiration Cytology of the Head and Neck,” no. August, pp. 380–382, 1987.

[4] N. Gudino, J. A. Heilman, J. J. Derakhshan, J. L. Sunshine, J. L. Duerk, and M. A. Griswold, “Control of intravascular catheters using an array of active steering coils,” *Med. Phys.*, vol. 38, no. 7, pp. 4215–4224, 2011, doi: 10.1118/1.3600693.

[5] J. A. Bell *et al.*, “A deflectable guiding catheter for real-time MRI-guided interventions,” *J. Magn. Reson. Imaging*, vol. 35, no. 4, pp. 908–915, 2012, doi: 10.1002/jmri.23520.

[6] Z. He *et al.*, “Design of a percutaneous MRI-guided needle robot with soft fluid-driven actuator,” *IEEE Robot. Autom. Lett.*, vol. 5, no. 2, pp. 2100–2107, 2020.

[7] H. Su *et al.*, “Piezoelectrically Actuated Robotic System for MRI-Guided Prostate Percutaneous Therapy,” *IEEE/ASME Trans. Mechatronics*, vol. 20, no. 4, pp. 1920–1932, 2015, doi: 10.1109/TMECH.2014.2359413.

[8] O. Felfoul, A. T. Becker, G. Fagogenis, and P. E. Dupont, “Simultaneous steering and imaging of magnetic particles using MRI toward delivery of therapeutics,” *Sci. Rep.*, vol. 6, no. 1, pp. 1–10, 2016.

[9] S. Mutlu, O. Yasa, O. Erin, and M. Sitti, “Magnetic Resonance Imaging-Compatible Optically Powered Miniature Wireless Modular Lorentz Force Actuators,” *Adv. Sci.*, vol. 8, no. 2, pp. 1–14, 2021, doi: 10.1002/advs.202002948.

[10] O. Erin, M. Boyvat, J. Lazovic, M. E. Tiryaki, and M. Sitti, “Wireless MRI-

Powered Reversible Orientation-Locking Capsule Robot," *Adv. Sci.*, p. 2100463, 2021.

[11] P. Magnusson *et al.*, "Passive catheter tracking during interventional MRI using hyperpolarized 13C," *Magn. Reson. Med.*, vol. 57, no. 6, pp. 1140–1147, 2007, doi: 10.1002/mrm.21239.

[12] S. Kozerke, S. Hegde, T. Schaeffter, R. Lamerichs, R. Razavi, and D. L. Hill, "Catheter tracking and visualization using 19F nuclear magnetic resonance," *Magn. Reson. Med.*, vol. 52, no. 3, pp. 693–697, 2004, doi: 10.1002/mrm.20202.

[13] N. Whiting *et al.*, "Real-Time MRI-Guided Catheter Tracking Using Hyperpolarized Silicon Particles," *Sci. Rep.*, vol. 5, pp. 1–8, 2015, doi: 10.1038/srep12842.

[14] J. Anders, P. Sangiorgio, X. Deligianni, F. Santini, K. Scheffler, and G. Boero, "Integrated active tracking detector for MRI-guided interventions," *Magn. Reson. Med.*, vol. 67, no. 1, pp. 290–296, 2012, doi: 10.1002/mrm.23112.

[15] K. Zhang, A. J. Krafft, R. Umathum, F. Maier, W. Semmler, and M. Bock, "Real-time MR navigation and localization of an intravascular catheter with ferromagnetic components," *Magn. Reson. Mater. Physics, Biol. Med.*, vol. 23, no. 3, pp. 153–163, 2010.

[16] C. Dahmen, K. Belharet, D. Folio, A. Ferreira, and S. Fatikow, "MRI-based dynamic tracking of an untethered ferromagnetic microcapsule navigating in liquid," *Int. J. Optomechatronics*, vol. 10, no. 2, pp. 73–96, 2016, doi: 10.1080/15599612.2016.1166305.

[17] M. E. Tiryaki, Ö. Erin, and M. Sitti, "A Realistic Simulation Environment for MRI-Based Robust Control of Untethered Magnetic Robots With Intra-Operational Imaging," *IEEE Robot. Autom. Lett.*, vol. 5, no. 3, pp. 4501–4508, 2020.

[18] O. Nassar, D. Mager, and J. G. Korvink, "Wireless Double Micro-Resonator for Orientation Free Tracking of MR-Catheter during Interventional MRI," *IEEE J.*

Electromagn. RF Microwaves Med. Biol., vol. 5, no. 1, pp. 78–83, 2021, doi: 10.1109/JERM.2020.3010093.

[19] N. Garnov *et al.*, "Suitability of miniature inductively coupled RF coils as MR-visible markers for clinical purposes," *Med. Phys.*, vol. 38, no. 11, pp. 6327–6335, 2011.

[20] C.-L. Cheung, J. D.-L. Ho, V. Vardhanabhuti, H.-C. Chang, and K.-W. Kwok, "Design and Fabrication of Wireless Multilayer Tracking Marker for Intraoperative MRI-Guided Interventions," *IEEE/ASME Trans. Mechatronics*, vol. 25, no. 2, pp. 1016–1025, 2020.

[21] T. Kahn, T. Harth, J. C. W. Kiwit, H.-J. Schwarzmaier, C. Wald, and U. M"odder, "In vivo MRI thermometry using a phase-sensitive sequence: preliminary experience during MRI-guided laser-induced interstitial thermotherapy of brain tumors," *J. Magn. Reson. Imaging*, vol. 8, no. 1, pp. 160–164, 1998.

[22] J. De Poorter, C. De Wagter, Y. De Deene, C. Thomsen, F. Staahlberg, and E. Achten, "Noninvasive MRI thermometry with the proton resonance frequency (PRF) method: in vivo results in human muscle," *Magn. Reson. Med.*, vol. 33, no. 1, pp. 74–81, 1995.

[23] V. Rieke, "MR thermometry," *Interv. Magn. Reson. Imaging*, pp. 271–288, 2011.

[24] M. Delcey, P. Bour, V. Ozenne, W. Ben Hassen, and B. Quesson, "A fast MR-thermometry method for quantitative assessment of temperature increase near an implanted wire," *PLoS One*, vol. 16, no. 5, p. e0250636, 2021.

[25] A. F. Stalder, M. F. Russe, A. Frydrychowicz, J. Bock, J. Hennig, and M. Markl, "Quantitative 2D and 3D phase contrast MRI: Optimized analysis of blood flow and vessel wall parameters," *Magn. Reson. Med.*, vol. 60, no. 5, pp. 1218–1231, 2008, doi: 10.1002/mrm.21778.

[26] E. M. Haacke *et al.*, "In vivo measurement of blood oxygen saturation using magnetic resonance imaging: A direct validation of the blood oxygen level-

dependent concept in functional brain imaging," *Hum. Brain Mapp.*, vol. 5, no. 5, pp. 341–346, 1997, doi: 10.1002/(SICI)1097-0193(1997)5:5<341::AID-HBM2>3.0.CO;2-3.

[27] R. S. Alomari, J. J. Corso, V. Chaudhary, and G. Dhillon, "Computer-aided diagnosis of lumbar disc pathology from clinical lower spine MRI," *Int. J. Comput. Assist. Radiol. Surg.*, vol. 5, no. 3, pp. 287–293, 2010, doi: 10.1007/s11548-009-0396-9.

[28] P. Natarajan, N. Krishnan, N. S. Kenkre, S. Nancy, and B. P. Singh, "Tumor detection using threshold operation in MRI brain images," *2012 IEEE Int. Conf. Comput. Intell. Comput. Res. ICCIC 2012*, pp. 4–7, 2012, doi: 10.1109/ICCIC.2012.6510299.

[29] K. M. Iftekharuddin, J. Zheng, M. A. Islam, and R. J. Ogg, "Fractal-based brain tumor detection in multimodal MRI," *Appl. Math. Comput.*, vol. 207, no. 1, pp. 23–41, 2009, doi: 10.1016/j.amc.2007.10.063.

[30] A. Hai, V. C. Spanoudaki, B. B. Bartelle, and A. Jasanoff, "Wireless resonant circuits for the minimally invasive sensing of biophysical processes in magnetic resonance imaging," *Nat. Biomed. Eng.*, vol. 3, no. 1, pp. 69–78, 2019.

[31] K. Bilici, A. Muti, F. Demir Duman, A. Sennaroğlu, and H. Yağci Acar, "Investigation of the factors affecting the photothermal therapy potential of small iron oxide nanoparticles over the 730-840 nm spectral region," *Photochem. Photobiol. Sci.*, vol. 17, no. 11, pp. 1787–1793, 2018, doi: 10.1039/c8pp00203g.

[32] M. Erkisa *et al.*, "Etoposide Loaded SPION-PNIPAM Nanoparticles Improve the in vitro Therapeutic Outcome on Metastatic Prostate Cancer Cells via Enhanced Apoptosis," *Chem. Biodivers.*, vol. 17, no. 11, 2020, doi: 10.1002/cbdv.202000607.

[33] X. Huang, Z. Ren, and C. Majidi, "Soft Thermal Actuators with Embedded Liquid Metal Microdroplets for Improved Heat Management," *2020 3rd IEEE Int. Conf. Soft Robot. RoboSoft 2020*, pp. 367–372, 2020, doi: 10.1109/RoboSoft48309.2020.9115972.

[34] M. Suter *et al.*, “Superparamagnetic microrobots: Fabrication by two-photon polymerization and biocompatibility,” *Biomed. Microdevices*, vol. 15, no. 6, pp. 997–1003, 2013, doi: 10.1007/s10544-013-9791-7.

[35] S. Prijic *et al.*, “Surface modified magnetic nanoparticles for immuno-gene therapy of murine mammary adenocarcinoma,” *Biomaterials*, vol. 33, no. 17, pp. 4379–4391, 2012, doi: 10.1016/j.biomaterials.2012.02.061.

[36] O. Unal *et al.*, “Treatment of breast cancer with autophagy inhibitory microRNAs carried by AGO2-conjugated nanoparticles,” *J. Nanobiotechnology*, vol. 18, no. 1, pp. 1–18, 2020, doi: 10.1186/s12951-020-00615-4.

[37] T. Neuberger, B. Schöpf, H. Hofmann, M. Hofmann, and B. Von Rechenberg, “Superparamagnetic nanoparticles for biomedical applications: Possibilities and limitations of a new drug delivery system,” *J. Magn. Magn. Mater.*, vol. 293, no. 1, pp. 483–496, 2005, doi: 10.1016/j.jmmm.2005.01.064.

[38] O. Erin, M. Boyvat, M. E. Tiryaki, M. Phelan, and M. Sitti, “Magnetic Resonance Imaging System--Driven Medical Robotics,” *Adv. Intell. Syst.*, vol. 2, no. 2, p. 1900110, 2020.

[39] M. W. Wilson *et al.*, “Magnetic catheter manipulation in the interventional MR imaging environment,” *J. Vasc. Interv. Radiol.*, vol. 24, no. 6, pp. 885–891, 2013.

[40] J. Dai *et al.*, “A Robotic Platform to Navigate MRI-guided Focused Ultrasound System,” *IEEE Robot. Autom. Lett.*, vol. 6, no. 3, pp. 5137–5144, 2021.

[41] G. Fang *et al.*, “Soft robotic manipulator for intraoperative MRI-guided transoral laser microsurgery,” *Sci. Robot.*, vol. 6, no. 57, 2021.

[42] S. Krueger *et al.*, “An MR guidewire based on micropultruded fiber-reinforced material,” *Magn. Reson. Med.*, vol. 60, no. 5, pp. 1190–1196, 2008, doi: 10.1002/mrm.21743.

[43] S. Kos *et al.*, “First magnetic resonance imaging-guided aortic stenting and cava filter placement using a polyetheretherketone-based magnetic resonance imaging-compatible guidewire in swine: Proof of concept,” *Cardiovasc. Intervent.*

Radiol., vol. 32, no. 3, pp. 514–521, 2009, doi: 10.1007/s00270-008-9483-5.

[44] Y. Wang and K. Harrington, “Dscc2010- Sliding Mode Control of Piezoelectric Valve Regulated Pneumatic Actuator,” *Design*, pp. 1–6, 2010.

[45] W. Shang, H. Su, G. Li, and G. S. Fischer, “Teleoperation system with hybrid pneumatic-piezoelectric actuation for MRI-guided needle insertion with haptic feedback,” *IEEE Int. Conf. Intell. Robot. Syst.*, pp. 4092–4098, 2013, doi: 10.1109/IROS.2013.6696942.

[46] H. Su *et al.*, “A MRI-guided concentric tube continuum robot with piezoelectric actuation: A feasibility study,” *Proc. - IEEE Int. Conf. Robot. Autom.*, pp. 1939–1945, 2012, doi: 10.1109/ICRA.2012.6224550.

[47] X. Liu *et al.*, “High-resolution intravascular MRI-guided perivascular ultrasound ablation,” *Magn. Reson. Med.*, vol. 83, no. 1, pp. 240–253, 2020, doi: 10.1002/mrm.27932.

[48] R. Staruch, R. Chopra, and K. Hynynen, “Localised drug release using MRI-controlled focused ultrasound hyperthermia,” *Int. J. Hyperth.*, vol. 27, no. 2, pp. 156–171, 2011, doi: 10.3109/02656736.2010.518198.

[49] H. H. Quick *et al.*, “Interventional magnetic resonance angiography with no strings attached: wireless active catheter visualization,” *Magn. Reson. Med. An Off. J. Int. Soc. Magn. Reson. Med.*, vol. 53, no. 2, pp. 446–455, 2005.

[50] C. M. Hillenbrand *et al.*, “Active Device Tracking and High-Resolution Intravascular MRI Using a Novel Catheter-Based, Opposed-Solenoid Phased Array Coil,” *Magn. Reson. Med.*, vol. 51, no. 4, pp. 668–675, 2004, doi: 10.1002/mrm.20050.

[51] Y. Qiu, L. Wu, F. Huang, Z. Huang, Q. Yan, and J. Guo, “MRI-Compatible Hydraulic Drive Needle Insertion Robot,” in *2021 6th IEEE International Conference on Advanced Robotics and Mechatronics (ICARM)*, Jul. 2021, pp. 86–92, doi: 10.1109/ICARM52023.2021.9536120.

[52] K. Masamune *et al.*, “Development of an MRI-compatible needle insertion

manipulator for stereotactic neurosurgery," *Comput. Aided Surg.*, vol. 1, no. 4, pp. 242–248, 1995, doi: 10.3109/10929089509106330.

[53] M. Vonthron, V. Lalande, G. Bringout, C. Tremblay, and S. Martel, "A MRI-based integrated platform for the navigation of microdevices and microrobots," *IEEE Int. Conf. Intell. Robot. Syst.*, pp. 1285–1290, 2011, doi: 10.1109/IROS.2011.6048274.

[54] G. K'osa, P. Jakab, G. Sz'ekely, and N. Hata, "MRI driven magnetic microswimmers," *Biomed. Microdevices*, vol. 14, no. 1, pp. 165–178, 2012.

[55] J.-B. Mathieu and S. Martel, "Steering of aggregating magnetic microparticles using propulsion gradients coils in an MRI scanner," *Magn. Reson. Med.*, vol. 63, no. 5, pp. 1336–1345, 2010.

[56] A. Aziz *et al.*, "Medical imaging of microrobots: toward in vivo applications," *ACS Nano*, vol. 14, no. 9, pp. 10865–10893, 2020.

[57] L. Arcese, M. Fruchard, and A. Ferreira, "Nonlinear modeling and robust controller-observer for a magnetic microrobot in a fluidic environment using MRI gradients," *2009 IEEE/RSJ Int. Conf. Intell. Robot. Syst. IROS 2009*, pp. 534–539, 2009, doi: 10.1109/IROS.2009.5354600.

[58] L. Arcese, M. Fruchard, F. Beyeler, A. Ferreira, and B. J. Nelson, "Adaptive backstepping and MEMS force sensor for an MRI-guided microrobot in the vasculature," *Proc. - IEEE Int. Conf. Robot. Autom.*, pp. 4121–4126, 2011, doi: 10.1109/ICRA.2011.5979954.

[59] K. Ahrar and R. J. Stafford, "Magnetic resonance imaging-guided laser ablation of bone tumors," *Tech. Vasc. Interv. Radiol.*, vol. 14, no. 3, pp. 177–182, 2011, doi: 10.1053/j.tvir.2011.02.010.

[60] J. G. R. Bomers *et al.*, "MRI-guided focal laser ablation for prostate cancer followed by radical prostatectomy: correlation of treatment effects with imaging," *World J. Urol.*, vol. 35, no. 5, pp. 703–711, 2017, doi: 10.1007/s00345-016-1924-1.

[61] G. P. Zientara *et al.*, “MRI monitoring of laser ablation using optical flow,” *J. Magn. Reson. Imaging*, vol. 8, no. 6, pp. 1306–1318, 1998, doi: 10.1002/jmri.1880080618.

[62] Z. Tovar-Spinoza, D. Carter, D. Ferrone, Y. Eksioglu, and S. Huckins, “The use of MRI-guided laser-induced thermal ablation for epilepsy,” *Child’s Nerv. Syst.*, vol. 29, no. 11, pp. 2089–2094, 2013, doi: 10.1007/s00381-013-2169-6.

[63] Y. Chen *et al.*, “Robotic system for MRI-guided focal laser ablation in the prostate,” *IEEE/ASME Trans. Mechatronics*, vol. 22, no. 1, pp. 107–114, 2017, doi: 10.1109/TMECH.2016.2611570.

[64] R. Salomir, F. C. Vimeux, J. A. De Zwart, N. Grenier, and C. T. W. Moonen, “Hyperthermia by MR-guided focused ultrasound: Accurate temperature control based on fast MRI and a physical model of local energy deposition and heat conduction,” *Magn. Reson. Med.*, vol. 43, no. 3, pp. 342–347, 2000, doi: 10.1002/(SICI)1522-2594(200003)43:3<342::AID-MRM4>3.0.CO;2-6.

[65] M. Tillander *et al.*, “High intensity focused ultrasound induced in vivo large volume hyperthermia under 3D MRI temperature control,” *Med. Phys.*, vol. 43, no. 3, pp. 1539–1549, 2016, doi: 10.1118/1.4942378.

[66] A. Antoniou *et al.*, “Robotic system for magnetic resonance guided focused ultrasound ablation of abdominal cancer,” *Int. J. Med. Robot. Comput. Assist. Surg.*, vol. 17, no. 5, pp. 1–9, 2021, doi: 10.1002/rcs.2299.

[67] F. Galassi, D. Brujic, M. Rea, N. Lambert, N. Desouza, and M. Ristic, “Fast and accurate localization of multiple RF markers for tracking in MRI-guided interventions,” *Magn. Reson. Mater. Physics, Biol. Med.*, vol. 28, no. 1, pp. 33–48, 2015.

[68] M. Rea, D. McRobbie, H. Elhawary, T. H. Zion, M. Lamperth, and I. Young, “Sub-pixel localisation of passive micro-coil fiducial markers in interventional MRI,” *Magn. Reson. Mater. Physics, Biol. Med.*, vol. 22, no. 2, pp. 71–76, 2009.

[69] A. Alipour, S. Gokyar, O. Algin, E. Atalar, and H. V. Demir, “An inductively

coupled ultra-thin, flexible, and passive RF resonator for MRI marking and guiding purposes: Clinical feasibility," *Magn. Reson. Med.*, vol. 80, no. 1, pp. 361–370, 2018.

[70] M. F. Dempsey and B. Condon, "Thermal injuries associated with MRI," *Clin. Radiol.*, vol. 56, no. 6, pp. 457–465, 2001.

[71] R. C. Susil, C. J. Yeung, H. R. Halperin, A. C. Lardo, and E. Atalar, "Multifunctional interventional devices for MRI: a combined electrophysiology/MRI catheter," *Magn. Reson. Med. An Off. J. Int. Soc. Magn. Reson. Med.*, vol. 47, no. 3, pp. 594–600, 2002.

[72] W. R. Nitz, A. Oppelt, W. Renz, C. Manke, M. Lenhart, and J. Link, "On the heating of linear conductive structures as guide wires and catheters in interventional MRI," *J. Magn. Reson. Imaging*, vol. 13, no. 1, pp. 105–114, 2001, doi: 10.1002/1522-2586(200101)13:1<105::AID-JMRI1016>3.0.CO;2-0.

[73] G. H. Griffin, K. J. T. Anderson, H. Celik, and G. A. Wright, "Safely assessing radiofrequency heating potential of conductive devices using image-based current measurements," *Magn. Reson. Med.*, vol. 73, no. 1, pp. 427–441, 2015, doi: 10.1002/mrm.25103.

[74] S. M. Park, R. Kamondetdacha, and J. A. Nyenhuis, "Calculation of MRI-induced heating of an implanted medical lead wire with an electric field transfer function," *J. Magn. Reson. Imaging*, vol. 26, no. 5, pp. 1278–1285, 2007, doi: 10.1002/jmri.21159.

[75] M. E. Ladd and H. H. Quick, "Reduction of resonant RF heating in intravascular catheters using coaxial chokes," *Magn. Reson. Med.*, vol. 43, no. 4, pp. 615–619, 2000, doi: 10.1002/(SICI)1522-2594(200004)43:4<615::AID-MRM19>3.0.CO;2-B.

[76] S. Wildermuth, C. L. Dumoulin, T. Pfammatter, S. E. Maier, E. Hofmann, and J. F. Debatin, "Mr-guided percutaneous angioplasty: Assessment of tracking safety, catheter handling and functionality," *Cardiovasc. Intervent. Radiol.*, vol. 21, no. 5, pp. 404–410, 1998, doi: 10.1007/s002709900288.

[77] F. Godinez *et al.*, “Interventional cardiac MRI using an add-on parallel transmit MR system: In vivo experience in sheep,” *Magn. Reson. Med.*, vol. 86, no. 6, pp. 3360–3372, 2021, doi: 10.1002/mrm.28931.

[78] L. Winter, F. Seifert, L. Zilberti, M. Murbach, and B. Ittermann, “MRI-Related Heating of Implants and Devices: A Review,” *J. Magn. Reson. Imaging*, vol. 53, no. 6, pp. 1646–1665, 2021, doi: 10.1002/jmri.27194.

[79] G. Bashein and G. SYROVY, “Burns associated with pulse oximetry during magnetic resonance imaging,” *J. Am. Soc. Anesthesiol.*, vol. 75, no. 2, p. 382, 1991.

[80] M. K. Konings, L. W. Bartels, H. F. M. Smits, and C. J. G. Bakker, “Heating around intravascular guidewires by resonating RF waves,” *J. Magn. Reson. Imaging*, vol. 12, no. 1, pp. 79–85, 2000.

[81] I. Khodarahmi, L. W. Bonham, C. R. Weiss, and J. Fritz, “Needle heating during interventional magnetic resonance imaging at 1.5-and 3.0-T field strengths,” *Invest. Radiol.*, vol. 55, no. 6, pp. 396–404, 2020.

[82] R. Buchli, P. Boesiger, and D. Meier, “Heating effects of metallic implants by MRI examinations,” *Magn. Reson. Med.*, vol. 7, no. 3, pp. 255–261, 1988.

[83] J. A. Nyenhuis, S.-M. Park, R. Kamondetdacha, A. Amjad, F. G. Shellock, and A. R. Rezai, “MRI and implanted medical devices: basic interactions with an emphasis on heating,” *IEEE Trans. device Mater. Reliab.*, vol. 5, no. 3, pp. 467–480, 2005.

[84] A. Boutet *et al.*, “Improving safety of MRI in patients with deep brain stimulation devices,” *Radiology*, vol. 296, no. 2, pp. 250–262, 2020.

[85] L. Golestanirad *et al.*, “RF-induced heating in tissue near bilateral DBS implants during MRI at 1.5 T and 3T: The role of surgical lead management,” *Neuroimage*, vol. 184, pp. 566–576, 2019.

[86] J. Haik, S. Daniel, A. Tessone, A. Orenstein, and E. Winkler, “MRI induced fourth-degree burn in an extremity, leading to amputation,” *Burns*, vol. 35, no. 2,

pp. 294–296, 2009.

[87] A. Vanne and K. Hynynen, “MRI feedback temperature control for focused ultrasound surgery,” *Phys. Med. Biol.*, vol. 48, no. 1, pp. 31–43, 2003, doi: 10.1088/0031-9155/48/1/303.

[88] L. Chen, J. P. Wansapura, G. Heit, and K. Butts, “Study of laser ablation in the in vivo rabbit brain with MR thermometry,” *J. Magn. Reson. Imaging*, vol. 16, no. 2, pp. 147–152, 2002, doi: 10.1002/jmri.10152.

[89] P. Wang and O. Unal, “Motion-compensated real-time MR thermometry augmented by tracking coils,” *J. Magn. Reson. Imaging*, vol. 41, no. 3, pp. 851–857, 2015, doi: 10.1002/jmri.24574.

[90] V. Ozenne *et al.*, “Improved cardiac magnetic resonance thermometry and dosimetry for monitoring lesion formation during catheter ablation,” *Magn. Reson. Med.*, vol. 77, no. 2, pp. 673–683, 2017, doi: 10.1002/mrm.26158.

[91] M. A. Ertürk, A. M. M. El-Sharkawy, and P. A. Bottomley, “Monitoring local heating around an interventional MRI antenna with RF radiometry,” *Med. Phys.*, vol. 42, no. 3, pp. 1411–1423, 2015, doi: 10.1118/1.4907960.

[92] T. T. Thai *et al.*, “Design and development of a novel passive wireless ultrasensitive RF temperature transducer for remote sensing,” *IEEE Sens. J.*, vol. 12, no. 9, pp. 2756–2766, 2012, doi: 10.1109/JSEN.2012.2201463.

[93] A. E. M. M. El-Sharkawy, P. P. Sotiriadis, P. A. Bottomley, and E. Atalar, “Absolute temperature monitoring using RF radiometry in the MRI scanner,” *IEEE Trans. Circuits Syst. I Regul. Pap.*, vol. 53, no. 11, pp. 2396–2404, 2006, doi: 10.1109/TCSI.2006.884423.

[94] A. Vaz *et al.*, “Full passive UHF tag with a temperature sensor suitable for human body temperature monitoring,” *IEEE Trans. Circuits Syst. II Express Briefs*, vol. 57, no. 2, pp. 95–99, 2010, doi: 10.1109/TCSII.2010.2040314.

[95] Di. Schröder *et al.*, “Magnetic Resonance Imaging Artifacts and Cochlear Implant Positioning at 1.5 T In Vivo,” *Biomed Res. Int.*, vol. 2018, pp. 1–4, Nov.

2018, doi: 10.1155/2018/9163285.

[96] A. S. Soliman, A. Owrangi, A. Ravi, and W. Y. Song, “Metal artefacts in MRI-guided brachytherapy of cervical cancer,” *J. Contemp. Brachytherapy*, vol. 4, no. 4, pp. 363–369, 2016, doi: 10.5114/jcb.2016.61817.

[97] B. A. Hargreaves, P. W. Worters, K. B. Pauly, J. M. Pauly, K. M. Koch, and G. E. Gold, “Metal-Induced Artifacts in MRI,” *Am. J. Roentgenol.*, vol. 197, no. 3, pp. 547–555, Sep. 2011, doi: 10.2214/AJR.11.7364.

[98] T. Kuehne, R. Fahrig, and K. Butts, “Pair of resonant fiducial markers for localization of endovascular catheters at all catheter orientations,” *J. Magn. Reson. Imaging An Off. J. Int. Soc. Magn. Reson. Med.*, vol. 17, no. 5, pp. 620–624, 2003.

[99] K. Will *et al.*, “Pre-tuned resonant marker for iMRI using aerosol deposition on polymer catheters,” in *Medical Imaging 2010: Visualization, Image-Guided Procedures, and Modeling*, 2010, vol. 7625, p. 76251Z.

[100] C. D. Jordan *et al.*, “Wireless resonant circuits printed using aerosol jet deposition for MRI catheter tracking,” *IEEE Trans. Biomed. Eng.*, vol. 67, no. 3, pp. 876–882, 2019.

[101] H. Celik, A. Ulut"urk, T. Tali, and E. Atalar, “A catheter tracking method using reverse polarization for MR-guided interventions,” *Magn. Reson. Med. An Off. J. Int. Soc. Magn. Reson. Med.*, vol. 58, no. 6, pp. 1224–1231, 2007.

[102] E. Baysoy, D. K. Yildirim, C. Ozsoy, S. Mutlu, and O. Kocaturk, “Thin film based semi-active resonant marker design for low profile interventional cardiovascular MRI devices,” *Magn. Reson. Mater. Physics, Biol. Med.*, vol. 30, no. 1, pp. 93–101, 2017.

[103] O. Nassar, D. Mager, and J. G. Korvink, “Wireless Double Micro-Resonator for Orientation Free Tracking of MR-Catheter During Interventional MRI,” *IEEE J. Electromagn. RF Microwaves Med. Biol.*, vol. 5, no. 1, pp. 78–83, 2020.

[104] C. G. Malmberg and A. A. Maryott, “Dielectric constant of water from 0 to 100

C," *J. Res. Natl. Bur. Stand. (1934).*, vol. 56, no. 1, p. 1, 1956, doi: 10.6028/jres.056.001.

[105] W. J. Ellison, "Permittivity of Pure Water, at Standard Atmospheric Pressure, over the Frequency Range 0–25THz and the Temperature Range 0–100°C," *J. Phys. Chem. Ref. Data*, vol. 36, no. 1, pp. 1–18, Mar. 2007, doi: 10.1063/1.2360986.

[106] M. Burl, G. A. Coutts, and I. R. Young, "Tuned fiducial markers to identify body locations with minimal perturbation of tissue magnetization," *Magn. Reson. Med.*, vol. 36, no. 3, pp. 491–493, 1996, doi: 10.1002/mrm.1910360326.

[107] J. K. Yang *et al.*, "Interventional magnetic resonance imaging guided carotid embolectomy using a novel resonant marker catheter: demonstration of preclinical feasibility," *Biomed. Microdevices*, vol. 19, no. 4, pp. 1–11, 2017.

[108] S. K. Aggarwal and R. H. Johnston, "Equations for complex relative permittivity of saline water," *IETE Tech. Rev. (Institution Electron. Telecommun. Eng. India)*, vol. 5, no. 8, pp. 317–320, 1988, doi: 10.1080/02564602.1988.11438336.

[109] S. Charkhabi, Y. J. Chan, D.-G. Hwang, S. T. Frey, M. D. Bartlett, and N. F. Reuel, "Kirigami-Enabled, Passive Resonant Sensors for Wireless Deformation Monitoring," *Adv. Mater. Technol.*, vol. 4, no. 5, p. 1800683, 2019.

[110] C. Andreuccetti, Daniele; Fossi, Roberto; and Petrucci, "Dielectric Properties of Body Tissues: Output data," *Ifac-Cnr*, vol. 5, 2014, [Online]. Available: http://niremf.ifac.cnr.it/tissprop/htmlclie/uniquery.php?func=atsffun&freq=4550000000&tiss=&outform=disphtm&tisname=on&frequen=on&conduct=on&permit=on&losstan=on&wavelen=on&pendept=on&freq1=4550000000&tissue2=Air&frqbeg=10&frqend=100e9&linstep=100&mode=l.

[111] T. Voigt, U. Katscher, and O. Doessel, "Quantitative conductivity and permittivity imaging of the human brain using electric properties tomography," *Magn. Reson. Med.*, vol. 66, no. 2, pp. 456–466, 2011, doi: 10.1002/mrm.22832.

[112] H. Zimmermann, S. Zuehlsdorff, R. Umathum, S. Volz, W. Semmler, and M.

Bock, “Use of fiducial markers for motion corrected MRI,” in *Proc Intl. Soc. Mag. Reson. Med*, 2003, vol. 11, p. 1059.

[113] D. K. Sodickson and W. J. Manning, “Simultaneous acquisition of spatial harmonics (SMASH): Fast imaging with radiofrequency coil arrays,” *Magn. Reson. Med.*, vol. 38, no. 4, pp. 591–603, 1997, doi: 10.1002/mrm.1910380414.

[114] A. S. C. Yang, M. Kretzler, S. Sudarski, V. Gulani, and N. Seiberlich, “Sparse reconstruction techniques in magnetic resonance imaging,” *Invest. Radiol.*, vol. 51, no. 6, pp. 349–364, 2016, doi: 10.1097/RLI.0000000000000274.

[115] A. D. Curtis and H. L. M. Cheng, “Primer and Historical Review on Rapid Cardiac CINE MRI,” *J. Magn. Reson. Imaging*, 2020, doi: 10.1002/jmri.27436.

[116] Y. S. Yaras *et al.*, “Real-time device tracking under MRI using an acousto-optic active marker,” *Magn. Reson. Med.*, vol. 85, no. 5, pp. 2904–2914, 2021, doi: 10.1002/mrm.28625.

[117] J. M. Serfaty, X. Yang, P. Aksit, H. H. Quick, M. Solaiyappan, and E. Atalar, “Toward MRI-guided coronary catheterization: Visualization of guiding catheters, guidewires, and anatomy in real time,” *J. Magn. Reson. Imaging*, vol. 12, no. 4, pp. 590–594, 2000, doi: 10.1002/1522-2586(200010)12:4<590::AID-JMRI11>3.0.CO;2-3.

[118] X. Liu *et al.*, “Real-Time High-Resolution MRI Endoscopy at up to 10 Frames per Second,” *BME Front.*, vol. 2021, pp. 1–10, 2021, doi: 10.34133/2021/6185616.

[119] S. Sathyanarayana, M. Schr, D. L. Kraitchman, and P. A. Bottomley, “Towards real-time intravascular endoscopic magnetic resonance imaging,” *JACC Cardiovasc. Imaging*, vol. 3, no. 11, pp. 1158–1165, 2010, doi: 10.1016/j.jcmg.2010.08.014.

[120] J. Barrese, X. R. Sun, N. Patel, P. Jethwa, and S. F. Danish, “Endoscopic laser ablation of clival chordoma with magnetic resonance-guided laser induced thermal therapy,” *Interdiscip. Neurosurg. Adv. Tech. Case Manag.*, vol. 1, no. 4,

pp. 76–80, 2014, doi: 10.1016/j.inat.2014.06.006.

[121] F. G. Shellock and E. Kanal, “Safety of magnetic resonance imaging contrast agents,” *J. Magn. Reson. Imaging*, vol. 10, no. 3, pp. 477–484, 1999, doi: 10.1002/(SICI)1522-2586(199909)10:3<477::AID-JMRI33>3.0.CO;2-E.

[122] K. N. Raymond and V. C. Pierre, “Next generation, high relaxivity gadolinium MRI agents,” *Bioconjug. Chem.*, vol. 16, no. 1, pp. 3–8, 2005, doi: 10.1021/bc049817y.

[123] C. Pan *et al.*, “An intelligent T 1- T 2switchable MRI contrast agent for the non-invasive identification of vulnerable atherosclerotic plaques,” *Nanoscale*, vol. 13, no. 13, pp. 6461–6474, 2021, doi: 10.1039/d0nr08039j.

[124] A. Servant *et al.*, “Gadolinium-functionalised multi-walled carbon nanotubes as a T1 contrast agent for MRI cell labelling and tracking,” *Carbon N. Y.*, vol. 97, pp. 126–133, 2016, doi: 10.1016/j.carbon.2015.08.051.

[125] H. K. Kim *et al.*, “Highly brain-permeable apoferritin nanocage with high dysprosium loading capacity as a new T2 contrast agent for ultra-high field magnetic resonance imaging,” *Biomaterials*, vol. 243, no. August 2019, p. 119939, 2020, doi: 10.1016/j.biomaterials.2020.119939.

[126] Y. D. Xiao, R. Paudel, J. Liu, C. Ma, Z. S. Zhang, and S. K. Zhou, “MRI contrast agents: Classification and application (Review),” *Int. J. Mol. Med.*, vol. 38, no. 5, pp. 1319–1326, 2016, doi: 10.3892/ijmm.2016.2744.

[127] N. Alghamdi *et al.*, “Structural, magnetic and toxicity studies of ferrite particles employed as contrast agents for magnetic resonance imaging thermometry,” *J. Magn. Magn. Mater.*, vol. 497, no. April 2019, p. 165981, 2019, doi: 10.1016/j.jmmm.2019.165981.

[128] H. Yim *et al.*, “The performance of gadolinium diethylene triamine pentaacetate-pullulan hepatocyte-specific T1 contrast agent for MRI,” *Biomaterials*, vol. 32, no. 22, pp. 5187–5194, 2011, doi: 10.1016/j.biomaterials.2011.03.069.

[129] J. Wang *et al.*, “An Ultrahigh-Field-Tailored T1–T2 Dual-Mode MRI Contrast

Agent for High-Performance Vascular Imaging," *Adv. Mater.*, vol. 33, no. 2, pp. 1–8, 2021, doi: 10.1002/adma.202004917.

[130] Y. Zhong *et al.*, "A rheumatoid arthritis magnetic resonance imaging contrast agent based on folic acid conjugated PEG-b-PAA@SPION," *J. Mater. Chem. B*, vol. 2, no. 19, pp. 2938–2946, 2014, doi: 10.1039/c4tb00085d.

[131] D. Koh, "Liver-specific contrast agents," vol. 12, no. October, pp. 363–364, 2012, doi: 10.1097/RLI.0b013.

[132] J. P. Ridgway, "Cardiovascular magnetic resonance physics for clinicians: part I," *J. Cardiovasc. Magn. Reson.*, vol. 12, no. 1, p. 71, Dec. 2010, doi: 10.1186/1532-429X-12-71.

[133] H. Bin Na *et al.*, "Development of aT1 Contrast Agent for Magnetic Resonance Imaging Using MnO Nanoparticles," *Angew. Chemie*, vol. 119, no. 28, pp. 5493–5497, 2007, doi: 10.1002/ange.200604775.

[134] T. Vangijzegem *et al.*, "VSION as high field MRI T 1 contrast agent: evidence of their potential as positive contrast agent for magnetic resonance angiography," *Nanotechnology*, vol. 29, no. 26, p. 265103, Jun. 2018, doi: 10.1088/1361-6528/aabbd0.

[135] S. Hong, Y. Chang, and I. Rhee, "Chitosan-coated ferrite (Fe3O4) nanoparticles as a T2 contrast agent for magnetic resonance imaging," *J. Korean Phys. Soc.*, vol. 56, no. 3, pp. 868–873, 2010, doi: 10.3938/jkps.56.868.

[136] S. D. Iancu *et al.*, "Assessment of gold-coated iron oxide nanoparticles as negative T2 contrast agent in small animal MRI studies," *Int. J. Nanomedicine*, vol. 15, pp. 4811–4824, 2020, doi: 10.2147/IJN.S253184.

[137] T. H. Shin *et al.*, "T 1 and T 2 dual-mode MRI contrast agent for enhancing accuracy by engineered nanomaterials," *ACS Nano*, vol. 8, no. 4, pp. 3393–3401, 2014, doi: 10.1021/nn405977t.

[138] H. Zhu *et al.*, "Aptamer-PEG-modified Fe3O4 @Mn as a novel T1-and T2-dual-model MRI contrast agent targeting hypoxia-induced cancer stem cells," *Sci.*

Rep., vol. 6, no. November, pp. 1–12, 2016, doi: 10.1038/srep39245.

[139] Y. X. J. Wang, S. M. Hussain, and G. P. Krestin, "Superparamagnetic iron oxide contrast agents: Physicochemical characteristics and applications in MR imaging," *Eur. Radiol.*, vol. 11, no. 11, pp. 2319–2331, 2001, doi: 10.1007/s003300100908.

[140] A. Jedlovszky-Hajdú, E. Tombácz, I. Bányai, M. Babos, and A. Palkó, "Carboxylated magnetic nanoparticles as MRI contrast agents: Relaxation measurements at different field strengths," *J. Magn. Magn. Mater.*, vol. 324, no. 19, pp. 3173–3180, 2012, doi: 10.1016/j.jmmm.2012.05.031.

[141] E. K. Schlachter *et al.*, "Metabolic pathway and distribution of superparamagnetic iron oxide nanoparticles: in vivo study.," *Int. J. Nanomedicine*, vol. 6, pp. 1793–1800, 2011, doi: 10.2147/ijn.s23638.

[142] S. Dadashi-Silab, Y. Yar, H. Yagci Acar, and Y. Yagci, "Magnetic iron oxide nanoparticles as long wavelength photoinitiators for free radical polymerization," *Polym. Chem.*, vol. 6, no. 11, pp. 1918–1922, 2015, doi: 10.1039/c4py01658k.

[143] M. Nejatpour, U. Unal, and H. Yağcı Acar, "Bidisperse magneto-rheological fluids consisting of functional SPIONs added to commercial MRF," *J. Ind. Eng. Chem.*, vol. 91, pp. 110–120, 2020, doi: 10.1016/j.jiec.2020.07.040.

[144] A. Carvalho, M. B. F. Martins, M. L. Corvo, and G. Feio, "Enhanced contrast efficiency in MRI by PEGylated magnetoliposomes loaded with PEGylated SPION: Effect of SPION coating and micro-environment," *Mater. Sci. Eng. C*, vol. 43, pp. 521–526, 2014, doi: 10.1016/j.msec.2014.07.055.

[145] B. Steitz *et al.*, "Characterization of PEI-coated superparamagnetic iron oxide nanoparticles for transfection: Size distribution, colloidal properties and DNA interaction," *J. Magn. Magn. Mater.*, vol. 311, no. 1 SPEC. ISS., pp. 300–305, 2007, doi: 10.1016/j.jmmm.2006.10.1194.

[146] R. Alwi *et al.*, "Silica-coated super paramagnetic iron oxide nanoparticles (SPION) as biocompatible contrast agent in biomedical photoacoustics," *Biomed.*

Opt. Express, vol. 3, no. 10, p. 2500, 2012, doi: 10.1364/boe.3.002500.

[147] K. Bilici *et al.*, "Broad spectrum antibacterial photodynamic and photothermal therapy achieved with indocyanine green loaded SPIONs under near infrared irradiation," *Biomater. Sci.*, vol. 8, no. 16, pp. 4616–4625, 2020, doi: 10.1039/d0bm00821d.

[148] M. Zuvin *et al.*, "Nanoparticle based induction heating at low magnitudes of magnetic field strengths for breast cancer therapy," *J. Magn. Magn. Mater.*, vol. 483, no. August 2018, pp. 169–177, 2019, doi: 10.1016/j.jmmm.2019.03.117.

[149] G. Odian, *Principles of Polymerization*. Hoboken, NJ, USA: John Wiley & Sons, Inc., 2004.

[150] Y. Yagci, S. Jockusch, and N. J. Turro, "Photoinitiated polymerization: Advances, challenges, and opportunities," *Macromolecules*, vol. 43, no. 15, pp. 6245–6260, 2010, doi: 10.1021/ma1007545.

[151] C. Calero, J. García-Torres, A. Ortiz-Ambriz, F. Sagués, I. Pagonabarraga, and P. Tierno, "Propulsion and energetics of a minimal magnetic microswimmer," *Soft Matter*, vol. 16, no. 28, pp. 6673–6682, 2020, doi: 10.1039/d0sm00564a.

[152] I. C. Yasa, A. F. Tabak, O. Yasa, H. Ceylan, and M. Sitti, "3D-Printed Microrobotic Transporters with Recapitulated Stem Cell Niche for Programmable and Active Cell Delivery," *Adv. Funct. Mater.*, vol. 29, no. 17, pp. 1–10, 2019, doi: 10.1002/adfm.201808992.

[153] I. C. Yasa, H. Ceylan, U. Bozuyuk, A. M. Wild, and M. Sitti, "Elucidating the interaction dynamics between microswimmer body and immune system for medical microrobots," *Sci. Robot.*, vol. 5, no. 43, pp. 1–14, 2020, doi: 10.1126/scirobotics.aaz3867.

[154] W. Hu, G. Z. Lum, M. Mastrangeli, and M. Sitti, "Small-scale soft-bodied robot with multimodal locomotion," *Nature*, vol. 554, no. 7690, pp. 81–85, 2018, doi: 10.1038/nature25443.

[155] L. Che Rose *et al.*, "A SPION-eicosane protective coating for water soluble

capsules: Evidence for on-demand drug release triggered by magnetic hyperthermia," *Sci. Rep.*, vol. 6, no. July 2015, pp. 1–5, 2016, doi: 10.1038/srep20271.

[156] A. H. Alhasan *et al.*, "Polymeric Reactor for the Synthesis of Superparamagnetic-Thermal Treatment of Breast Cancer," *Mol. Pharm.*, vol. 16, no. 8, pp. 3577–3587, 2019, doi: 10.1021/acs.molpharmaceut.9b00433.

[157] S. Stolik, J. A. Delgado, A. Pérez, and L. Anasagasti, "Measurement of the penetration depths of red and near infrared light in human ″ex vivo″ tissues," *J. Photochem. Photobiol. B Biol.*, vol. 57, no. 2–3, pp. 90–93, 2000, doi: 10.1016/S1011-1344(00)00082-8.

[158] E. Buz, F. Morlet-Savary, J. Lalevée, and H. Y. Acar, "CdS–Oleic Acid Quantum Dots as Long-Wavelength Photoinitiators in Organic Solvent and Preparation of Luminescent, Colloidal CdS/Polymer Nanocomposites," *Macromol. Chem. Phys.*, vol. 219, no. 2, pp. 1–7, 2018, doi: 10.1002/macp.201700356.

[159] EELS Database, "EELS Atlas, Iron-oxide magnetite, iron loss," 2008. https://eelsdb.eu/spectra/iron-oxide-magnetite/ (accessed Dec. 07, 2021).

[160] EELS Database, "EELS Atlas, Iron-oxide magnetite, oxygen loss," 2008. https://eelsdb.eu/spectra/iron-oxide-magnetite-2/.

[161] A. Lak *et al.*, "Highly stable monodisperse PEGylated iron oxide nanoparticle aqueous suspensions: A nontoxic tracer for homogeneous magnetic bioassays," *Nanoscale*, vol. 5, no. 23, pp. 11447–11455, 2013, doi: 10.1039/c3nr02197a.

Appendix A: Surface coil trial for RF sensor

As initial design surface coils were experimented. Designs were surface spiral shapes; square spiral, Archimedean spiral and double Archimedean spiral (Figure 0.1).

Figure 0.1: Initial surface coil designs in order; square, Archimedean and double Archimedean spiral

Initial manufacturing method started with polyimide coated copper sheet with thickness of 80 µm super glued on to a substrate like glass or plexiglass (Figure 0.2).

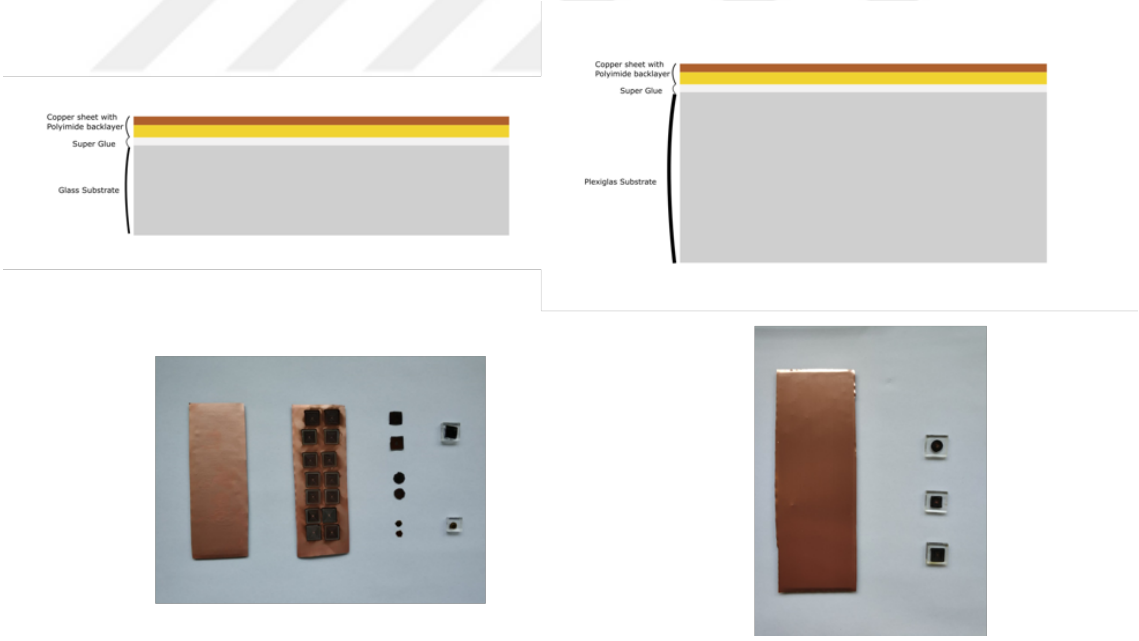

Figure 0.2: Manufacturing process of the surface coils.

Then, coils were cut out using a laser cutter (Figure 0.2). Individual coils were extracted and imaged under MRI, which gave high contrasts as shown in Figure 0.3. However, this manufacturing method was not robust and coils were too sensitive for deformations. Hence, this design was discontinued.

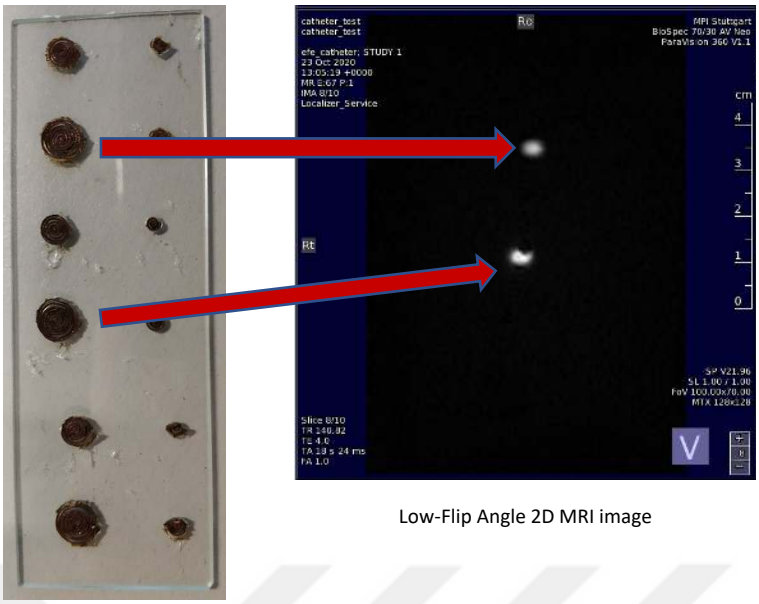

Low-Flip Angle 2D MRI image

Figure 0.3: MRI image of surface coils

Appendix B: Sample code

Below is the sample code for RC evaluation of the individual markers during MRI characterization. This particular code was modified for finding the effect of the repetition time on RC values. There are several codes similar to one below, modified for evaluating the effect of each parameter.

Code (TR_FA_20210627):

```
clear all

Nifti_to_Read = [ 729:738 29:728 ];
pos_images_places = 1:10;

flip_angle = [ 0.1:0.1:1.0, 2:5 ];
rot_angles = [0:10:90];
repetition_time = [7.183, 10, 12.5, 15, 20];
FoV_data = 120;
pixels = [256];
measurement_parameters = {'Rotation' , rot_angles , 'flip_angle',
flip_angle, 'pixel', pixels, 'repetition_time', repetition_time};

address = 'I:\20210627\Antenna_single_sweep_Berk_imaging_20_';

last_image_rotates_too_much= 1;
well_count = 12;
proximity_number = 3;
signalbox = 8;
corner_reference_point_changes = [ floor(length(rot_angles)/3) ,...
    (length(rot_angles) - floor(length(rot_angles)/3)) ];
sample_box_dimensions = [54.5, 70.5];
well_halflength = 12.35;
well_halfwidth = 5;
well_spacing = 1.35;

%% Parameter Properties

param_count = length(measurement_parameters)/2;
image_per_rotation = 1;

for param = 4:2:size(measurement_parameters, 2)
    image_per_rotation = image_per_rotation *
length(measurement_parameters{param});
end

image_per_rotation = image_per_rotation/length(pixels);

%% Read Data && Sample box thresholding

image_numbers = 1:length(Nifti_to_Read);
V = cell(1, length(image_numbers));
raw_images = cell(length(pixels),0);
pixel_data = image_numbers.*0;
```

```
threshold_array = zeros(length(pixels),
length(image_numbers)/length(pixels));
pixcol = [0, 0];

for i = image_numbers
    filename = strcat(address, int2str(Nifti_to_Read(i)), '_1_1.nii');
    V{1, i} = niftiread(filename);
    pixel_data(i) = size(V{1, i}, 1);
    rower = 1:length(pixels);
    row_pos = rower((pixels==pixel_data(i))==1);
    pixcol(row_pos) = pixcol(row_pos)+1;
    raw_images{row_pos, pixcol(row_pos)} = double(V{1,
i})/double(max(max(V{1, i})))*1.0;
    pxPerMm = pixel_data(i)/FoV_data;
    sample_box_size=(10*pxPerMm*24*pxPerMm)*12;
    thrshld = 0.01;

    while threshold_array(row_pos,pixcol(row_pos)) == 0
        thresholded_size = length(raw_images{row_pos,
pixcol(row_pos)}(raw_images{row_pos, pixcol(row_pos)}>thrshld));
        if (sample_box_size*0.99 > thresholded_size)
            thrshld = 0.9*abs(thrshld);
        elseif (sample_box_size*2 <= thresholded_size)
            thrshld = 2*abs(thrshld);
        elseif (sample_box_size*1.001 < thresholded_size)
            thrshld = 1.1*abs(thrshld);
        elseif (sample_box_size*0.99 <= thresholded_size) &&...
                (thresholded_size <= sample_box_size*1.001)
            threshold_array(row_pos,pixcol(row_pos)) = thrshld;
        end
    end
end


pos_images(:, :) = raw_images(:,pos_images_places);
pos_threshold_array = threshold_array(:,pos_images_places);


%% Geometric

image_corners = zeros(2,4, size(raw_images,1), size(raw_images,2));
Centers = zeros(2, 1, size(pos_images,1), size(pos_images,2));
vectors = zeros(2, 2,size(pos_images,1), size(pos_images,2));
opened_image = cell(1, length(rot_angles));
for pix_var = 1:length(pixels)
    for j = 1 : corner_reference_point_changes(1)
        opened_image{1, j} = pos_images{pix_var,j};
        for T = 2 : pixels(pix_var)
            for x = 1 : T
                y = T+1-x;
                if image_corners(:,1,pix_var,j) == [0;0]
                    if opened_image{1,j}(x,y) >=
pos_threshold_array(pix_var,j)
                        image_corners(:,1,pix_var,j) =[x;y];
                    end
                end
                if image_corners(:,2,pix_var,j) == [0;0]
                    if opened_image{1,j}(x,pixels(pix_var)+1-y) >
pos_threshold_array(pix_var,j)
```

```
                        image_corners(:,2,pix_var,j) =
[x;pixels(pix_var)+1-y];
                    end
                end
                if image_corners(:,3,pix_var,j) == [0;0]
                    if opened_image{1,j}(pixels(pix_var)+1-
x,pixels(pix_var)+1-y) > pos_threshold_array(pix_var,j)
                        image_corners(:,3,pix_var,j) =
[pixels(pix_var)+1-x;pixels(pix_var)+1-y];
                    end
                end
                if image_corners(:,4,pix_var,j) == [0;0]
                    if opened_image{1,j}(pixels(pix_var)+1-x,y) >
pos_threshold_array(pix_var,j)
                        image_corners(:,4,pix_var,j) =
[pixels(pix_var)+1-x;y];
                    end
                end
            end
        end

    end

    for j = corner_reference_point_changes(1)+1 :
corner_reference_point_changes(2)

        opened_image{1, j} = pos_images{pix_var,j};


        for x = 1 : pixels(pix_var)
            for y = 1 : pixels(pix_var)
                if image_corners(:,1,pix_var,j) == [0;0]
                    if opened_image{1,j}(x,y) >=
pos_threshold_array(pix_var,j)
                        image_corners(:,1,pix_var,j) = [x;y];
                    end
                end
                if image_corners(:,2,pix_var,j) == [0;0]
                    if opened_image{1,j}(y,pixels(pix_var)+1-x) >
pos_threshold_array(pix_var,j)
                        image_corners(:,2,pix_var,j) =
[y;pixels(pix_var)+1-x];
                    end
                end
                if image_corners(:,3,pix_var,j) == [0;0]
                    if opened_image{1,j}(pixels(pix_var)+1-
x,pixels(pix_var)+1-y) > pos_threshold_array(pix_var,j)
                        image_corners(:,3,pix_var,j) =
[pixels(pix_var)+1-x;pixels(pix_var)+1-y];
                    end
                end
                if image_corners(:,4,pix_var,j) == [0;0]
                    if opened_image{1,j}(pixels(pix_var)+1-y, x) >
pos_threshold_array(pix_var,j)
                        image_corners(:,4,pix_var,j) =
[pixels(pix_var)+1-y;x];
                    end
                end
            end
        end
```

```
    end

    for j = corner_reference_point_changes(2)+1 : length(rot_angles)

        opened_image{1, j} = pos_images{pix_var,j};

        for T = 2 : pixels(pix_var)
            for x = 1 : T
                y = T+1-x;
                if image_corners(:,1,pix_var,j) == [0;0]
                    if opened_image{1,j}(x,pixels(pix_var)+1-y) >
pos_threshold_array(pix_var,j)
                        image_corners(:,1,pix_var,j) =
[x;pixels(pix_var)+1-y];
                    end
                end
                if image_corners(:,2,pix_var,j) == [0;0]
                    if opened_image{1,j}(pixels(pix_var)+1-
x,pixels(pix_var)+1-y) > pos_threshold_array(pix_var,j)
                        image_corners(:,2,pix_var,j) =
[pixels(pix_var)+1-x;pixels(pix_var)+1-y];
                    end
                end
                if image_corners(:,3,pix_var,j) == [0;0]
                    if opened_image{1,j}(pixels(pix_var)+1-x,y) >
pos_threshold_array(pix_var,j)
                        image_corners(:,3,pix_var,j) =
[pixels(pix_var)+1-x;y];
                    end
                end
                if image_corners(:,4,pix_var,j) == [0;0]
                    if opened_image{1,j}(x,y) >=
pos_threshold_array(pix_var,j)
                        image_corners(:,4,pix_var,j) = [x;y];
                    end
                end
            end
        end
    end
end


for pix_var = 1:length(pixels)
    for k = pos_images_places

        Centers(:,:,pix_var,k) = [mean(image_corners(1,:,pix_var,k));
mean(image_corners(2,:,pix_var,k))];
        v11 = image_corners(1,2,pix_var,k)-
image_corners(1,1,pix_var,k);
        v12 = image_corners(2,2,pix_var,k)-
image_corners(2,1,pix_var,k);
        v21 = image_corners(1,4,pix_var,k)-
image_corners(1,1,pix_var,k);
        v22 = image_corners(2,4,pix_var,k)-
image_corners(2,1,pix_var,k);
        vectors(1,1,pix_var,k) = v11/sqrt(abs((v11^2) + (v12^2)));
        vectors(2,1,pix_var,k) = v12/sqrt(abs((v11^2) + (v12^2)));
        vectors(1,2,pix_var,k) = v21/sqrt(abs((v21^2) + (v22^2)));
        vectors(2,2,pix_var,k) = v22/sqrt(abs((v21^2) + (v22^2)));
```

```
    end
end



%% Setting Position Vectors

for set = 1:10
    for go = 1:image_per_rotation
            Centers(:,:,:,10+go+(set-1)*image_per_rotation) =
Centers(:,:,:,set);
            vectors(:,:,:,10+go+(set-1)*image_per_rotation) =
vectors(:,:,:,set);
            image_corners(:,:,:,10+go+(set-1)*image_per_rotation) =
image_corners(:,:,:,set);
    end
end


%% Rotation

rotated_images = cell(size(raw_images));
angles = zeros(1,10);
for pix_var = 1:length(pixels)
    for i = pos_images_places
        angle = RotMatAngleFinder(vectors(:,:,pix_var,i));
        if i == pos_images_places(end)
            if last_image_rotates_too_much == 1
                angle = -1*angle;
            end
        end
        angles(i) = angle;
        rotated_images(pix_var,i) =
{imrotate(raw_images{pix_var,i},(90-angle), 'nearest', 'loose')};
        for go = 1:image_per_rotation
            angles(10+(i-1)*image_per_rotation+go) = angle;
            rotated_images(pix_var,10+(i-1)*image_per_rotation+go) =
{imrotate(raw_images{pix_var,10+(i-1)*image_per_rotation+go},(90-
angle), 'nearest', 'loose')};

        end
    end
end


%% Well data

well_positioning_images = cell(length(pixels), length(rot_angles));
well_centers =
zeros(2,well_count,length(pixels),length(Nifti_to_Read)/length(pixels)
);
well_coordinates =
zeros(2,4,well_count,length(pixels),length(Nifti_to_Read)/length(pixel
s));
rotated_image_corners =
zeros(2,4,length(pixels),length(Nifti_to_Read)/length(pixels));
well_cell =
cell(well_count,length(pixels),length(Nifti_to_Read)/length(pixels));
```

```
for pix_var = 1:length(pixels)
    for j = pos_images_places

        well_positioning_images(:, j) = rotated_images(:,j);

        clear opened_image_2
        opened_image_2(:,:) = well_positioning_images{pix_var,j};
        image_size=size(opened_image_2(:,:), 1);

        for T = 1 : image_size
            for x = 1 : T
                y = T-x+1;
                if rotated_image_corners(:,1,pix_var,j) == [0;0]
                    if opened_image_2(x,y) >=
threshold_array(pix_var,j)
                        rotated_image_corners(:,1,pix_var,j) = [x;y];
                    end
                end
                if rotated_image_corners(:,2,pix_var,j) == [0;0]
                    if opened_image_2(x,image_size-y) >=
threshold_array(pix_var,j)
                        rotated_image_corners(:,2,pix_var,j) =
[x;image_size+1-y];
                    end
                end
                if rotated_image_corners(:,3,pix_var,j) == [0;0]
                    if opened_image_2(image_size-x,image_size-y) >=
threshold_array(pix_var,j)
                        rotated_image_corners(:,3,pix_var,j) =
[image_size+1-x;image_size+1-y];
                    end
                end
                if rotated_image_corners(:,4,pix_var,j) == [0;0]
                    if opened_image_2(image_size-x,y) >=
threshold_array(pix_var,j)
                        rotated_image_corners(:,4,pix_var,j) =
[image_size+1-x;y];
                    end
                end
            end
        end

        pixel_multiplier = pixels(pix_var) / FoV_data;
        well_centers_axis1 =
round(rotated_image_corners(2,1,pix_var,j) +
well_halfwidth*pixel_multiplier):...

round((2*well_halfwidth+well_spacing)*pixel_multiplier):round(rotated_
image_corners(2,3,pix_var,j));
        well_centers_axis2 =
round(rotated_image_corners(1,1,pix_var,j) +
well_halflength*pixel_multiplier):...

round((2*well_halflength+well_spacing)*pixel_multiplier):round(rotated
_image_corners(1,3,pix_var,j));

        well_centers(:,:,pix_var,j)=[well_centers_axis1,
well_centers_axis1; well_centers_axis2(1)*ones(1,6),
well_centers_axis2(2)*ones(1,6)];
```

```
        for w = 1:well_count

            well_image_halfwidth = round(well_halfwidth *
pixel_multiplier);
            well_image_halflength = round(well_halflength *
pixel_multiplier);

            well_coordinates(:,:,w,pix_var,j) =
[well_centers(2,w,pix_var,j) + well_image_halflength,...
                well_centers(2,w,pix_var,j) - well_image_halflength,
well_centers(2,w,pix_var,j) - well_image_halflength,...
                well_centers(2,w,pix_var,j) + well_image_halflength;
well_centers(1,w,pix_var,j) + well_image_halfwidth,...
                well_centers(1,w,pix_var,j) + well_image_halfwidth,
well_centers(1,w,pix_var,j) - well_image_halfwidth,...
                well_centers(1,w,pix_var,j) - well_image_halfwidth];

            well_cell{w, pix_var, j} =
rotated_images{pix_var,j}(well_coordinates(1,3,w,pix_var,j):well_coord
inates(1,1,w,pix_var,j),...

well_coordinates(2,3,w,pix_var,j):well_coordinates(2,1,w,pix_var,j));

        end
    end
end


%% Setting Well Position Vectors

for pix_var = 1:length(pixels)
    pixel_multiplier = pixels(pix_var) / FoV_data;
    for set = pos_images_places
        for go = 1:image_per_rotation
            well_centers(:,:,pix_var,10+go+(set-1)*image_per_rotation)
= round(well_centers(:,:,pix_var,set));
            well_coordinates(:,:,:,pix_var,10+go+(set-
1)*image_per_rotation) = round(well_coordinates(:,:,:,pix_var,set));
            rotated_image_corners(:,:,pix_var,10+go+(set-
1)*image_per_rotation) =
round(rotated_image_corners(:,:,pix_var,set));
            for w = 1:well_count
                well_cell{w,pix_var,10+go+(set-1)*image_per_rotation}
= rotated_images{pix_var,10+go+(set-1)*image_per_rotation}...
                    (well_coordinates(1,3,w,pix_var,10+go+(set-
1)*image_per_rotation):well_coordinates(1,1,w,pix_var,10+go+(set-
1)*image_per_rotation),...
                    well_coordinates(2,3,w,pix_var,10+go+(set-
1)*image_per_rotation):well_coordinates(2,1,w,pix_var,10+go+(set-
1)*image_per_rotation));
            end
        end
    end
end

%% Locating Markers within wells

marker_info = cell(4, well_count, pix_var, size(rotated_images, 2)-
length(pos_images_places));
```

```
for pix_var = 1:length(pixels)
    for k = 1:size(marker_info, 4)
        for w = 1:well_count
            temp = well_cell{w, pix_var, k+10};
            std_dev = std2(temp);
            mean_well = mean2(temp);
            sorted = sort(temp(temp>0), 'descend');
            marker_appearance_count=0;
            marker_index_pos=2;
            while sorted(1) > (mean_well+8*std_dev)
                marker_appearance_count=marker_appearance_count+1;
                [index1, index2] = find(temp==sorted(1), 1);
                marker_info{1,w,pix_var,k} = marker_appearance_count;
                marker_info{marker_index_pos, w, pix_var, k} =
[index1, index2];
                if index1 <= proximity_number
                    index1 = proximity_number+1;
                end
                if index2 <= proximity_number
                    index2 = proximity_number+1;
                end
                temp(index1-
proximity_number:index1+proximity_number,...
                    index2-
proximity_number:index2+proximity_number)=0;
                sorted = sort(temp(temp>0), 'descend');
                marker_index_pos= 1+marker_index_pos;
            end
        end
    end
end


%% Matching Markers

transimage_marker_log = cell(1,1,length(pixels));
old_marker_flag = 0;

for pix_var = 1:length(pixels)
    marker_number = 1;
    for i = 1:size(rotated_images, 2)-length(pos_images_places)
        for w = 1:well_count
            if not(isempty(marker_info{1,w,pix_var,i}))
                for inWellMarkerNumber = 1:marker_info{1,w,pix_var,i}
                    old_marker_flag = 0;
                    if not(isempty(transimage_marker_log))
                        sz = size(transimage_marker_log);
                        for logged_marker = 1:sz(1)
                            if transimage_marker_log{logged_marker, 1,
pix_var} == w
                                for exwells = 2:sz(2)
                                    if
not(isempty(transimage_marker_log{logged_marker,exwells, pix_var}))
                                        old_marker_flag = 1;
                                        old_marker_number =
logged_marker;
                                    end
                                end
                            end
```

```
                        end
                    end

                    if old_marker_flag == 0
                        transimage_marker_log{marker_number,1,
pix_var} = w;
                        transimage_marker_log{marker_number,i+1,
pix_var} = [marker_info{inWellMarkerNumber+1, w, pix_var, i}];
                        marker_number = marker_number + 1;
                    end
                    if old_marker_flag == 1
                        transimage_marker_log{old_marker_number,i+1,
pix_var} = [marker_info{inWellMarkerNumber+1, w, pix_var, i}];
                    end
                end
            end
        end
    end
end

%% Average marker positions

sz = size(transimage_marker_log);
marker_average_positions = zeros(2, sz(1), length(pos_images_places),
pix_var);
temp_for_avr_pos = [0, 0];

for pix_var = 1:length(pixels)
    for i = 1:sz(1)
        prev_rot_pos_backup = [0,0];
        prev_rot_pos_backup_count = 0;
        for set = 1:length(pos_images_places)
            temp_for_avr_pos = [0, 0];
            marker_appearance_count = 0;
            for go = 1:image_per_rotation
                j = go+(set-1)*image_per_rotation;
                if not(isempty(transimage_marker_log{i,j+1,pix_var}))
                    temp_for_avr_pos(1) =
temp_for_avr_pos(1)+transimage_marker_log{i,j+1,pix_var}(1);
                    temp_for_avr_pos(2) =
temp_for_avr_pos(2)+transimage_marker_log{i,j+1,pix_var}(2);
                    marker_appearance_count = marker_appearance_count
+ 1;
                end
            end
            if temp_for_avr_pos(1) == 0 || temp_for_avr_pos(2) == 0
                if prev_rot_pos_backup(1) ~= 0 &&
prev_rot_pos_backup(2) ~= 0
                    temp_for_avr_pos = prev_rot_pos_backup;
                    marker_appearance_count =
prev_rot_pos_backup_count;
                end
                if prev_rot_pos_backup(1) == 0 ||
prev_rot_pos_backup(2) == 0
                    temp_for_avr_pos = [0, 0];
                    for sset = 1:length(pos_images_places)
                        for ggo = 1:image_per_rotation
                            j = ggo+(sset-1)*image_per_rotation;
                            if
not(isempty(transimage_marker_log{i,j+1,pix_var}))
```

```
                                temp_for_avr_pos(1) =
temp_for_avr_pos(1)+transimage_marker_log{i,j+1,pix_var}(1);
                                temp_for_avr_pos(2) =
temp_for_avr_pos(2)+transimage_marker_log{i,j+1,pix_var}(2);
                                marker_appearance_count =
marker_appearance_count + 1;
                            end
                        end
                    end
                end
            end
            prev_rot_pos_backup = temp_for_avr_pos;
            prev_rot_pos_backup_count = marker_appearance_count;
            marker_average_positions(1,i,set,pix_var) =
round(temp_for_avr_pos(1)/marker_appearance_count);
            marker_average_positions(2,i,set,pix_var) =
round(temp_for_avr_pos(2)/marker_appearance_count);
        end
    end
 end


%% Converting image coordinates

marker_image_coor = transimage_marker_log;

for pix_var = 1:length(pixels)
    for j = 1:sz(1)
        for k1 = 1:length(pos_images_places)
            for k2 = 1:image_per_rotation
                k = (k1-1)*image_per_rotation+k2+1;
                if not(isempty(transimage_marker_log{j, k, pix_var}))
                    marker_image_coor{j,k, pix_var} =
[transimage_marker_log{j, k, pix_var}(1)+ ...
                        well_coordinates(1,3,transimage_marker_log{j,
1, pix_var},pix_var,k-1+10)-...
                        (rotated_image_corners(1,1,pix_var,k-1+10)-
round(15*pixels(pix_var)/pixels(1))), transimage_marker_log{j, k,
pix_var}(2) + ...
                        well_coordinates(2,3,transimage_marker_log{j,
1, pix_var},pix_var,k-1+10)-...
                        (rotated_image_corners(2,1,pix_var,k-1+10)-
round(15*pixels(pix_var)/pixels(1)))];
                end

                if isempty(transimage_marker_log{j, k, pix_var})
                    if not(isempty(transimage_marker_log{j, 1,
pix_var}))
                        marker_image_coor{j,k, pix_var} = [
marker_average_positions(1,j,k1,pix_var)+...

well_coordinates(1,3,transimage_marker_log{j, 1, pix_var},pix_var,k-
1+10)-...
                            (rotated_image_corners(1,1,pix_var,k-
1+10)-round(15*pixels(pix_var)/pixels(1))),
marker_average_positions(2,j,k1,pix_var)+...

well_coordinates(2,3,transimage_marker_log{j, 1, pix_var},pix_var,k-
1+10)-...
```

```
                            (rotated_image_corners(2,1,pix_var,k-
1+10)-round(15*pixels(pix_var)/pixels(1)))];
                    end
                end
            end
        end
    end
end


%% Position Visualiation

rect_image = {};
cropped_images = {};
sz = size(marker_image_coor);


for pix_var = 1:length(pixels)
    cropping_coordinates(:,1,pix_var,:) =
[rotated_image_corners(1,1,pix_var,:)-15*pix_var,
rotated_image_corners(2,1,pix_var,:)-15*pix_var];
    for i = length(pos_images_places)+1:size(rotated_images, 2)
        cropped_images{pix_var,i} =
imcrop(rotated_images{pix_var,i},[cropping_coordinates(2,1,pix_var,i).
..
            cropping_coordinates(1,1,pix_var,i)
round(sample_box_dimensions(2)*pixels(pix_var)/FoV_data)+round(30*pixe
ls(pix_var)/pixels(1))...

round(sample_box_dimensions(1)*pixels(pix_var)/FoV_data)+round(30*pixe
ls(pix_var)/pixels(1))]);
        rect_image{pix_var,i} = cropped_images{pix_var,i};
        for j = 1:sz(1)
            if not(isempty(marker_image_coor{j,i+1-10,pix_var}))
                rect_image{pix_var,i} =
insertShape(rect_image{pix_var,i},'Rectangle',...
                    [marker_image_coor{j,i+1-10,pix_var}(2)-
5*pixels(pix_var)/pixels(1) marker_image_coor{j,i+1-10,...
                    pix_var}(1)-5*pixels(pix_var)/pixels(1)
11*pixels(pix_var)/pixels(1) 11*pixels(pix_var)/pixels(1)],...
                    'LineWidth', 1, 'Color', 'g');
            end
        end
    end
end

%% SNR calculations

CBR = zeros(sz(1), size(rotated_images, 2)+1, length(pixels));
marker_signals = zeros(sz(1), size(rotated_images, 2)+1,
length(pixels));
Background_signal = zeros(sz(1), size(rotated_images, 2)+1,
length(pixels));

for pix_var = 1:length(pixels)
    for k = length(pos_images_places)+1:size(rotated_images, 2)
        noise_mean =
mean2(rotated_images{pix_var,k}(rotated_images{pix_var,k}<threshold_ar
ray(pix_var,k)));
```

```
        noise =
std2(rotated_images{pix_var,k}(rotated_images{pix_var,k}<threshold_arr
ay(pix_var,k)));
        temp =
rotated_images{pix_var,k}(5*threshold_array(pix_var,k)>rotated_images{
pix_var,k});
        sample_mean =
mean2(temp(1.2*threshold_array(pix_var,k)<temp));

        for i = 1:sz(1)
            if not(isempty(marker_image_coor{i,1,pix_var}))
                CBR(i,k,pix_var) = (max(max( ...
                    cropped_images{pix_var,k}(
marker_image_coor{i,k+1-10,pix_var}(1)-
signalbox/2:marker_image_coor{i,k+1-10,pix_var}(1)+signalbox/2,...
                    marker_image_coor{i,k+1-10,pix_var}(2)-
signalbox/2:marker_image_coor{i,k+1-10,pix_var}(2)+signalbox/2)))...
                    - sample_mean )/ sample_mean;
                marker_signals(i,k,pix_var)=max(max(img(k-
10,:,:)))*max(max(cropped_images{pix_var,k}( marker_image_coor{i,k+1-
10,pix_var}(1)-signalbox/2:marker_image_coor{i,k+1-
10,pix_var}(1)+signalbox/2,...
                    marker_image_coor{i,k+1-10,pix_var}(2)-
signalbox/2:marker_image_coor{i,k+1-10,pix_var}(2)+signalbox/2)));

Background_signal(i,k,pix_var)=mean2(temp(1.0*threshold_array(pix_var,
k)<temp))*max(max(img(k-10,:,:)));
            end
        end
    end

    for i = 1:sz(1)
        if not(isempty(marker_image_coor{i,1,pix_var}))
            CBR(i,end,pix_var) = marker_image_coor{i,1,pix_var};
        end
    end

end
```